Transmission Electron Imaging and Diffraction Characterisation of 2D Nanomaterials

Aleksey Shmeliov
St. Edmund Hall
University of Oxford

A thesis submitted for the degree of
Doctor of Philosphy
Hilary 2014

Abstract

Following the discovery of graphene, 2D nanostructures have been noted for their potential in a range of high-impact applications, such as sensing, catalysis, and composite reinforcement. Liquid-phase exfoliation and chemical vapour deposition have been demonstrated and indicate the feasibility of mass-scale production. With the advent of mass-produced 2D nanostructures a key focus of research is to characterise these materials.

This thesis is concerned with imaging and structural properties of the 2D nanomaterials, hexagonal boron nitride (*h*-BN), molybdenum disulfide (MoS_2), tungsten disulfide (WS_2), titanium disulfide (TiS_2) and hexabenzocoronene (HBC), produced via liquid phase exfoliation. HBC strictly speaking is not 2D nanomaterial, however, it can be viewed as transition molecule from benzene to graphene. The data used for characterisation is based primarily on electron diffraction and, in particular, aberration corrected annular dark field (ADF) scanning transmission electron microscopy (STEM). The incoherent nature of ADF STEM provides direct atomic imaging without the contrast reversals upon focus changes seen in conventional high-resolution transmission electron microscopy (HRTEM).

The main structural feature investigated in this thesis was the stacking sequences in few-layers *h*-BN, MoS_2, WS_2 and TiS_2. Simple stacking (AAA) can be distinguished from Bernal (ABA) and rhombohedral (ABC) on the basis of intensity ratio, $I_{\{10\bar{1}0\}}/I_{\{11\bar{2}0\}}$, in diffraction patterns and indirectly in HRTEM images. Nonetheless acquisition of the diffraction patterns suitable for analysis can be challenging due to the sample issues. Non-bulk stacking sequences were reliably confirmed for all above 2D nanomaterials on the basis of atomically resolved ADF STEM. 20 *h*-BN, 28 MoS_2, 5 WS_2 and 6 TiS_2 nanoflakes were imaged and analysed. Amongst them 2 *h*-BN, 9 MoS_2, 4 WS_2 and 1 TiS_2 nanoflakes displayed non-bulk stacking. Hence, it appears that 2D WS_2 has the greatest affinity for non-bulk stacking.

Finally, an interesting structural transformation was observed in HBC molecules. Under the influence of electron beam HBC agglomerates were transformed into crystalline phase with 90^o symmetry.

List of Publications

Some of the work contained in this thesis has been published elsewhere in peer-reviewed journals. A list of publications is given here.

[1] J. N. Coleman, M. Lotya, A. O'Neill, S. D. Bergin, P. J. King, U. Khan, K. Young, A. Gaucher, S. De, R. J. Smith, I. V. Shvets, S. K. Arora, G. Stanton, H.-Y. Kim, K. Lee, G. T. Kim, G. S. Duesberg, T. Hallam, J. J. Boland, J. J. Wang, J. F. Donegan, J. C. Grunlan, G. Moriarty, **A. Shmeliov**, R. J. Nicholls, J. M. Perkins, E. M. Grieveson, K. Theuwissen, D. W. McComb, P. D. Nellist, and V. Nicolosi, "Two-dimensional nanosheets produced by liquid exfoliation of layered materials," *Science.*, vol. 331, no. 6017, pp. 568–571, Feb. 2011.

[3] J. M. Hughes, Y. Hernandez, D. Aherne, L. Doessel, K. Müllen, B. Moreton, T. W. White, C. Partridge, G. Costantini, **A. Shmeliov**, M. Shannon, V. Nicolosi, and J. N. Coleman, "High quality dispersions of hexabenzocoronene in organic solvents.," *J. Am. Chem. Soc.*, vol. 134, no. 29, pp. 12168–79, Jul. 2012.

[2] **A. Shmeliov**, J. S. Kim, K. B. Borisenko, P. Wang, E. Okunishi, M. Shannon, A. I. Kirkland, P. D. Nellist, and V. Nicolosi, "Impurity induced non-bulk stacking in chemically exfoliated h-BN nanosheets.," *Nanoscale*, vol. 5, no. 6, pp. 2290–4, Mar. 2013.

[4] **A. Shmeliov**, M. Shannon, P. Wang, J. S. Kim, E. Okunishi, P. D. Nellist, K. Dolui, S. Sanvito, and V. Nicolosi, "Unusual stacking variations in liquid-phase exfoliated transition metal dichalcogenides.," *ACS Nano*, vol. 8, no. 4, pp. 3690–9, Apr. 2014.

Table of Contents

Abstract iii

List of Publications iv

Table of Contents v

Chapter 1: Introduction 1

1.1 The rise of 2D nanoworld 1

1.2 Synthesis of 2D nanostructures 2

1.3 Aims of the project 4

Chapter 2: Theoretical Background 6

2.1 Liquid-phase exfoliation 6

2.2 Transmission Electron Microscopy 7

2.2.1 Brief History 7

2.2.2 Basics of Transmission Microscopy 9

2.2.3 Electron Diffraction 12

2.2.4 Image Formation Theory 16

2.2.4.1 Conventional Transmission Electron Microscopy 17

2.2.4.2 Scanning Transmission Electron Microscopy 21

2.2.5 Aberration corrected microscopy 25

2.2.6 Electron Energy Loss Spectroscopy 27

Chapter 3: Experimental and Processing Routines 29

3.1 Samples Preparation 29

3.2 Imaging 30

3.3 Image Processing 31

3.4 Butterworth Filter 32

3.5 Masking in Digital Micrograph 33

3.6 Krivanek's Filter 35

3.7 Image Simulations....36
Chapter 4: 2D hexagonal boron nitride....40
4.1 Introduction....40
4.2 Structural Models....43
4.3 Conventional TEM and Diffraction....44
4.4 Aberration-corrected TEM....48
4.5 Aberration-corrected STEM....52
4.6 EELS....62
4.7 Summary of the findings....64
Chapter 5: 2D Transition Metal Dichalcogenides....65
5.1 2D MoS_2 and WS_2....65
5.1.1 Introduction....65
5.1.2 Conventional TEM and Diffraction....68
5.1.3 Aberration corrected TEM....70
5.1.4 Aberration corrected STEM....71
5.1.4.1 2D MoS_2....72
5.1.4.2 2D WS_2....80
5.2 2D TiS2....83
5.2.1 Introduction....83
5.2.2 Conventional TEM and Diffraction....84
5.2.3 Aberration-corrected STEM....85
5.2.4 EELS....89
5.3 Summary of the findings....89
Chapter 6: Hexabenzocoronene....91
6.1 Introduction....91
6.2 Imaging....92
6.2.1 Aberration-corrected TEM....92

6.2.2 Aberration-corrected STEM 94
6.3 Summary of the findings 97
Chapter 7: Conclusions 98
7.1 Characterisation techniques 98
7.2 Structural findings 99
7.3 Future work 100
References 101
Appendix A: Structure Factor Calculation 118
Appendix B: C_s-corrector drift 120

Chapter 1: Introduction

1.1 The rise of 2D nanoworld

The concept of 2D crystalline nanosheets was first introduced in theoretical calculations of graphite properties [1][2]. After the discovery of nanotubes [3][4] their structural properties, such as chirality, began to be described in terms of roll up vectors defined on 2D crystalline nanosheets [3][5]. The discovery of graphene [6], a single layer of graphite, provided a necessary "proof of concept" for the existence of 2D nanostructures. Its remarkable physical properties, attributed to the confinement of electron in two dimensions [6][7][8], sparked broad scientific interest in other 2D nanostructures [9][10][11]. The typical bulk materials which have 2D equivalents are highly anisotropic layered materials, where atoms within layers are held together by the strong covalent bonds and layers are attracted together by much weaker Van der Waals forces [12].

Prior to the discovery of graphene [6], it was generally believed that there was a thickness limit for thin crystalline films. Theoretical calculations predict that 2D nanomaterials are thermodynamically unstable at any finite temperature [13][14]. Mechanisms of thin film growth models [15][16][17] based on the amassed experimental evidence also suggest the impossibility of long range 2D crystalline order. Nevertheless, there were a number of attempts to exfoliate layered materials down to few layers or grow a monolayer on a catalytic surface [18][19][20][21][22]. However, in most of these cases the thickness measurements either did not have sufficient sensitivity [19] or were unreliable [20][21][22]. A special case was the report of a monolayer of hexagonal boron nitride, *h*-BN, formed on a Ni(111) surface [23]. A presence of a monolayer was confirmed by Scanning Tunnelling Microscopy (STM), but it was not shown that a monolayer can exist without the presence of a crystalline substrate. From the historic perspective the earlier discovery of 2D nanostructures as a new class of low dimensional materials was impossible due to the limitation of available instrumentation.

After the discovery of graphene [6], the question of its stability arose. It was hypothesized that after cleavage from the bulk phase, graphene is left in a metastable state, assisted by a strong in-plane covalent bonding. It was also suggested that once graphene is produced, it loses its perfectly flat surface, acquiring a wavy shape. These surface undulations were confirmed experimentally [24][25][26].

There is no strict definition of the 2D nanomaterial. However it is possible to define a set of criteria which a material must fulfil in order to qualify as 2D nanomaterial:

- They must have sheet-like structure with a typical thickness below 10nm.
- They must be thermodynamically stable as freely suspended membranes.
- They are expected to exhibit effects and properties, attributed to the two-dimensional confinement of the electrons which are unobserved in the bulk phase. For example for few layers graphene it is the behaviour of electrons as massless Dirac fermions [7] and quantum Hall effect [8]. Another example is monolayer MoS_2 and WS_2 which are direct band-gap semiconductors [27][28][29], while in the bulk form both materials have indirect band gap.

In principle, any layered material should be able to form 2D nanostructures [9][30]. There are a large number of materials with layered structure such as graphite, *h*-BN, SnS_2, transition metal chalcogenides, transition metal oxides, etc. Moreover, this list can be further extended by the materials which do not have 3D layered structure but are capable to form quasi-2D nanostructures on a certain surfaces [31][32]. Since a broad range of metals and oxidation states is included in this class of materials, a broad range of properties is observed, giving the opportunity of tuning the desired properties by controlling the composition of the materials. Essentially, layered materials cover the full range of electronic properties: metals [33], semimetals [6], semiconductors [34], insulators [35], superconductors [36], and even charge density waves [37]. As a result there are many potential applications which can benefit from an increased surface area and novel properties such as thermoelectric devices [38][39], photocatalysts [40], nanocomposites [30], supercapacitors [41], field effect transistors [42][43] etc. In addition, the whole new field of research emerged based on heterostructures and devices made by stacking different 2D crystals on top of each other [44].

1.2 Synthesis of 2D nanostructures

Originally graphene was produced by peeling off flakes by Scotch tape from highly ordered pyrolitic graphite (HOPG) [6]. Currently this method is known as micromechanical cleavage, and initially was the most common method for production of 2D flakes from layered materials. Micromechanical cleavage can produce defect free large size flakes (greater than $1\mu m$) which are preferable for applications testing

[6][42][45][46]. Obviously, this method cannot be up-scaled. Moreover, a transfer of peeled off flakes onto a suitable substrate is lengthy and challenging [24].

Another method of top-down synthesis of 2D nanostructures is liquid exfoliation. As the name suggests the final product is a suspension of 2D flakes in an appropriate solvent. This method can be roughly subdivided into four categories:

1. One of the first methods developed for production of 2D nanoflakes involves intercalation of alkali metals (primarily Li) between the layers under inert conditions [20]. The intercalation process can be assisted by ultrasonication [21]. After that, the intercalated material is usually placed into water where the reaction of alkali metal with water causes layers to separate producing a suspension of nanoflakes. Recently, this method was greatly improved by introducing controllable electrochemical lithiation process [47][48].
2. It is possible to achieve direct exfoliation of the layered material in a solvent [49][30] with the help of ultrasonication but it requires the solvent to have approximately the same surface energy as the 2D nanocrytals.
3. In certain cases, instead of matching the surface energy of the solvent with the 2D nanoflake material, it is easier to add surfactant [50][51] or a polymer [52] which will modify surface energies and will allow, ultrasonication-assisted, exfoliation in more common solvents.
4. Sometimes, it is easier to exfoliate material which was initially chemically modified. After exfoliation, a reverse chemical reaction allows the production of nanoflakes of the original material. Such an approach is typical for graphene [53] where graphite is first oxidized, then exfoliated to produce graphene oxide, and finally, it is reduced to obtain a graphene suspension. Similarly, the surface of the material can be irreversibly functionalized and then dispersed in common solvents [54]. In principle, it might be possible to remove functional groups by annealing but it will require the deposition of the material onto the surface.

The main advantages of the liquid phase exfoliation are the high yield and the product versatility because materials in a liquid phase can easily be processed for most applications such as thin film transistors [55], transparent conductors [56], nanocomposites [30] etc. Moreover, nanoflakes in the liquid phase can be easily deposited onto TEM grids by drop-cast method for characterisation using electron microscopy. However, only direct exfoliation in a solvent provides chemically non-

contaminated samples. In all other cases it is impossible to completely remove surfactants, chemical modifiers, or inclusion molecules from the final product. The main drawbacks of this method are poor monolayer yield and limited lateral flake size. Extensive review of liquid exfoliation of layered materials, containing detailed information on families of layered compounds, their structure, exfoliation method, applications and commercial availability is given by Nicolosi et al [57].

An alternative approach to micromechanical cleavage and liquid exfoliation is epitaxial growth of 2D nanomaterials on flat highly crystalline substrates, primarily by chemical vapour deposition (CVD) [22][58][59][60][61]. Epitaxial growth allows formations of large areas 2D nanofilms with precise control of the number of layers. Epitaxially grown 2D nanostructures can suffer from multicrystallinity [60][62] where the properties of the material are dominated by the grain boundaries [63]. Epitaxial growth is up-scalable and for the case of graphene is envisaged as the main production technique which would allow its commercialisation in electronic devices [64][65]. Similar to the micromechanically cleaved 2D nanocrystals the transfer from the original substrate poses a challenge and can cause contamination of the sample.

1.3 Aims of the project

So far most of the research on the topic of 2D nanomaterials has been dedicated to graphene. However as mentioned earlier, there are many other interesting layered materials with unexpected novel properties in the 2D state. The primary objectives of the project are the imaging and determination of the structural properties of 2D nanostructures of hexagonal boron nitride (*h*-BN), tungsten disulfide (WS_2), molybdenum disulfide (MoS_2) and titanium disulfide (TiS_2) produced via direct exfoliation in solvent. The main structural features, intended for investigation, are stacking sequences in MoS_2, WS_2 and TiS_2. In addition, characterisation of liquid exfoliated hexabenzocoronene (HBC) molecule as a special case of 2D nanomaterial, is carried out.

The main technique chosen for characterisation of the samples is transmission electron microscopy (TEM) which encompasses selected area electron diffraction (SAED) conventional TEM (CTEM)[1], scanning TEM (STEM) and electron energy loss spectroscopy (EELS). These characterisation methods will be accompanied by the

[1] Atomically resolved CTEM will be referred as high-resolution TEM (HRTEM).

necessary calculations and image simulations for the reliable assessment of the results. It is expected that some of these techniques might be better suited for characterisation of certain structural features. Therefore the secondary objective is an assessment of capabilities of the available TEM techniques in the effective characterisation of the specific structural features of the 2D nanostructures.

Chapter 2: Theoretical Background

2.1 Liquid-phase exfoliation

As mentioned in the introduction 2D nanostructures can be obtained from layered crystals. The atoms within layers are held by strong covalent bonds while layers are weakly bound with van der Waals forces. In order to exfoliate layered materials van der Waals bonds must be broken. The whole process can be viewed as a mixing process and understood in terms of basic thermodynamics. For the exfoliation to be a spontaneous process the change in the Gibbs free energy, ΔG_{mix}, of the process must be negative:

$$\Delta G_{mix} = \Delta H_{mix} - T\Delta S_{mix} < 0 \qquad \text{Eq. 2.1}$$

where ΔH_{mix} and ΔS_{mix} are respectively the enthalpy and the entropy of exfoliation. For extended objects like 2D nanostructures ΔS_{mix} can be neglected, therefore ΔG_{mix} is dominated by the enthalpy of the process. Under these circumstances, the enthalpy of mixing can be approximated as:

$$\Delta H_{mix} \approx (\delta_{2D} - \delta_{solvent})^2 (1 - \phi)\phi \qquad \text{Eq. 2.2}$$

where δ_i is the Hildebrand solubility parameter and ϕ is the solute volume fraction. The Hildebrand solubility parameter is the square root of the cohesive energy density. Hence, for successful exfoliation, the cohesive energy density of the solvent and the 2D nanocrystal must be matched. Even if $\delta_{2D} \approx \delta_{solvent}$, ΔH_{mix} is still only zero and $\Delta G_{mix} \approx 0$. In reality, approximated terms of Eq. 2.2 and positive ΔS_{mix} result in $\Delta G_{mix} < 0$.

For a more detailed analysis of the solvent-solute interactions the consideration of the Hildebrand parameter alone is not sufficient and must be separated out into components (Hansen solubility parameters): dispersive, polar, Hydrogen bonding. Therefore, the appropriate solvent for exfoliation must be the one which has the same type of bonds as in the 2D nanocrystal. Following this approach successful exfoliation of carbon nanotube bundles [66], graphene [49] and other layered materials in general [30] was achieved. The detailed derivations are presented in the supplementary information of these papers [66][49][30].

2.2 Transmission Electron Microscopy

This chapter outlines the basic theoretical background of Transmission Electron Microscopy (TEM). The following description does not aim to be comprehensive but only present the most essential concepts of this technique, omitting full mathematical derivations. These concepts are necessary for better understanding the imaging mechanisms and the analytical capabilities of the TEM. For further background and mathematical derivations, the author suggests references [67][68][69][70][71].

2.2.1 Brief History

By the beginning of the 20th century it was already firmly established that resolution, δ_d, in optical microscopes is given by the Rayleigh criterion defining the diffraction limit:

$$\delta_d = 0.61 \frac{\lambda}{\mu \sin \theta} \qquad \text{Eq. 2.3}$$

where λ is the wavelength of the radiation, μ the refractive coefficient of the viewing medium, and θ the semi-angle of collection of the magnifying lens. Hence, for improved resolution, a minimisation of λ is required. In 1925 Luis de Broglie postulated that all particles have some wave-like properties (wave-particle duality) [72]. Correspondingly, the wavelength of the particle can be expressed as:

$$\lambda = \frac{h}{p} \qquad \text{Eq. 2.4}$$

where h is Planck's constant and p is momentum of the particle. Few years later, Davisson and Germer [73] and Thomson and Reid [74] experimentally confirmed the wave nature of electrons. The first conventional transmission electron microscope (CTEM) was designed in 1931 by Knoll and Russka. They employed magnetic lens to focus an electron beam and successfully obtained a magnified image.

Eq. 2.4 can be rewritten to express λ as a function of electron's energy, E:

$$\lambda = \frac{h}{\sqrt{2 m_0 e E}} \qquad \text{Eq. 2.5}$$

where m_0 is the rest mass of electron and e electron's charge. For high electron energies (> 50 keV) the above equation requires relativistic correction:

$$\lambda = \frac{h}{\sqrt{2m_0 eE(1 + \frac{e}{2m_0 c^2}E)}} \qquad \text{Eq. 2.6}$$

where c is the speed of light in vacuum. Table 2.1 shows the electron wavelengths corresponding to different energies with relativistic correction. Despite, several orders of magnitude of difference between the wavelength of the visible light (450 – 600 nm) and the wavelength of accelerated electrons, the original first CTEM instrument developed by Knoll and Ruska did not surpass the resolution of the best light microscopes of those days. The main limitation of the CTEM can be attributed to the poor quality of magnetic lenses.

Table 2.1. Relativistic electron wavelengths for selected acceleration voltages.

E (keV)	$\lambda_{relativistic}$ (pm)
50	5.36
80	4.18
100	3.70
200	2.51
300	1.97

Thereafter, the major historical milestones of TEM development can be summarised as below:

- In 1931 Knoll and Russka designed and constructed the first CTEM [75].
- In 1936 Otto Scherzer proved that a round magnetic lens suffers from positive spherical aberration C_s [76].
- In 1937-1938 Manfred von Ardenne designed and constructed the first scanning transmission electron microscope, STEM [77].
- In 1949 Scherzer examined the optimum CTEM imaging conditions in detail (Scherzer conditions) [78].

- In 1970 Albert Victor Crewe introduced cold field emission gun, CFEG, and annular dark field, ADF, detector in STEM mode which allowed him to image individual atoms on a substrate [79].
- In 1995 Joachim Zach and Maximilian Haider successfully implemented quadrupole-octupole C_s corrector in scanning electron microscope, SEM, configuration [80].
- In 1998 Haider *et al*. implemented hexapole C_s corrector in TEM configuration [81].
- In 1999 Ondrej Krivanek *et al*. implemented quadrupole-octupole C_s corrector in STEM configuration and demonstrated atomic resolution capabilities [82].

2.2.2 Basics of Transmission Microscopy

Fig. 2.1 shows a basic schematic of the main components of a transmission electron microscope. The object outside the focal length of the objective lens is illuminated with a parallel illumination. The focusing of the objective lens produces a real, inverted image. The projector lenses, if necessary, can be used to transfer the image onto a fluorescent screen or a CCD camera.

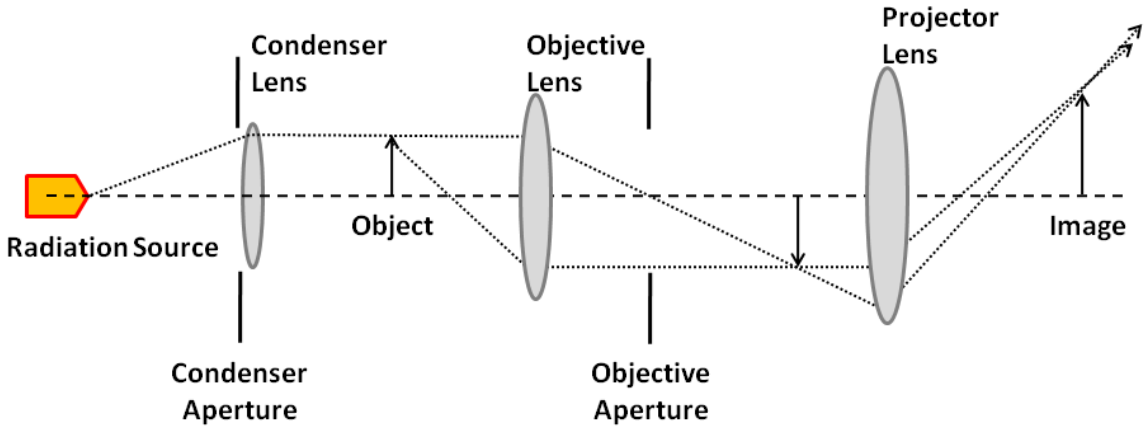


Figure 2.1. Schematic ray diagram of the transmission microscope.

The objective lens is usually a round magnetic lens which is rotationally symmetric. In 1936 Scherzer proved that images produced by such a lens will always suffer from spherical aberrations (C_s). The effect of the aberrations can be demonstrated by considering the converging effect of the lens (Fig. 2.2a). An ideal lens is expected to focus parallel rays in the focal point. However, a lens suffering from spherical aberration will produce stronger focusing effect on the rays further away from optical axes. As a

result, instead of producing a point image at the focal point, a diffused disc obtained. The plane of least confusion is located before the back focal plane where the smallest disc is produced. It is convenient to reconsider the same example in terms of wavefront (Fig. 2.2b). For an ideal lens a perfect spherical wavefront is obtained. The difference between this perfect spherical wave and the actual wavefront is used to define the wave aberration function, χ, which is sometimes re-written with the wave-number, $2\pi/\lambda$, factored out:

$$\chi = \frac{2\pi}{\lambda} W \qquad \text{Eq. 2.7}$$

This new function W can be used to represent the distance between perfect and aberrated wavefronts (Fig. 2.2b):

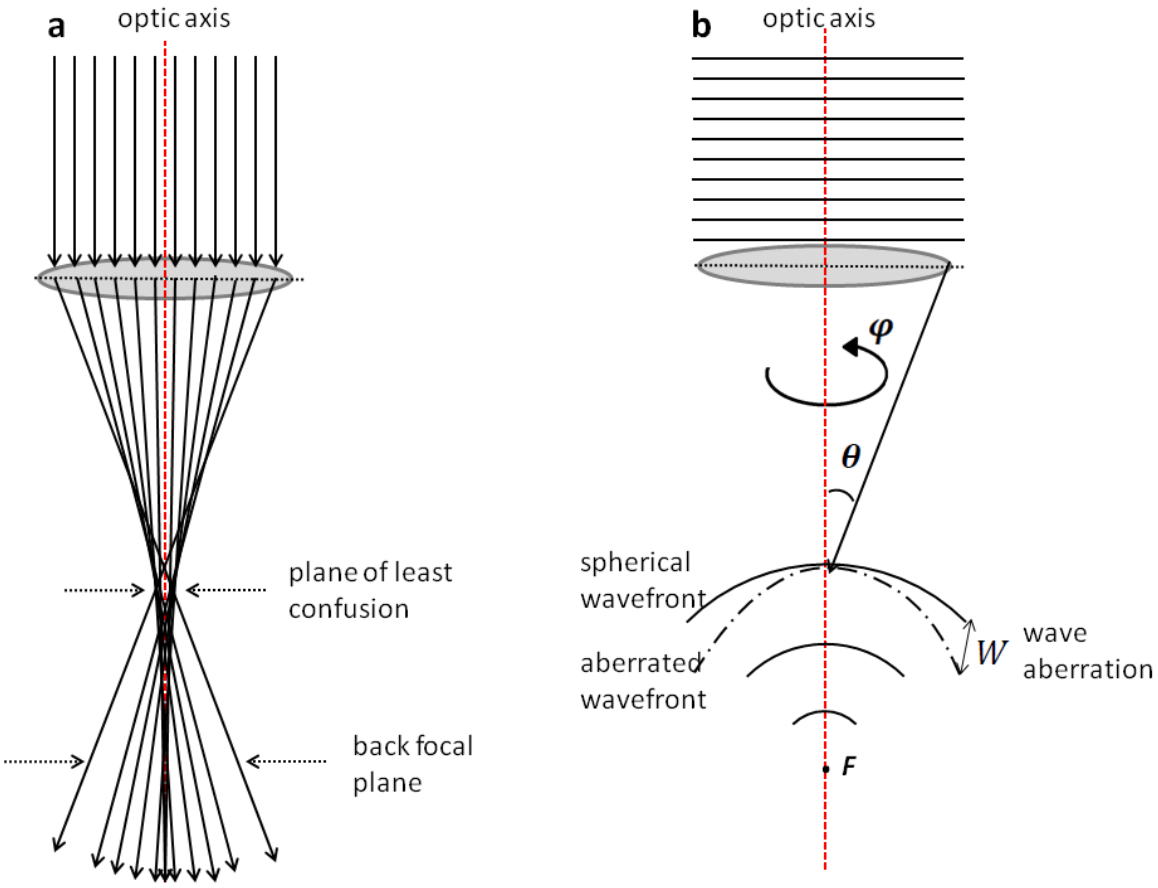


Figure 2.2. Effect of spherical aberration on the (a) electron trajectories (b) electron wavefront.

χ is function of the angle to the optic axis, θ, and azimuthal angle, φ, around the optic axis. Ideally, $\chi(\theta, \varphi)$ should be zero everywhere but in practise it is set as close as possible to zero up to a θ_{max}. Badly aberrated rays at an angles exceeding θ_{max} can be cut off by the use of an objective aperture. The aberration function can therefore be

conveniently expanded as a power series, where the coefficients of expansion are aberration coefficients. Several mathematical approaches can be used for such expansion. As a result several notations of aberration coefficients exist [81][82]. In the rest of this work Uhlemann & Haider notation [81] is used. This notation is employed in the aberration correctors produced by CEOS. A list of aberrations up to the 5th order is given in Table 2.2.

Table 2.2. The name, order in $\boldsymbol{\theta}$ and azimuthal symmetry for the aberrations.

Aberration Coefficient	Notation Symbol	Order in θ	Azimuthal Symmetry
Defocus	$C_1, \Delta f$	1	∞
Twofold astigmatism	A_1	1	2
Threefold astigmatism	A_2	2	3
Axial coma	B_2	2	1
Spherical aberration	C_3, C_s	3	∞
Fourfold astigmatism	A_3	3	4
Star aberration	S_3	3	2
Fivefold astigmatism	A_4	4	5
Axial coma	B_4	4	1
Three lobe aberration	D_4	4	3
Spherical aberration	C_5	5	∞
Sixfold astigmatism	A_5	5	6

The aberrations discussed above are known as geometric aberrations. They are also known as coherent aberrations since distortions of the wavefront do not lead to the loss of coherence. The effect of the coherent aberrations can be corrected using exit wave reconstruction routines such as focal series [83] or tilt series reconstructions [84]. On the other hand incoherent aberrations, such as chromatic aberration, add blurring effect to the image which cannot be corrected for. Similarly, mechanical and electrical instabilities can lead to incoherent blurring.

2.2.3 Electron Diffraction

The geometrical conditions governing diffraction in crystalline materials are given by the Bragg's Law. It can be readily visualised by considering two plane waves with wavelength λ (wavevector $\boldsymbol{k}$) incident upon a set of parallel planes (Fig. 2.3a). If the diffracted waves (wavecector $\boldsymbol{k}'$) are to interfere constructively the following condition (Bragg's Law) must be satisfied:

$$2d_{hkl} \sin \theta_B = n\lambda \qquad \text{Eq. 2.8}$$

where d_{hkl} is the interlayer spacing of the lattice planes with Miller indices (hkl), θ_B is the Bragg angle and n is the diffraction order. Rather than using n^{th} order diffraction from (hkl) plane it is more straightforward to discuss first-order diffraction from $(nh\ nk\ nl)$ planes. Following this approach the Bragg law can be simplified to

$$2d_{hkl} \sin \theta_B = \lambda \qquad \text{Eq. 2.9}$$

For all intents and purposes it is more practical to work with Bragg's Law in reciprocal space (Fig. 2.3b), which can be re-written as

$$\boldsymbol{k}' = \boldsymbol{k} + \mathbf{g}_{hkl} \qquad \text{Eq. 2.10}$$

where $\mathbf{g}_{hkl}$ is the reciprocal lattice vector representing (hkl) plane. It is instructive to redraw visualisation of the Bragg's Law as in Fig. 2.3c. The Bragg's scattering is an elastic process, therefore $|\boldsymbol{k}| = |\boldsymbol{k}'| = 1/\lambda$. Under these circumstances any of the reciprocal space points lying on the surface of the sphere (Ewald's sphere) with radius $|\boldsymbol{k}|$ and origin $\mathcal{O}$ shall satisfy Bragg's condition. The probability that the Ewald's sphere will intersect infinitely small reciprocal space point is zero. The only exception is $\mathbf{g}_{000}$ which corresponds to the transmitted, unscattered beam. Nonetheless the finite dimensions of a crystal result in reciprocal space points which are no longer infinitely small (relrods). As a result Bragg's condition relaxes significantly making diffraction possible. In addition it is important to notice that the extremely small wavelength of the electrons produces an Ewald's sphere which is almost flat near the origin $\mathcal{O}$, making electron diffraction a highly probable event.

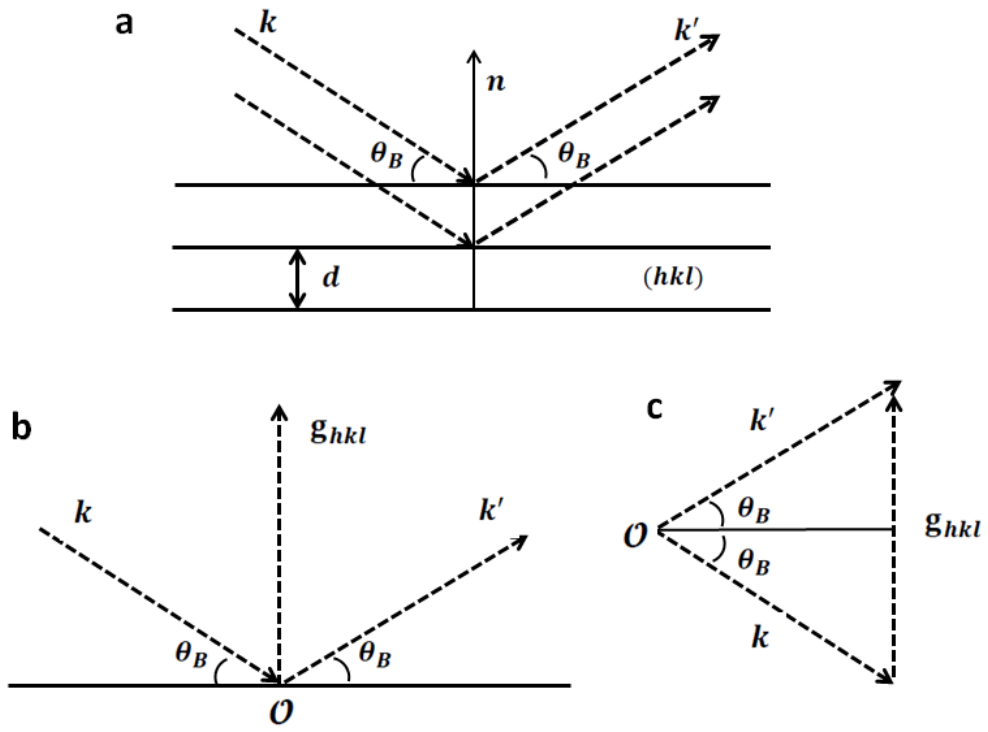


Figure 2.3. Schematic of the wave diffracted from the set of parallel planes in (a) real space (b) reciprocal space. (c) Visualisation of the Bragg's law as the vector triangle.

Each crystal consists of a periodic arrangement of lattice points. Each lattice points can consist of one (1 basis) or more atoms (n basis). The Bragg's law was derived in reference to the lattice planes described by Miller indices. Therefore if crystal structure is defined by more than single basis, contribution of each scatterer towards diffraction must be further analysed. This is expressed via parameter known as structure factor, F_{hkl}:

$$F_{hkl}(\theta) = \sum_n f_n\,(\theta) e^{2\pi i(hx_n + ky_n + lz_n)} \qquad \text{Eq. 2.11}$$

where $f_n(\theta)$ is the atomic scattering amplitude of the nth atom with coordinates (x_n, y_n, z_n). Intuitively, if $F_{hkl} = 0$, the diffraction spot intensity for that particular reflection is also zero. The particular importance of the structure factors is that they allow the prediction of relative intensities, $I_{hkl}/I_{h'k'l'}$, of the diffraction spots for single scattering events:

$$\frac{I_{hkl}}{I_{h'k'l'}} \approx \frac{|F_{hkl}|^2}{|F_{h'k'l'}|^2} \qquad \text{Eq. 2.12}$$

All of the 2D nanocrystals used in this work have hexagonal symmetry (Fig. 2.4a). The lattice parameters for the hexagonal system are given by $\{a, a, c, 90°, 90°, 120°\}$. Three non-coplanar basis vectors, $\mathbf{a}_1$, $\mathbf{a}_2$, $\mathbf{c}$, suffice to define this structure. However for hexagonal system there is an advantage in adding fourth basis vectors, $\mathbf{a}_3$ (Fig. 2.4a). The result of the fourth basis vector is an additional index i in reciprocal space. The use of 4 indices, $(hkil)$, for hexagonal systems is known as Miller-Bravais notation. h, k and l are equivalent to Miller indices and i is a redundant index which can be expressed as:

$$i = -(h + k) \qquad \text{Eq. 2.13}$$

The advantage of the redundant index is that it makes permutation symmetries apparent. Example of an electron diffraction pattern of a crystal with hexagonal symmetry for the beam direction $[001]$ is given in Fig. 2.4b.

Hexagonal close-packed three-dimensional structure is formed by placing consecutive layers in the A, B, or C positions (Fig. 2.4c). No two successive layers are allowed in identical positions. In addition, apostrophe symbol is used to represent rotated layer. For example in Fig. 2.4d motif of the *h*-BN monolayer is shown for A and A' positions. Alternative to ABC notation of the different stacking sequences is Ramsdell *n*X notation where *n* is identity period and X stands for lattice type [85]. In the literature ABC labelling is commonly used for *h*-BN, while Ramsdell notation is typical for chalcogenides. Different structural modifications of an element or compound, each of which may be regarded as built up by stacking layers of nearly identical composition are known as polytypes [86].

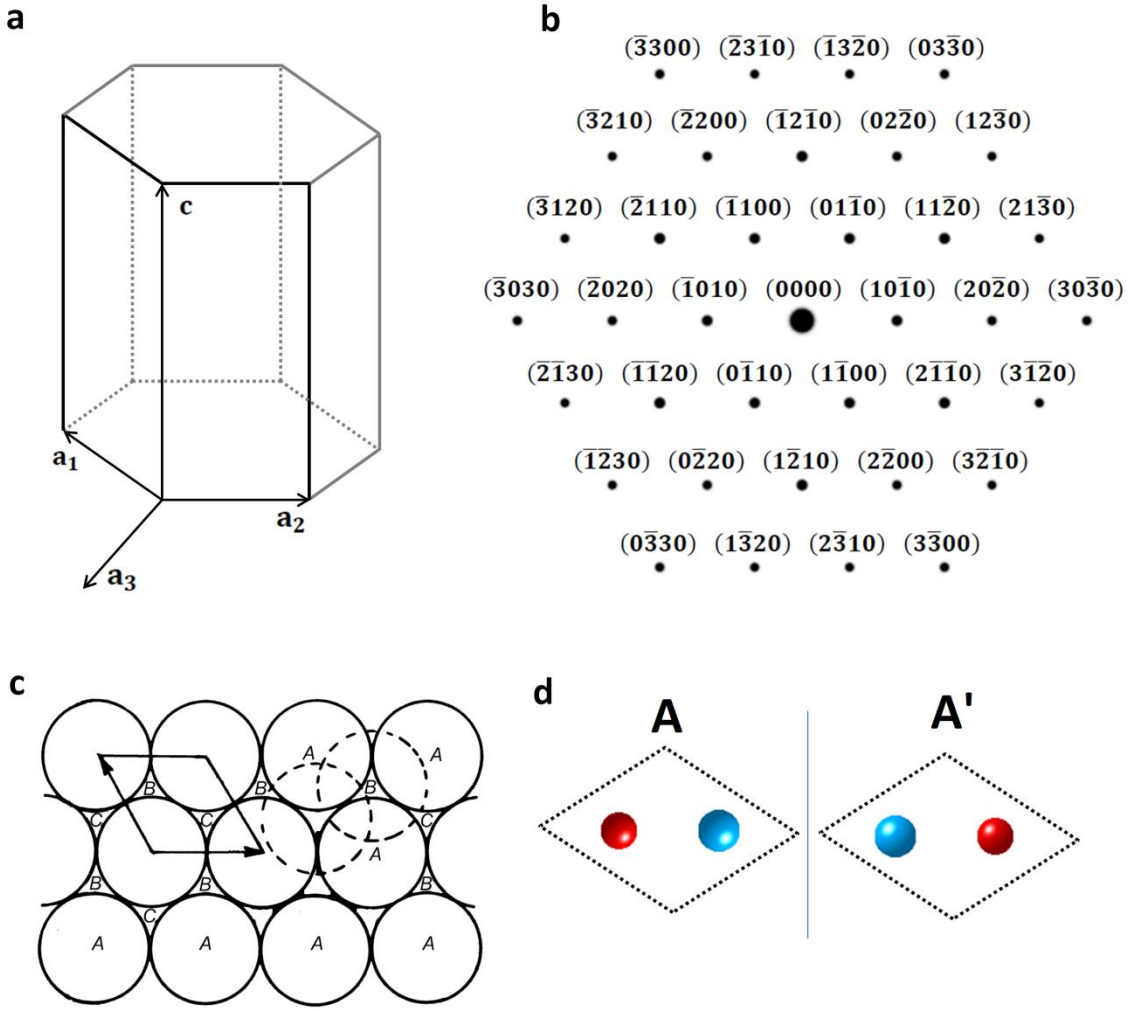


Figure 2.4. (a) Schematic of hexagonal lattice system. (b) Labelled electron diffraction pattern of hexagonal lattice system. Electron beam direction is [**001**] which is parallel to vector **c** in part a. (c) The close packing of spheres in a plane [87]. (d) Motif of *h*-BN monolayer for A and A' stacking.

Diffraction mode is one of the primary modes in CTEM making the acquisition of electron diffraction patterns a straightforward procedure. Typically it is only necessary to analyse specific areas of the specimen. In order to select a necessary area an aperture is placed in a plane conjugate with the specimen creating a virtual aperture in the specimen plane. The smallest physical size of the typical aperture is ~10μm in diameter, which after ~60 times demagnification back to the plane of the specimen gives a minimum selected area of ~150 nm. Electron diffraction of the specific area of the sample is known as selected area electron diffraction (SAED).

2.2.4 Image Formation Theory

For a better understanding of the imaging process and the intuitive interpretation of the images it is useful to consider a linear image model. Although transmission electron imaging does not follow such simple model with great precision, under certain condition it can be treated as reliable approximation.

The basic principle of the linear image model states that the actual recorded image intensity $g(\boldsymbol{r})$ is related to the ideal image of the object $f(\boldsymbol{r})$ by a linear convolution of the object function with the point spread function $h(\boldsymbol{r})$ of the instrument:

$$g(\boldsymbol{r}) = f(\boldsymbol{r}) \otimes h(\boldsymbol{r}) = \int f(\boldsymbol{r}')\, h(\boldsymbol{r} - \boldsymbol{r}')d\boldsymbol{r}' \qquad \text{Eq. 2.14}$$

where $\boldsymbol{r} = (x, y)$ is a two dimensional position vector in the image plane. The point spread function (PSF) of the instrument is the image of an isolated point in the specimen. Eq. 2.14 can be re-written in reciprocal space by applying Fourier Convolution Theorem:

$$G(\boldsymbol{k}) = F(\boldsymbol{k})H(\boldsymbol{k}) \qquad \text{Eq. 2.15}$$

$G(\boldsymbol{k})$, $F(\boldsymbol{k})$ and $H(\boldsymbol{k})$ are the Fourier Transforms of $g(\boldsymbol{r})$, $f(\boldsymbol{r})$ and $h(\boldsymbol{r})$, respectively. $H(\boldsymbol{k})$ is also known as the transfer function or modulation transfer function.

2.2.4.1 Conventional Transmission Electron Microscopy

In order to get better understanding of the phase contrast formation mechanism in CTEM it is useful to consider how the electron function changes during its passage through the column (Fig. 2.5).

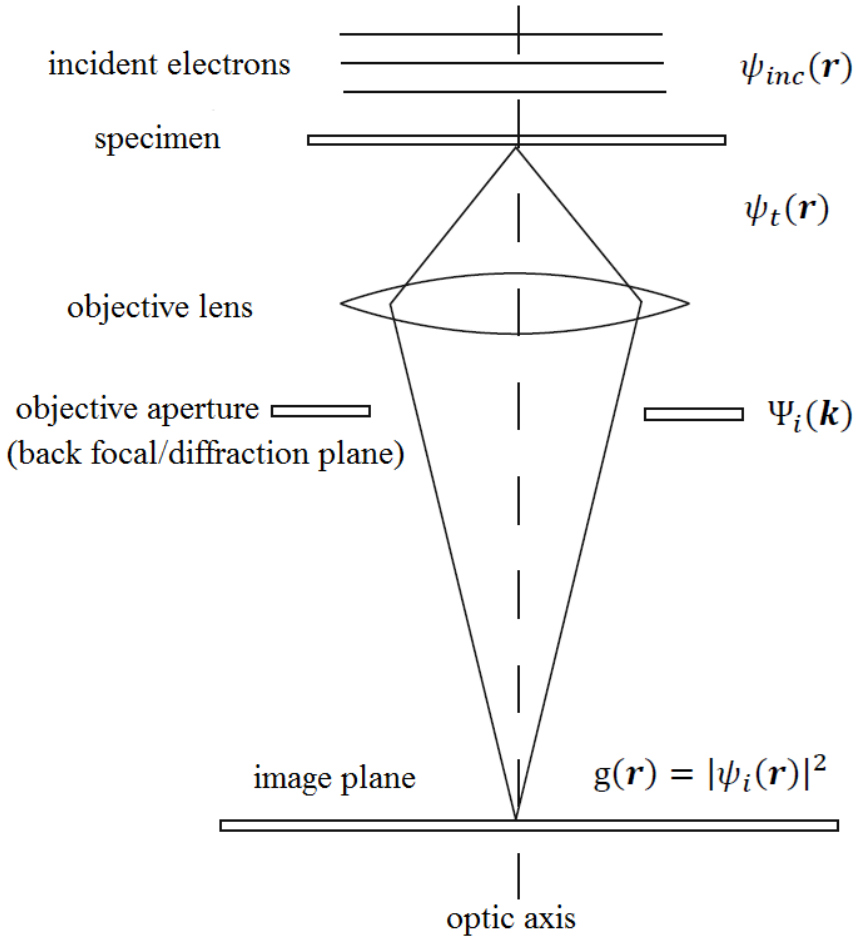


Figure 2.5. Schematic of the CTEM column with positions of the imaging wave functions [71].

The condenser lenses produce plane waves, $\psi_{inc}(\boldsymbol{r})$, which interact with the specimen. Provided that the specimen is very thin (approximation which is particularly valid for the treatment of 2D nanomaterials), the incident electrons pass through the specimen only with small deviations (phase-object approximation). Hence, the effect of the specimen can be modelled as a simple transmission function, $t(\boldsymbol{r})$, which can be related to the projected potential of the specimen, $v_z(\boldsymbol{r})$.

$$t(\boldsymbol{r}) \sim \exp[-i\sigma_e v_z(\boldsymbol{r})] \qquad \text{Eq. 2.16}$$

where σ_e is an appropriate scaling factor. The electron function after passing through the specimen becomes

$$\psi_t(\boldsymbol{r}) = \psi_{inc}(\boldsymbol{r})t(\boldsymbol{r}) \qquad \text{Eq. 2.17}$$

The action of the ideal lens is mathematically represented by Fourier Transform (FT) and the effect of the lens by an additional phase shift. Then the electron function at the back focal plane becomes

$$\Psi_t(\boldsymbol{k}) = \mathrm{FT}\big(\psi_t(\boldsymbol{x})\big) \qquad \text{Eq. 2.18}$$

and adding aberrations effect

$$\Psi_i(\boldsymbol{k}) = \Psi_t(\boldsymbol{k}) \exp[-i\chi(\boldsymbol{k})] \qquad \text{Eq. 2.19}$$

Finally, in the image plane the wavefunction becomes

$$\psi_i(\boldsymbol{r}) = \mathrm{FT}^{-1}\big(\Psi_i(\boldsymbol{k})\big) \qquad \text{Eq. 2.20}$$

and the image intensity is

$$\mathrm{g}(\boldsymbol{r}) = |\psi_i(\boldsymbol{r})|^2 = |\psi_t(\boldsymbol{r}) \otimes h(\boldsymbol{r})|^2 \qquad \text{Eq. 2.21}$$

where $h(\boldsymbol{r}) = \mathrm{FT}^{-1}\big(H(\boldsymbol{k})\big) = \mathrm{FT}^{-1}(\exp[-i\chi(\boldsymbol{k})])$ is the complex point spread function of the objective lens.

The transmission function can be further simplified as

$$t(\boldsymbol{r}) \sim \exp[i\sigma_e\, v_z(\boldsymbol{r})] \sim 1 + \sigma_e v_z(\boldsymbol{r}) + \cdots \qquad \text{Eq. 2.22}$$

This is known as weak phase object (WPO) approximation. Since the incident wave function is a plane wave ($\psi_{inc}(\boldsymbol{r}) \approx 1$), transmitted wave function becomes

$$\psi_t(\boldsymbol{r}) = \psi_{inc}(\boldsymbol{r})t(\boldsymbol{r}) \sim 1 + \sigma_e v_z(\boldsymbol{r}) \qquad \text{Eq. 2.23}$$

Substituting the above results into the equation Eq. 2.15 for image intensity the following result is obtained

$$\mathrm{g}(\boldsymbol{r}) = |\psi_t(\boldsymbol{r}) \otimes h(\boldsymbol{r})|^2 = 1 + \sigma_e v_z(\boldsymbol{r}) \otimes [ih(\boldsymbol{r}) - ih^*(\boldsymbol{r})] + \mathcal{O}(v_z^2)$$

$$\approx 1 + 2\sigma_e v_z(\boldsymbol{r}) \otimes h_{WP}(\boldsymbol{r}) \qquad \text{Eq. 2.24}$$

where $\mathcal{O}(v_z^2)$ represents higher order terms in $v_z(\boldsymbol{r})$ which are ignored for WPO. $h_{WP}(\boldsymbol{r})$ is the point spread function in the WPO approximation. It is more insightful to deal with transfer function, $H_{WP}(\boldsymbol{k})$, which is

$$H_{WP}(\boldsymbol{k}) = \mathrm{FT}\big(h_{WP}(\boldsymbol{r})\big) = \sin\big(\chi(\boldsymbol{k})\big) \qquad \text{Eq. 2.25}$$

The oscillatory transfer function means that different spatial frequencies will be transferred with different contrast. ($H_{WP}(\boldsymbol{k}) > 0 \rightarrow$ white; $H_{WP}(\boldsymbol{k}) < 0$). Such behaviour leads to images which are difficult to interpret. Ideally, the transfer function must be approximately flat for a significant region near its minimum or maximum i.e. $\big|\sin\big(\chi(\boldsymbol{k})\big)\big| \approx 1$. Assuming that the limiting resolution factor is C_s (which is true for CTEM) and astigmatism is fully corrected, $\chi(\boldsymbol{k})$ is

$$\chi(\boldsymbol{k}) = \pi\lambda\boldsymbol{k}^2(0.5C_s\lambda^2\boldsymbol{k}^2 - \Delta f) \qquad \text{Eq. 2.26}$$

Defocus values, satisfying condition $\big|\sin\big(\chi(\boldsymbol{k})\big)\big| \approx 1$ for the above equation, are

$$\Delta f = -\sqrt{2n_D - 0.5C_s\lambda}; \quad n_D = 1,2,3 \ldots \qquad \text{Eq. 2.27}$$

The special case of $n_D = 1$ is referred as Scherzer defocus, Δf_{Sch}. The use of higher-order bands leads to improved resolution. Moreover bands can be used for exit-wave reconstruction from a defocus series [83]. Nonetheless, for everyday imaging it is more convenient to use Δf_{Sch}. If resolution is an issue, it is more practical to use an aberration-corrected CTEM. Example of $H_{WP}(\boldsymbol{k})$ for different defocus values is given in Fig. 2.6.

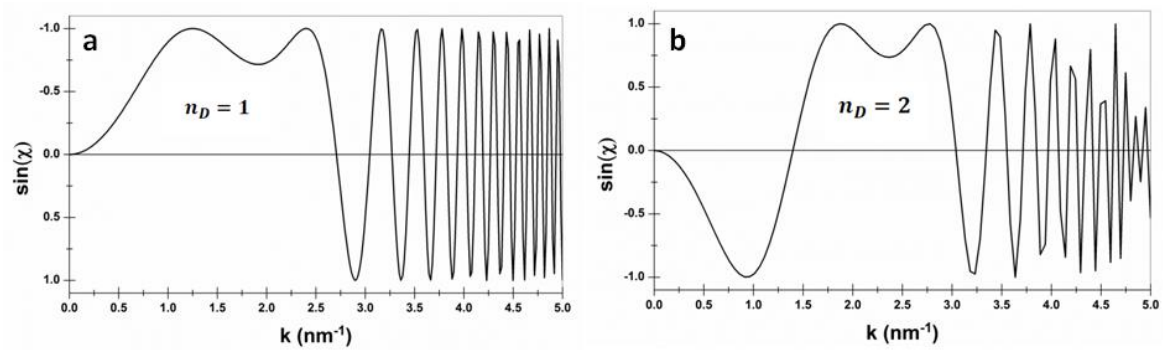


Figure 2.6. The phase contrast transfer function for a weak phase object as a function spatial frequency for different values of defocus (a) $\boldsymbol{n_D = 1}$, (b) $\boldsymbol{n_D = 2}$. $\boldsymbol{C_s = 1.5}$ **mm**. All other aberrations are set to zero. Accelerating voltage is 80 kV.

The first zero crossing in Fig. 2.6a corresponds to the maximum frequency, k_{max}, transferred with the same sign for Δf_{Sch}. It is given by:

$$k_{max} = \left(\frac{6}{C_s \lambda^3}\right)^{\frac{1}{4}} \qquad \text{Eq. 2.28}$$

$\theta_{max} = \lambda\, k_{max}$ is the Scherzer aperture. Eq. 2.28 can be conveniently used to estimate maximum C_s tolerated in order to transfer specific spatial frequencies. This approach was applied to the *h*-BN family of planes whose values are taken as k_{max} (Table 2.3). Table 2.3 also shows the scattering angles, θ_{max}, and Δf_{Sch} to demonstrate the expected magnitude of these parameters at 80 keV. The transfer function H_{WP} is zero for the spacing at k_{max}. Hence, for hexagonal lattice and atomic resolution (6.95 nm^{-1}) the minimum transferred spatial frequency must be higher than the $\{10\bar{1}0\}$ and $\{11\bar{2}0\}$ family of planes, correspondingly. Typical C_s values for a CTEM instrument are 1.5 mm and higher. The magnitudes of C_s in Table 2.23 indicate that for high quality atomic resolution imaging of *h*-BN basal planes at 80 keV an aberration corrector is required. Similar results can be obtained for the other layered materials investigated in this thesis.

Table 2.3. This table shows reciprocal space values ($\boldsymbol{k_{max}}$ column) for the *h*-BN family of planes. $\boldsymbol{\theta_{max}}$ column shows corresponding scattering angles. $\boldsymbol{C_s}$ column shows the maximum values of spherical aberration coefficients necessary to transfer spatial frequency corresponding to the particular reflection. The final column shows values of Scherzer defocus for corresponding $\boldsymbol{C_s}$ values. Accelerating voltage is 80 kV. Beam direction is [001].

$g_{\{hkil\}}$	k_{max} (nm^{-1})	θ_{max} (mrad)	C_s (μm)	Δf_{Sch} (nm)
$g_{\{10\bar{1}0\}}$	4.64	9.1	1700	-67
$g_{\{11\bar{2}0\}}$	8.03	15.8	189	-22
$g_{\{20\bar{2}0\}}$	9.27	18.3	106	-17
$g_{\{21\bar{3}0\}}$	12.3	24.2	35	-9.5

2.2.4.2 Scanning Transmission Electron Microscopy

In STEM a focused electron beam is scanned across the specimen. The scattered electrons are then collected by two or more detectors. The two main detectors in STEM are the bright field (BF) detector and the annular dark field (ADF) detector (Fig. 2.7). The typical angular range of the BF detector is below 30 mrad, while for ADF the inner angle is ~40 mrad and the outer angle is ~200 mrad. In certain microscopes instead of a single ADF detector there are two dark field detectors: medium angle annular dark field (MAADF) detector (~40 – 200 mrad) and high angle annular dark field (HAADF) detector (80 – 200 mrad).

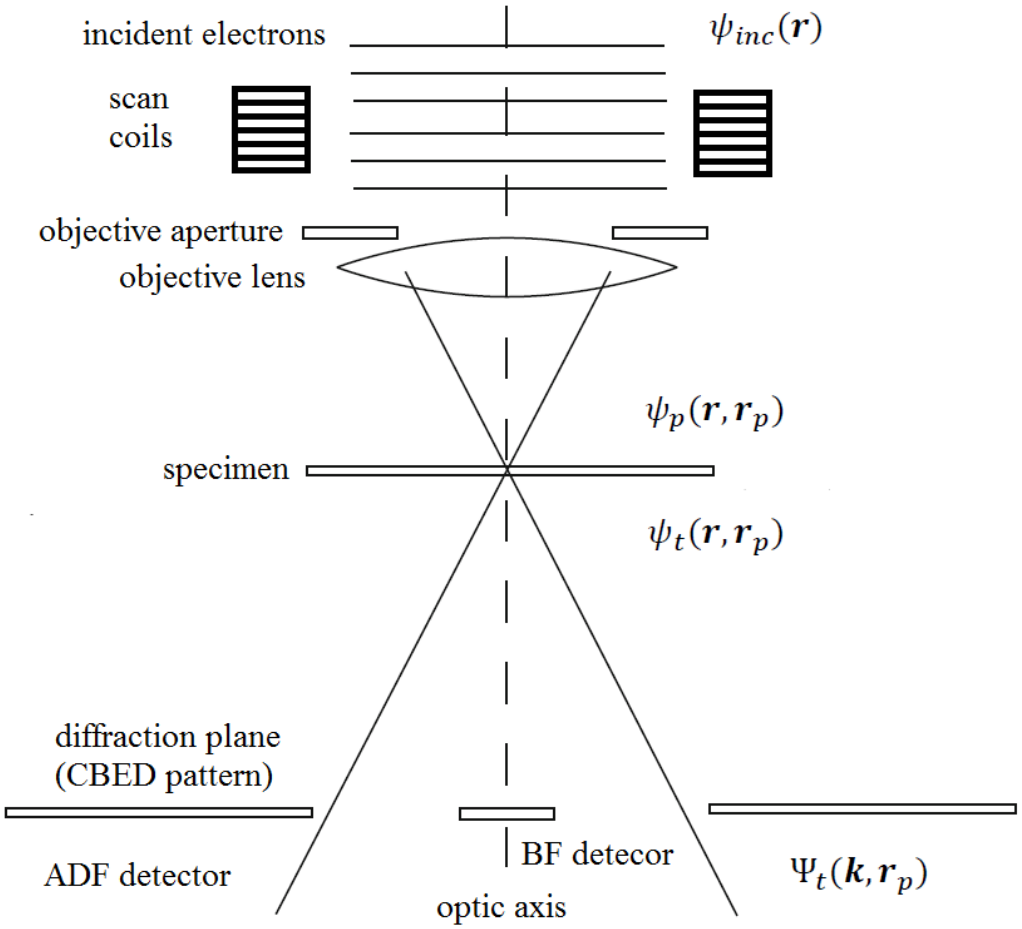


Figure 2.7. Schematic of the STEM column with positions of the imaging wave functions [71].

For understanding STEM image formation, similarly to a CTEM we should consider the propagation of the electron waves (Fig. 2.7). Since $\psi_{inc} \approx 1$, the equation for a focused probe becomes the FT of the aberration function with integration limits defined by the size of objective aperture.

$$\psi_p(\boldsymbol{r},\boldsymbol{r}_p) = A_p \int_0^{k_{max}} \exp[-i\chi(\boldsymbol{k})] \exp\big[-2\pi i\boldsymbol{k}\cdot(\boldsymbol{r}-\boldsymbol{r}_p)\big] d\boldsymbol{k} \qquad \text{Eq. 2.29}$$

where A_p is a normalisation constant, while$\boldsymbol{r}_p$ represents the probe scanning effects. Once again the specimen can be represented by the transmission function $t(\boldsymbol{r})$ so transmitted wave function becomes

$$\psi_t(\boldsymbol{r}, \boldsymbol{r}_p) = t(\boldsymbol{r})\psi_p(\boldsymbol{r}, \boldsymbol{r}_p) \qquad \text{Eq. 2.30}$$

Thus, the wavefunction diffracted onto the detector plane is

$$\Psi_t(\boldsymbol{k}, \boldsymbol{r}_p) = \mathrm{FT}\left(\psi_t(\boldsymbol{r}, \boldsymbol{r}_p)\right) \qquad \text{Eq. 2.31}$$

The intensity of the wave function $\left|\Psi_t(\boldsymbol{k}, \boldsymbol{x}_p)\right|^2$ as a function of scattering angle corresponds to the convergent beam electron diffraction (CBED) pattern. The final STEM image signal, $\mathrm{g}(\boldsymbol{x}_p)$ for single probe position $\boldsymbol{x}_p$ is the integral of the CBED over the whole detector.

$$\mathrm{g}(\boldsymbol{x}_p) = \int \left|\Psi_t(\boldsymbol{k}, \boldsymbol{r}_p)\right|^2 D(\boldsymbol{k}) d\boldsymbol{k} \qquad \text{Eq. 2.32}$$

where $D(\boldsymbol{k})$ is the detector function

$$\begin{aligned} D(\boldsymbol{k}) &= 1 \quad \text{for} \quad k_{D_{min}} \leq k \leq k_{D_{max}} \\ &= 0 \quad \text{otherwise} \end{aligned} \qquad \text{Eq. 2.33}$$

where $\lambda k_{D_{min}}$ and $\lambda k_{D_{max}}$ are the inner and outer angles of the ADF detector.
Equation 2.32 does not offer straightforward interpretation of the image contrast in STEM. Nonetheless, it strongly indicates the importance of the detector function. On this premises, it is necessary to consider BF-STEM and ADF-STEM separately.

The order of the optical components of the STEM is reversed from that of the CTEM. This allows BF-CTEM and BF-STEM to be related via the reciprocity theorem [88] which states that the electron intensities and ray paths in the microscope remain the same if their direction is reversed and the source and detector are interchanged. Reciprocity applies to all orders of elastic interaction of the electrons and the specimen.

Unlike BF-STEM and BF-CTEM, ADF STEM is a transversely incoherent process. Due to the size of the ADF detector, the interference features at the detector's plane are averaged out suppressing any coherent phase information. As a consequence, the collected intensity will be a fraction of the probe intensity scattered by the specimen. The corresponding linear image model is:

$$g(\boldsymbol{r}_p) = \left|\psi_p(\boldsymbol{r}, \boldsymbol{r}_p)\right|^2 \otimes \mathcal{O}(\boldsymbol{r}_p) \qquad \text{Eq. 2.34}$$

where $\mathcal{O}(\boldsymbol{r}_p)$ is ADF object function representing the fraction of intensity which the specimen is able to scatter in a point $\boldsymbol{r}_p$. The probe intensity, $\left|\psi_p(\boldsymbol{r}, \boldsymbol{r}_p)\right|^2$, is a point spread function and its FT is the transfer function, H_{ADF}. The shape of H_{ADF} is remarkably different from the H_{WP} (Fig. 2.8). H_{WP} is typically a monotonically positive decaying function. Hence, ADF-STEM does not suffer from contrast oscillations upon changes in defocus.

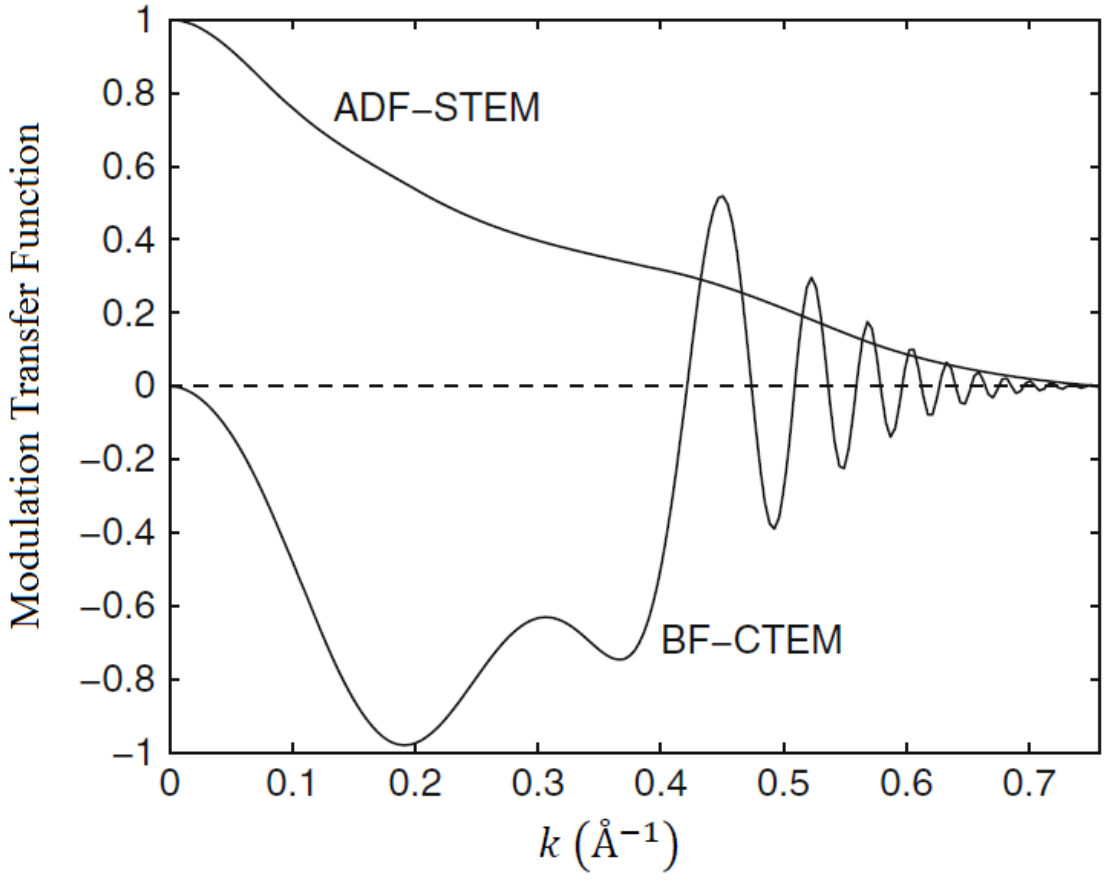


Figure 2.8. Comparison of ADF-STEM and BF-CTEM transfer functions for the same spherical aberration, $\boldsymbol{C_s} = \mathbf{1.2\ mm}$, at 200 keV [71].

The intensity of electrons scattered at high angles can be treated as following the Rutherford model with total intensity proportional to the atomic number squared, Z^2. In reality a lower exponent of 1.7 due to screening effects is more reasonable [89]. As a

result HAADF-STEM is often referred as Z-contrast imaging with Z-dependence much stronger than in CTEM images.

In addition to the Bragg scattering, it is important to consider the effect of thermal lattice vibrations which attenuate the strength of elastically scattered electrons. Attenuation results in diffuse intensity, known as thermal diffuse scattering (TDS). TDS is an incoherent process which dominates the signal at high scattering angles (i.e. HAADF signal).

In summary:

1. BF STEM. Small-axial detector is used to collect elastically scattered and transmitted electrons. Coherent imaging mode.
2. MAADF STEM. Annular detector with a small inner cut-off is used to collect primarily elastically scattered (Bragg diffraction) electron. Incoherent imaging mode. Weak Z-contrast.
3. HAADF STEM. Annular detector with a large inner and outer cut-offs is used to collect primarily inelastically scattered electrons. Incoherent imaging mode. Strong Z-contrast.

2.2.5 Aberration corrected microscopy

Scherzer in 1936 proved that any electron optical system will always suffer from positive spherical aberration and chromatic aberration if simultaneously:

1. The optical system is rotationally symmetric.
2. The system produces a real image of the object.
3. The fields of the system do not vary with time.
4. There is no charge present on the electron-optical axis.

Therefore to achieve C_s and C_c correction one of the above conditions must be broken. So far breaking rotational symmetry was the most successful approach towards C_s correction. The requirement to produce a real image cannot be circumvented. Time-varying fields are used in practise in particle accelerators to correct C_c. However this technique faces certain challenges when applied to electron microscopes. Similarly, adding charges to the electron optical axis was attempted but without much success due to the technical difficulties.

The practical method to produce negative C_s which offsets positive C_s of the round magnetic lens is achieved using multipole lenses. There are two commercially

successful designs: quadrupole-octupole corrector (NION) and hexapole corrector (CEOS).

Let's first consider the principles of the quadrupole-octupole corrector. The deflection of the electrons travelling through the octupole varies cubically with distance from the optical axis (i.e. the octupole acts directly on third order aberrations). Unfortunately on octupole produces negative and positive C_s-effects along different directions. Therefore, to obtain negative C_s it is necessary to produce a highly elliptical beam first which then passes through the octupole along the line of negative C_s (arbitrary x-direction). A round beam can be turned into an elliptical and back using quadrupole lenses. This protocol must then be repeated in order to correct C_s along the y-direction. Hence, overall correction is achieved by the combination of quadrupole and octupole lenses.

A long multipole element has an additional second order effect which can be understood in terms of several thin multipoles assembled together. Starting with the round beam, each thin mulitupole changes its shape. As a result rays that are further from the axis are deflected stronger. The overall effect is one power higher than in the radial direction than the first order effect. This approach is utilised in hexapole correctors. The first order effect of a hexapole is quadratic in the radial direction and three-fold azimuthally, but the second order effect is cubic in the radial direction and uniform azimuthally. Of course in the hexapole corrector first order effects must be removed. This is achieved by the use of two hexapoles rotated at 60^o with respect to each other. However, the effects of two hexapoles must occur in equivalent optical planes. As a result transfer lenses are placed between the two hexapoles.

The theory behind aberration correctors is fairly straightforward with initial corrector designs dating back to Scherzer. Nonetheless successful implementation of correctors proved to be somewhat difficult. Several challenges had to be overcome before improved resolution was achieved. They are: stability of electronics, a detailed understanding of the role of parasitic aberration and suitable algorithms and computational performance for quickly and accurately diagnosing aberrations. Parasitic aberrations are geometric aberrations introduced by the imperfections in the corrector. It means that functioning C_s-corrector must not only be able to correct C_s but also lower order parasitic aberrations. This requires placing additional multipole elements in the column and further increasing the complexity of the aberration corrected microscopes.

The latest generation of aberration correctors offers correction of aberration as high as 5th order. In many cases, it makes chromatic aberration the limiting aberration. Although working C_c correctors have been designed and tested its commercial realisation is only starting.

2.2.6 Electron Energy Loss Spectroscopy

The interaction of the fast incident electrons with the specimen can be sub-divided into the two broad categories: electron-nucleus (elastic) and electron-electron (inelastic). If the incident beam is monoenergetic, the inelastically scattered portion of the transmitted beam can be spectroscopically dispersed as a function of its energy loss. Electron energy loss spectroscopy (EELS) involves analysis of the energy distribution of the inelatically scattered electrons. An example of a typical EELS spectrum is given in Fig. 2.9. In a thin specimen most of the transmitted electrons are elastically scattered producing the most intense feature of spectrum called zero loss peak. The full width half maximum of the zero loss peak is defined as the spectral resolution and, in a well-tuned spectrometer, is limited by the energy spread of the electron source. Due to the spread of the zero loss peak it also contains phonon-scattered electrons whose interaction energies are 10-100 meV. EELS extends over 1000 eV of energy loss and can be subdivided into two regions: low loss and high loss.

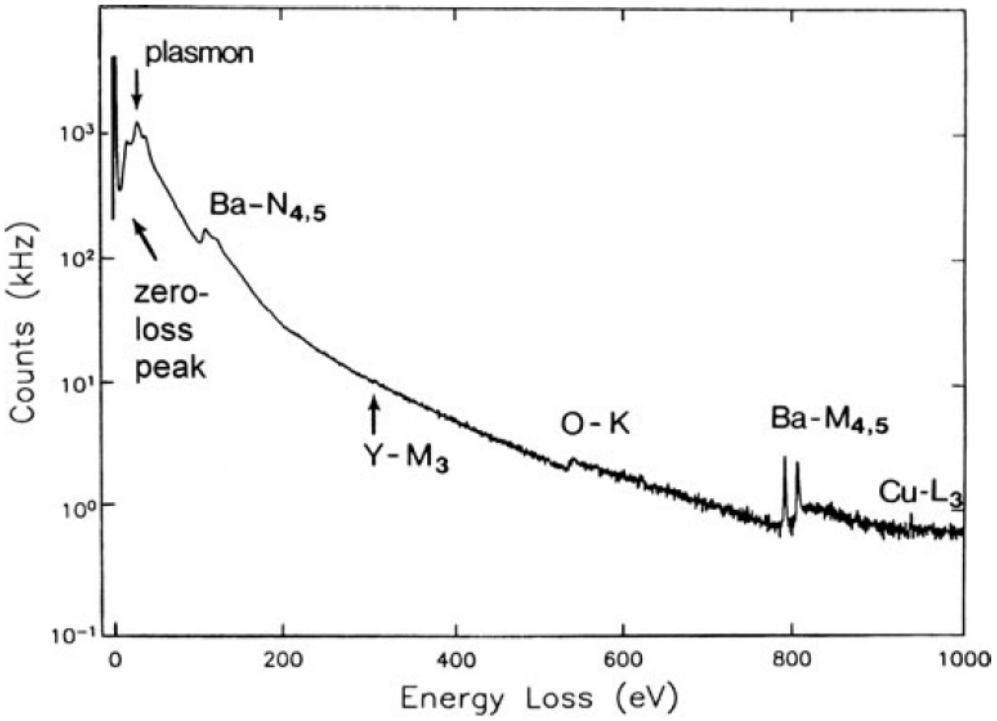


Figure 2.9. EELS of a high-temperature superconductor ($YBa_2Cu_3O_7$) showing zero-loss and plasmon peaks and ionization edges arising from each element. Image is reproduced from [90].

The low loss region of the EELS extends from zero loss peak to about 50 eV. The dominant features of the low loss EELS are interband transitions and resonant collective excitations (plasmons) of free electrons and electrons in the valence bands. The peak positions of the surface plasmons are sensitive to the sample geometry and can be used to extract structural information about the sample.

The high loss region of the EELS extends from about 50 eV to several thousand eV. It involves electron excitations from localised orbitals on single atomic sites. Hence, this region exhibits ionisation edges which can be used for elemental analysis of the sample. The notation of ionisation edges is based on the standard atomic shell model. Ionisation edges can also display fine structure such as that arising from spin-orbit coupling. The intensity of the fine-structure peaks is a function of chemical bonding and can reveal changes in the electronic structure.

Although EELS can be used in both TEM and STEM configurations, there is particular advantage of STEM mode due to the high spatial resolution approaching atomic. Furthermore the geometry of the ADF detector allows simultaneous sample's image acquisition with accompanying spectrum because portion of the beam can be passed to the EELS detector through the central hole.

Chapter 3: Experimental and Processing Routines

3.1 Samples Preparation

Bulk *h*-BN powder was provided by Saint-Gobain Advanced Ceramics Lauf GmbH with a stated chemical purity >98% *h*-BN, <1.5% O_2, >0.5% B_2O_3. MoS_2, WS_2, TiS_2 powders, isopropanol anhydrous (IPA), N-methyl-2-pyrrolidone anhydrous (NMP) and N-Cyclohexyl-2-pyrrolidone (CHP) were purchased from Sigma-Aldrich and used as received (CAS Nos.: 1317-33-5, 12138-09-9, 12039-13-3, 67-63-0, 872-50-4 and 6837-24-7 respectively). Some of the TiS_2 powder was baked for 3hrs at $T = 200℃$ at atmospheric pressure before use.

The experimental procedure for preparation of 2D nanostructures suspended in solvent is described by Coleman et al [30]. Although the fundamental principle behind chemical exfoliation did not change over the course of the project minor variations were added to the procedure to better suit TEM characterisation.

The basic procedure involved dispersing bulk material in suitable solvent using ultrasonic tip (Ultrawave UP100H, 100W, 30kHz, 100% amplitude, continuous cycle) or ultrasonic bath (Ultrawave U50, 100W, 42kHz) for 1-2 hrs. The initial concentration of the material was 0.5-1 g/L. Following ultrasonication all dispersions were centrifuged for 0.5 hrs at 500 r.p.m. The supernatant was then carefully decanted and TEM samples prepared by drop-casting onto Agar holey-carbon/copper grids (500mesh). While it was possible to use samples prepared this way they usually suffered from two drawbacks: low concentration of the nanoflakes, and low exfoliation yield (the thickness of the nanoflakes was too high). As a result, the above procedure was modified to use only the sonic tip for 2 hrs. After sonication, the suspensions were allowed to settle unperturbed for two days. The supernatant was not centrifuged but deposited directly onto TEM grids. The absence of centrifugation step implied that dispersions had to be handled with extreme care because any rapid movement would lift settled precipitate from the bottom of the vial.

Several solvents were tested for exfoliation. Amongst them the most suitable were isopropanol anhydrous (IPA) and NMP with the last one being the most efficient exfoliating agent. The boiling points of IPA and NMP are 83 ^oC and 203 ^oC respectively. NMP's high boiling point can cause contamination problems during imaging of the

samples. In order to avoid that, the grids were left after deposition in ambient conditions for at least 12 hrs to allow most of the solvent to evaporate and then baked at 135^{o}C in vacuum for at least 3 hrs. Typically, for successful atomic resolution STEM imaging the grids were additionally baked the entire night before the microscope session. This procedure was used for *h*-BN, MoS_2, WS_2 and TiS_2 nanoflakes.

Hexabenzocoronene dispersions were prepared using a Branson 1510 sonic bath (80W, 42kHz) in CHP [91]. For the ADF STEM characterisation dispersions were drop-cast onto holey-carbon/copperTEM grids with pre-deposited and baked *h*-BN grids and further baked at 60 ^{o}C in vacuum for 5 hrs. In addition, control samples were prepared where pure CHP was dropped onto pre-deposited *h*-BN grids and baked at 60 ^{o}C in vacuum for 5 hrs. For the HRTEM characterisation dispersions were drop-cast onto an ultrathin carbon support on a copper TEM grid (Agar Scientific, S186-4) and baked at 60 ^{o}C in vacuum for 5 hrs. The carbon film is less than 3nm thick, according to manufacturer.

3.2 Imaging

Conventional TEM and electron diffraction were carried out using a JEOL2010 microscope operated at 200 keV.

HRTEM images were acquired using the double aberration corrected JEOL 2200MCO. The instrument was operated at 80 keV with spherical aberration set to $C_3 \approx 3\mu$m. Imaging was assisted by Judy Kim and Valeria Nicolosi.

ADF STEM imaging of TiS_2 nanoflakes was performed using the double aberration corrected JEOL 2200MCO operated at 80 keV (probe current of ~45 pA, probe convergence angle of 26 mrad and collection half angle of 60-180 mrads). Imaging was assisted by Valeria Nicolosi.

ADF STEM imaging of *h*-BN and MoS_2 was done using a JEM-ARM200F operated at 80 keV (probe current of ~34 pA, probe convergence angle of 22 mrad and collection half angle of 45-170 mrads and 55-170 mrads). Imaging was assisted by Eiji Okunishi.

ADF STEM imaging of *h*-BN nanoflakes and HBC was performed using a Nion UltraSTEM 100 aberration-corrected STEM microscope operated at 60 keV (probe current of ~50 pA, probe convergence angle of 30 mrad and collection half angle of 41-195 mrads). Imaging was assisted by Mervyn Shannon.

ADF STEM imaging of *h*-BN, MoS_2 and WS_2 nanoflakes was performed using a Nion UltraSTEM 100 aberration-corrected STEM microscope operated at 60 keV (probe current of ~50 pA, probe convergence angle of 30 mrad and collection half angle of 78-195 mrads). Imaging was assisted by Mervyn Shannon.

3.3 Image Processing

Processing of images after acquisition must be done with extreme care to ensure absence of artefacts in the post-processed images. Here several types of filters are discussed assessing their suitability for improving the quality of the images. Mathematically, filtering an image ($g(\boldsymbol{r})$) using a filter ($H_F(\boldsymbol{k})$), can be written as

$$g_{Filtered}(\boldsymbol{r}) = \mathrm{FT}^{-1}\{\mathrm{FT}(g(\boldsymbol{r}))H_F(\boldsymbol{k})\} \qquad \text{Eq. 3.1}$$

Image filtering does not improve the ultimate resolution and has the sole purpose to remove the noise. Hence any new features observed in the filtered image which are absent in the original image must be treated as artefacts.

A special case of image processing is exit-wave reconstruction [83], which is expected to improve resolution. Nonetheless it must be pointed out that there are certain concerns about this method. In particular, studies of the edge structure based on exit-wave reconstruction require careful interpretation. The main problem is the complex behaviour of atoms at a boundary. The time required to acquire the a typical focal series image stack can vary from 30 seconds up to several minutes, depending on the exposure time and size of the stack. Such periods of time are more than sufficient to modify the edge structures. For the case of graphene movement of individual atoms at an isolated edge has been demonstrated in real time with 1 second temporal resolution [92]. Similar behaviour can be expected for other 2D nanomaterials [93][94]. In general, the exit-phase reconstructed image of an edge can be thought of as “the averaged structure” over the time length of image stack acquisition. The actual edge structure at a particular moment of the data acquisition can be slightly different from the reconstructed image. The other concern is with the reconstruction technique protocol, which due to its complexity, in principle, is capable to introduce artefacts.

3.4 Butterworth Filter

One of the simplest and most reliable filters is the Butterworth filter. This can be expressed by the function:

$$H_{BF}(\boldsymbol{k}) = \frac{1}{1 + \left(\frac{\boldsymbol{k}}{k_0}\right)^{2n}} \qquad \text{Eq. 3.2}$$

where k_0 is the cut off frequency and n is the order of the function. High values of n produce steeper frequency roll-off (Fig. 3.1) which can result in ringing artefacts. Unless otherwise stated, all atomically resolved images in this thesis were filtered using 1st order Butterworth function.

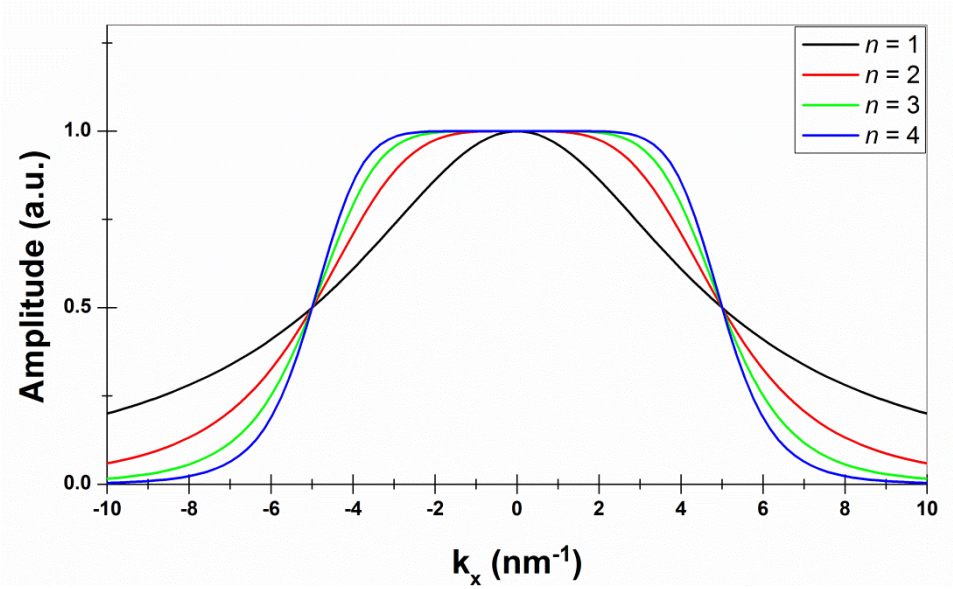


Figure 3.1. Butterworth filter functions of different orders along $\boldsymbol{k_x}$. $\boldsymbol{k_0 = 5\ nm^{-1}}$.

The Butterworth filter is a low pass filter which removes high spatial frequency component from the images. The use of the Butterworth filter is completely justifiable from a scientific point of view. For example the graphene image in Fig. 3.2a has $\{11\bar{2}0\}$ ($8\ nm^{-1}$) as its highest resolved reflection (Fig. 3.2b), while its frequency space extends to $\sim 20\ nm^{-1}$. The Butterworth filter can be used in these cases to remove the high frequency noise only. Figs. 3.2c,d show the filtered image with its corresponding FFT. As expected, the filtered image does not display any artefacts. In particular, the arrows in the unfiltered image (Fig. 3.2a) point to the region where hexagonal lattice is not seen most likely due to the beam damage and carbon contamination. The filtered

image (Fig. 3.2a) clearly preserves this feature. Unless otherwise stated all atomically resolved experimental images were Butterworth filtered.

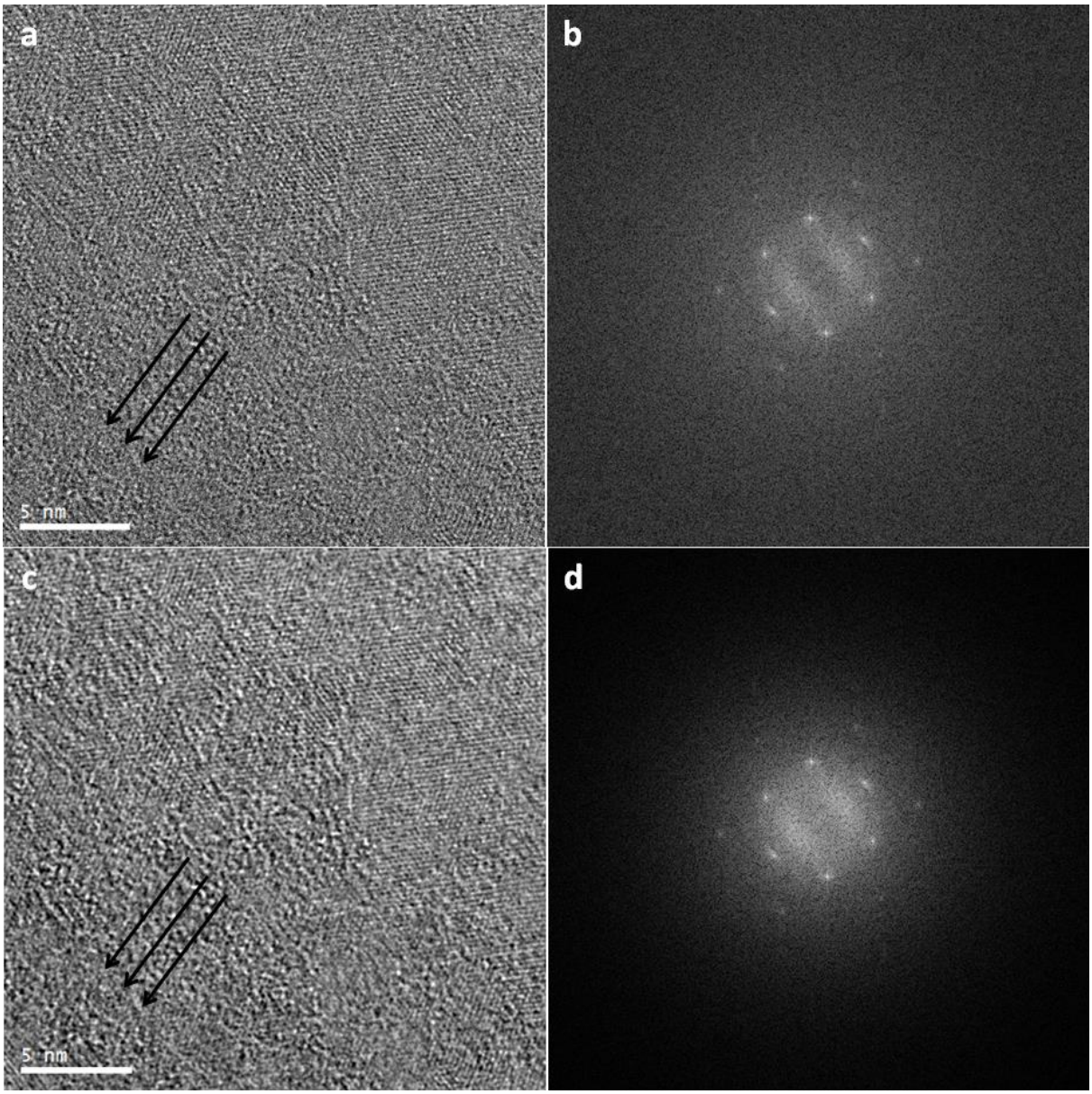


Figure 3.2. (a) Graphene image with corresponding (b) FFT. (c) Butterworth filtered graphene image with corresponding (d) FFT. Arrows indicate amorphised region of the nanoflake.

3.5 Masking in Digital Micrograph

Most of the TEM images are surveyed and processed using Digital Micrograph (DM) software from Gatan, Inc. DM offers certain masking capabilities which are sometimes used for filtering images of 2D nanostructures [95]. It involves the use of circular masks which are centred around the reflections peaks in the reciprocal space (prompt "Apply Mask - Keep masked area executed") (Fig. 3.3a). Fig. 3.3b shows the inverse FFT of Fig.

3.3a which is now the filtered image of the original graphene image in Fig. 3.2a. The filtered image shows several artefacts. First of all the area indicated by the arrows appears crystalline, while it appears amorphous in the original image. As a matter of fact the entire filtered image shows perfect crystallinity which is not true when compared with the original image. Secondly, the image now consists of patches with inversed contrast. It is rather tempting to interpret such pattern as surface undulations in the 2D material producing patches going in and out of focus [95]. However, it is rather straightforward to demonstrate that this patchiness is an artefact. If the diameter of the mask is changed from 0.6 nm^{-1} (Fig. 3.3a) to 1.8 nm^{-1} (Fig. 3.3c) the resulting image (Fig. 3.3d) shows patches with entirely different sizes.

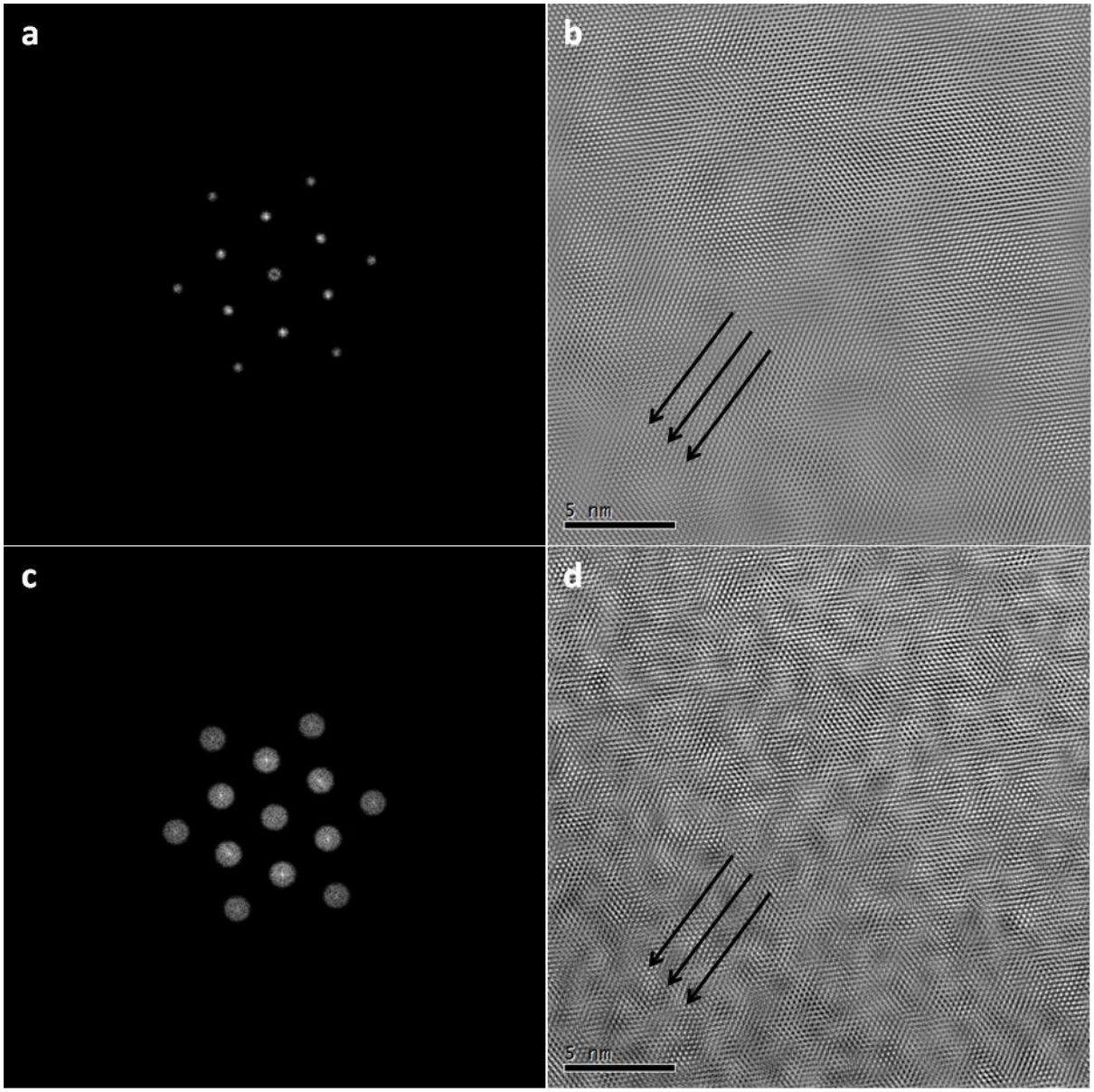


Figure 3.3. (a) (c) Masked FFTs of the graphene image in Fig. 3.2a with corresponding (b), (d) filtered images. Arrows indicate amorphised region of the nanoflake.

3.6 Krivanek's Filter

A special filter was used by Krivanek et al.[96] for filtering STEM images the *h*-BN monolayers, allowing for the chemical identification of all the atomic species in the image. This filter consists of two Gaussian functions:

$$H_{Kr}(\boldsymbol{k}) = A_1 e^{-\frac{\boldsymbol{k}^2}{2c_1^2}} + A_2 e^{-\frac{(|\boldsymbol{k}|-b)^2}{2c_2^2}} \qquad \text{Eq. 3.3}$$

The value of c_i controls the broadness of the function, A_i determines the relative contributions of each part, while b shifts the peak position. Both c_i and A_i control the roll-off characteristics of the filter. The first Gaussian has the effect of cutting out high spatial frequencies while the second one amplifies the contribution of intermediate frequencies. Fig. 3.4 gives an example of the Krivanek's filter for two different c_2^2 values where the contribution of the $\{10\bar{1}0\}$ and $\{11\bar{2}0\}$ family of planes is amplified. Figs. 3.5a,b,c show original and filtered ADF STEM images of a *h*-BN nanoflake. The improvement of the image quality in the filtered version is readily observed. In addition, filtering also helps to compensate for probe tail. This effect can be seen from analysis of the intensity profiles taken across the centre of hexagonal rings (Figs. 3.5d,e,f). In the original (Fig. 3.5a) and weakly filtered (Fig. 3.5b) images the probe tail results in an intensity at the centre of hexagonal rings which is approximately 50% of the nearest peak intensities. In the strongly filtered image (Fig. 3.5c) intensity in the centre of hexagonal rings is reduced to nearly vacuum level.

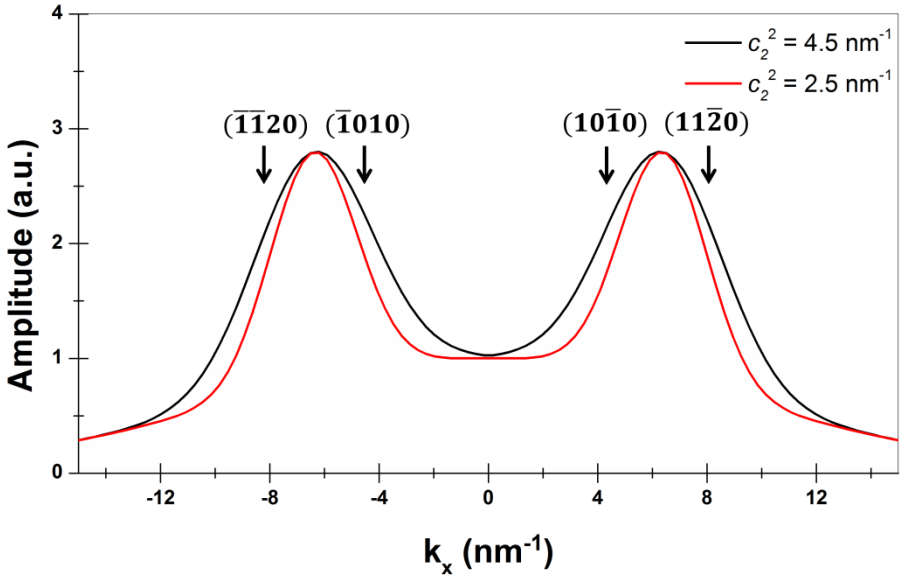


Figure 3.4. Krivanek's filter functions plotted along $\boldsymbol{k_x}$ for different $\boldsymbol{c_2^2}$ values. Other parameters are: $\boldsymbol{A_1 = 1}$, $\boldsymbol{A_2 = 2}$, $\boldsymbol{A_2 = 2}$, $\boldsymbol{c_1^2 = 90\ nm^{-1}}$ and $\boldsymbol{b = 6.4\ nm^{-1}}$. Selected value of the parameter $\boldsymbol{b}$ ensures that transfer of frequencies corresponding to $\{\boldsymbol{10\bar{1}0}\}$ and $\{\boldsymbol{11\bar{2}0}\}$ family of planes is amplified.

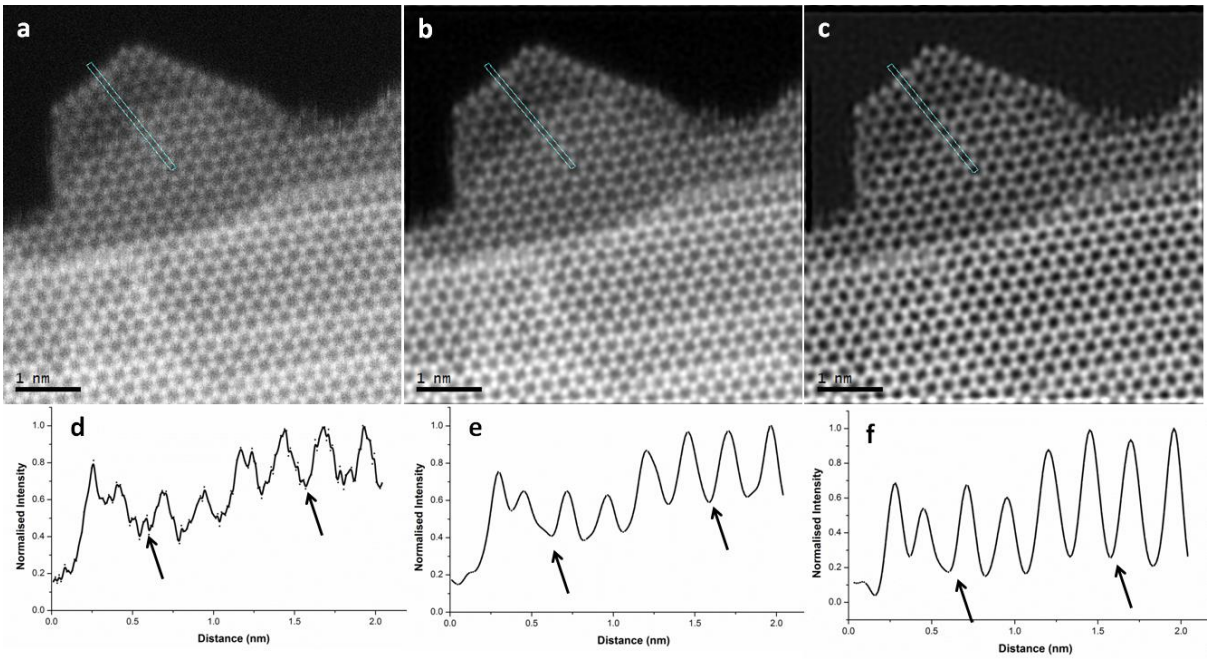


Figure 3.5. (a) Original and (b), (c) filtered ADF STEM images of the *h*-BN nanoflake with corresponding (d), (e), (f) intensity profiles. Arrows indicate intensity at the centre of the hexagonal rings. The filters used in (b) and (c) are shown in Fig. 3.4 with parameters $\boldsymbol{c_2^2 = 4.5\ nm^{-1}}$ and $\boldsymbol{c_2^2 = 2.5\ nm^{-1}}$, correspondingly.

3.7 Image Simulations

Simulation of TEM images can be roughly divided into two main steps: calculating the interaction of the fast moving electrons within the specimen and simulating the action of the microscope. Mathematically, the action of the microscope is sufficiently straightforward to describe as shown in Section 2.2.4.

The interaction of the fast moving electrons with the specimen can be calculated using two different approaches. A method, which is simple conceptually from the physics point of view but computationally rather demanding, is the multislice approach [71]. This involves sectioning the specimen into many slices, which are normal to the incident beam. The projected potential acts as a phase grating for the incident beam (phase-object approximation). As the beam passes through the specimen its amplitude and phase are calculated accordingly during its interaction with each slice. These calculations are based on the Fresnel approximation for the near-field diffraction. While the use of this multislice method is fully intuitive for coherent HRTEM imaging, it becomes less suitable for incoherent images which are dominated by the TDS. A more careful approach to solve this latter case is the method known as frozen phonon approach [71]. The frozen phonon approach is based on the observation that the typical period for lattice vibration is ~10^{-13} s while fast moving electrons transit thin samples within ~10^{-17} s. Therefore it is reasonable to assume that electrons interact with the sample frozen in some configuration. Each passing electron will interact with a different "frozen" configuration. This means that a multislice calculation must be performed for each of these configurations and then averaged in the detector plane for each pixel. The contribution of the TDS is included in the simulations via the Debye-Waller factor, which represents the damping envelope that is applied to the elastically diffracted beam in the diffraction plane. For the Einstein model in which all atoms independently vibrate about their mean lattice positions the Debye-Waller factor is given by:

$$D_W = e^{-B\left(\frac{k}{2}\right)^2} \qquad \text{Eq. 3.3}$$

The parameter $B = 8\pi^2\langle u^2\rangle$ is known as a B-factor and depends on the mean squared thermal displacement, $\langle u^2\rangle$.

The frozen phonon method does however raise some additional questions. In particular, how the frozen phonon scattering (which is a classical elastic process) can be equivalent to the actual phonon scattering (which is quantum process and involves energy exchange)? This paradox is answered in a series of papers which demonstrate that thermally averaged frozen phonon and actual phonon scattering are indeed mathematically equivalent [97][98][99].

A more elegant image simulation approach is based on the fact that electron in a crystal can be described by a sum of Bloch waves which themselves are solutions to the Schrödinger equation [67]. The suitability of the Bloch waves approach for contrast interpretation in HRTEM images was first demonstrated by Fujimoto and Kambe [100][101]. Later it was shown that Bloch waves in combination with absorption effects of TDS [102] can be used to describe incoherent imaging [103][104]. Model describing absorption effects of TDS is now known as absorptive potential [105][106]. When atomic resolution ADF STEM images are acquired along high symmetry directions the effects of channelling can be significant [107]. The channelling itself can be described as the process which enhances the TDS scattering due to the influence of dynamical diffraction [70]. The current absorptive potential model is capable of accommodating channelling effects [108]. The main advantage of the absorptive potential method is that only one calculation is required for each probe position.

In this work all simulations are performed using either QSTEM [109] or Kirkland [71] codes using imaging conditions specified in the section 3.1. These simulation packages are based on the frozen phonon approach. Although the frozen phonon approach is expected to produce quantitative agreement between simulated and experimental images [107] there has not been a systematic study between different simulation packages. The simulated results reported in this work are only expected to achieve qualitative agreement. The main factors hindering a quantitative match between simulation and experiment are the unknown values of the Debye-Waller factors, the contribution of the non-Gaussian probe tail to the experimental column intensities (as shown in Fig. 3.5) and the detector non-uniformity which can affect imaged intensity by 5% [110] and the contrast by up to 10% [111]. The influence of the Debye-Waller factor was further investigated by trial and error. The B-factors in the range of 0.1-4 Å^2 were used for series of simulations of 2D *h*-BN, MoS_2, WS_2 and TiS_2 using QSTEM. It was concluded that magnitude of the Debye-Waller factor does not influence column intensities. Even, if B-factor is not included in the QSTEM input file, a default value proportional to the inverse of the atomic mass will be used. Silicon is taken as the reference value with $B_{Si} = 0.45$ Å^2. Hence for random element

$$B_{element} = 0.45 \frac{28}{m_{element}}$$

For all simulations in this thesis B-factor was set to 1.5 $Å^2$ and results averaged over 20 frozen phonon configurations. Microscope parameters for simulations were matched to those used in experiments (Section 3.2).

Generally, it is believed that ADF STEM ensures direct interpretation of the images minimising significance of the qualitative image simulations. Later in this work it will be demonstrated that in certain cases direct interpretation is not always possible and qualitative image simulation can assist with the ultimate assessment of the results.

Chapter 4: 2D hexagonal boron nitride

In this chapter detailed discussion of the imaging and structural analysis of the liquid exfoliated *h*-BN is given. 2D *h*-BN was the first material investigated in this study, hence, practical advantages and disadvantages of the structural characterisation techniques are discussed to a greater length.

4.1 Introduction

There are three known polymorphs of boron nitride: α-BN (*h*-BN), β-BN (cubic-BN), and γ-BN (wurtzite-BN). Amongst them *h*-BN is most commonly used due to its unique combination of properties: low density, high-temperature stability, chemical inertness and low electrical conductivity. Its major applications include high temperature solid lubricant and component for cosmetic applications [112]. Deposited as thin films *h*-BN has a number of additional applications:

- restricted area boron-diffusion source [113]
- insulator in a metal-insulator-semiconductor (MIS) memory diode [113]
- voltage limiter in integrated circuits [114]
- thin film coating to increase hardness or as protective coating against oxidation of base material [112]

Structurally, *h*-BN consists of sp^2 bonded two-dimensional honeycomb layers stacked in arrangement known as AA$^{'}$ stacking, where nitrogen and boron are alternately stacked on top of each other as shown in Fig. 4.1. Its lattice parameters are {0.250 nm, 0.250 nm, 0.666 nm, π/2, π/2, π/3}[115].

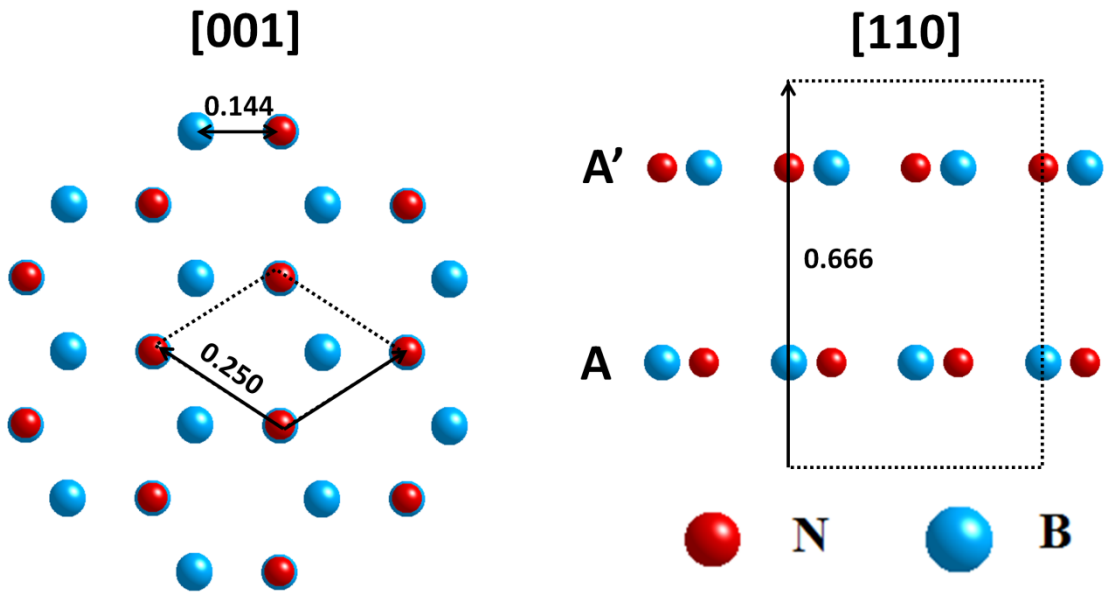


Figure 4.1. Structural model of the bulk *h*-BN (AA'). View along [001] shows the projected structures recorded in the atomically resolved images. View along [110] unambiguously shows stacking sequences. The interlayer distance of [110] view is shown to scale with respect to the interatomic distances of the [001] view. Dashed lines are used to indicate unit cell.

The current knowledge about the electronic properties of bulk *h*-BN is somewhat controversial. Most of theoretical studies [116][117][118] predict an indirect band-gap in the region of 3-5 eV, while the most recent experimental measurements [119] based on exciton-related luminescence indicate direct band-gap of approximately 5.8 eV with the potential to be used as a laser active material in ultraviolet region. The electronic properties of *h*-BN monolayers have not yet been investigated experimentally. Nonetheless, partially exfoliated *h*-BN was successfully employed as a substrate in graphene-based field effect transistors [120] and a top-gate dielectric [121]. Several theoretical investigations showed the possibility of spontaneous magnetization [122] and transition from semiconductor to half-metal [123] induced by the presence of vacancies in *h*-BN monolayers. Modulation of the band-gap through modification of the edge structure in *h*-BN nanoribbons [124][125] has also been theoretically predicted.

Shortly after discovery of graphene, Novoselov et al reported 2D *h*-BN which was also obtained by micromechanical cleavage of the 3D bulk crystal [9]. Prior to this publication the existence of monolayers of *h*-BN was already known, however always formed on crystalline highly-ordered transition metal surfaces [22][23] and never isolated from the substrate. In such a configuration *h*-BN always constituted an integral part of a 3D system, and could not be considered a truly isolated 2D nanostructure. The work of Novoselov was expanded by Pacile et al who published a paper where using

micromechanical cleavage they were able to obtain few-layer *h*-BN nanosheets and image them with CTEM [10]. All the following attempts to image the structural properties of protruding single layers of *h*-BN used more sophisticated TEM techniques: HRTEM with microscope operated at 300 keV [52], 120 keV [126] and 80 keV [127][128][129], and finally aberration-corrected ADF STEM operated at 60 keV [96].

Several HRTEM studies [128][126][93] focused on exit phase reconstruction, which allowed for the distinction of individual boron (B) and nitrogen (N) atoms based on their relative phase intensities. Although different synthesis methods (reactive ion etching, electron beam thinning, and chemical exfoliation) were used to produce atomically thin *h*-BN nanoflakes, in all cases almost similar results were reported. Findings of the exit-phase reconstructed images have shown a dominant presence of nitrogen terminated zig-zag edges, preferable formation of triangular shaped boron mono-vacancies and multi-vacancies with zig-zag nitrogen terminated edges formed by electron beam, structural distortions around vacancies, and absence of topological defects. The only exception was the chemically exfoliated 2D *h*-BN which was shown to be more resilient to electron beam damage and amorphisation [93]. The stability of nitrogen terminated zig-zag edges can be explained by looking at the values of the knock-on energy threshold for B and N which are 74 keV and 84 keV respectively (perfect monolayer crystal is assumed) [130]. The absence of topological defects, routinely formed in graphene [131], such as vacancy reconstruction and Stone-Wales defects are most likely related to the fact that neither N-N nor B-B bonds are energetically favourable compared to the B-N bond [132].

Aberration-corrected ADF STEM has been exceptionally effective in the study of 2D *h*-BN nanosheets [96]. Not only it was able to resolve individual atoms but also allowed identification of all atomic species with 99% certainty, based on quantitative statistical analysis of atomic intensities. This allowed for the identification of substitutional defects such as two carbon atoms substituting for B-N pair, and oxygen substituting for single N atom. Although the electron beam energy was as low as 60 keV, below the knock-on threshold for both B and N, the substitutional defects were most likely formed through vacancy intermediates, meaning that for non-destructive characterization even lower accelerating voltages must be used.

4.2 Structural Models

Most of the work in literature was done on the samples prepared by micromechanical cleavage [9][10][126][127][128]. For this project all samples were prepared by liquid-phase exfoliation and mainly produce few-layer nanoflakes with protruding monolayer regions [30]. This gives an opportunity to examine stacking in details as well as confirm previous structural findings.

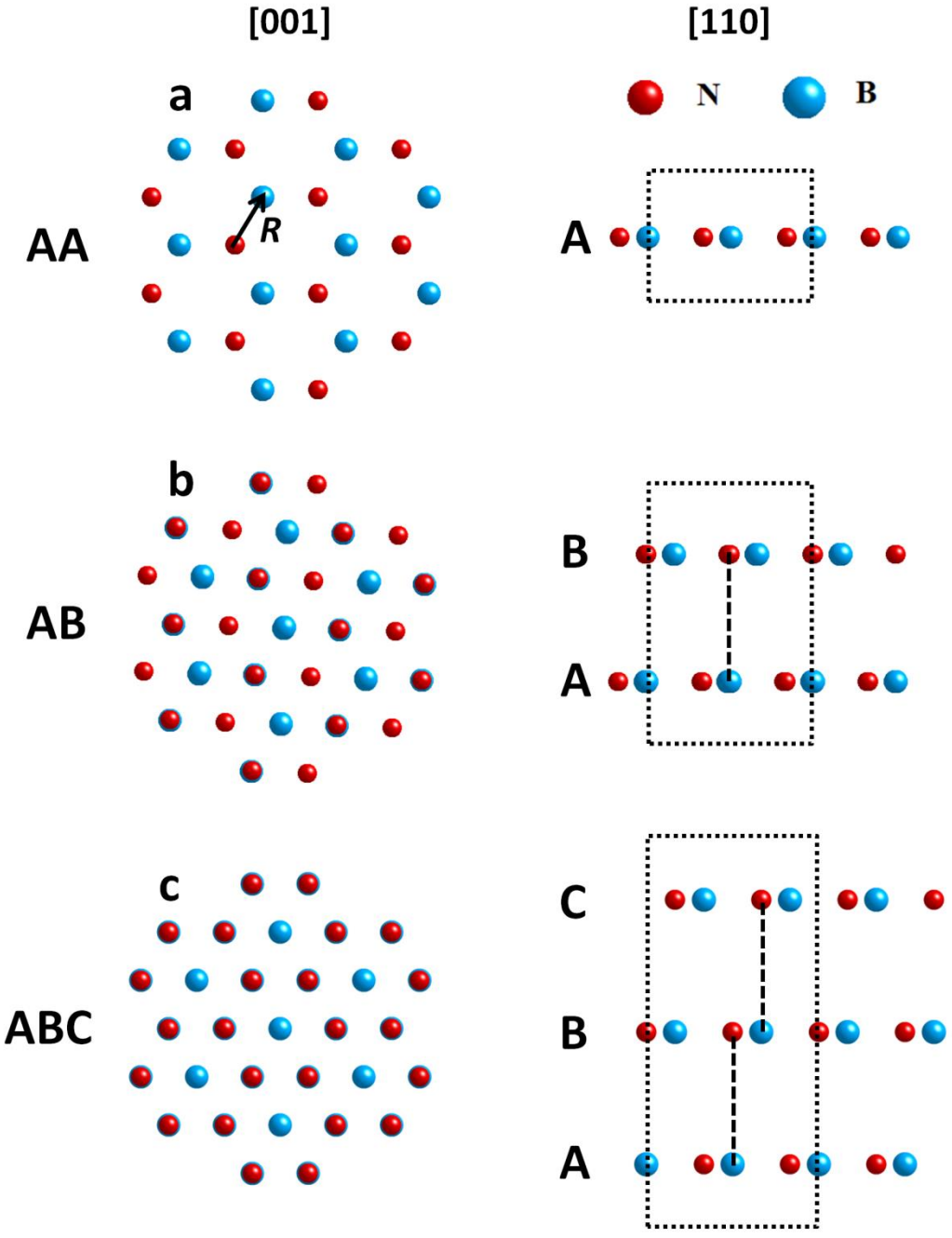


Figure 4.2. *h*-BN structural models View along [001] shows the projected structures expected in the atomically resolved images. View along [110] unambiguously shows stacking sequences. The interlayer distance of [110] view is shown to scale with respect to the interatomic distances of the [001] view. Dashed lines are used to indicate that in (b) and (c) N stacked above B.

The examination of the structure and stacking of *h*-BN nanosheets readily leads to a series of possible high-symmetry non-bulk configurations based on deviations of "simple" and "Bernal" stacking [117][133][134] (Fig. 4.2). These include: AA where the monolayer structure repeats itself (Fig. 2a); AB formed by shifting second layer along the vector $\boldsymbol{R}$ (Fig. 4.2b); and ABC formed by shifting second layer along the vector $\boldsymbol{R}$ and third layer along the vector $2\boldsymbol{R}$ (Fig. 4.2c). Of course, if we start with the AA' stacking (Fig. 4.1) and shift the layers exactly as before, similar structures will be obtained. However, in this scenario B and N atoms will be stacked on the top of each other, which is considered to be less stable than the case presented in Figs. 4.2b, 4.2c. Theoretical calculations indicate similar cohesive energies for all these models [117][133][134] where the AA type is calculated as being the least energetically favourable [134]. Moreover, AB stacking was predicted to be the most stable for *h*-BN bilayers [133].

4.3 Conventional TEM and Diffraction

The main structural parameters, which can be determined with conventional TEM machine, are shape, size and relative thickness of the particles. Although the available information appears somewhat limited, yet it is the important characterisation step which provides initial insight about the sample. Furthermore, it allows optimisation of the sample preparation technique and ensures sufficient quality of the deposited grid necessary for high-resolution microscopy.

Selected area electron diffraction is complimentary to any TEM instrument and provides information about the crystal symmetry and lattice spacings. In addition, for zone-axis oriented nanoflakes with particular structures, it is possible to differentiate between monolayer and multi-layer regions and determine the stacking sequence of the material based on the intensity ratio of the diffracted spots [135].

The first step was to calculate diffraction spots intensity ratios for monolayer and multilayer nanoflakes using the simple structure factors approach (Section 2.2.3). Calculations were performed for bulk stacking and other high symmetry structural models such as AA, AB and ABC to see whether unique intensity ratios could be obtained. The lowest order reflections, $(10\bar{1}0)$ and $(11\bar{2}0)$, were chosen because are least affected by the curvature of the Ewald's sphere. The results of these calculations are given in Table 4.1 and the following conclusions can be drawn accordingly:

- The ratio of the diffraction spots cannot be used to distinguish monolayers from multi-layers in AA' *h*-BN. This is because the scattering strength of the B atom is about equivalent to N atom.
- AB and ABC are readily distinguishable from the AA'. Thus, experimentally, it should be possible to distinguish deviations from the naturally occurring stacking.
- If a mixture of stacking sequences exists in the nanocrystal, the presence of AB and/or ABC stacking will have the effect to decrease the $I_{\{10\bar{1}0\}}/I_{\{11\bar{2}0\}}$ ratio relative to the value for AA' stacking, while the presence of AA' and AA will increases it.

Table 4.1. Calculated ratios of intensities, $\boldsymbol{I_{\{10\bar{1}0\}}/I_{\{11\bar{2}0\}}}$, for the different stacking sequences. Corresponding stacking sequences are given in the Figs. 4.1, 4.2. Ratios were calculated using atomic scattering amplitudes for neutral atoms. The electron beam direction is perpendicular to the *h*-BN basal plane. Example of the calculation is given in the Appendix A.

	Ratio ($I_{\{10\bar{1}0\}}/I_{\{11\bar{2}0\}}$)					
No. of layers:	1	2	3	5	11	Bulk
AA'	1.1	1.1	1.1	1.1	1.1	1.1
AA	1.1	1.1	1.1	1.1	1.1	1.1
AB	1.1	0.28	0.37	0.31	0.28	0.28
ABC	1.1	0.28	0	0.04	0.01	0

Fig. 4.3 shows two low-resolution CTEM images of 2D *h*-BN with corresponding SAED and intensity profiles. As expected, SAED confirms that we have a crystalline material with hexagonal symmetry. In Figs. 2c and 2d $I_{\{10\bar{1}0\}}/I_{\{11\bar{2}0\}}$ ratios are 9.3±2.5 and 0.29±0.09, correspondingly. While the first ratio does not agree with any of the calculated values, the second matches with the AB structure. The intensity profiles (Figs. 4.3e, 4.3f) indicate a slight off-axis tilt which, in combination with fractional translational shifts and Debye-Waller factor, may be the reason for the discrepancy between the theoretical prediction and the experimental values. In the given example a reliable and quantitative determination of the stacking sequence proved to be impossible, however, it confirmed that stacking variations can exist in 2D *h*-BN. The main challenge for the acquisition of the quantifiable SAED pattern is to align the crystal perfectly on-axis. In practice, this proved to be extremely challenging.

It can be speculated that the difference between theoretical value, 1.1, and experimentally observed, 9.3±2.5, is caused purely by the Debye-Waller factor. The

magnitude of the Debye-Waller factor necessary to produce such difference was calculated using the following equation:

$$\left(\frac{I_{\{10\bar{1}0\}}}{I_{\{11\bar{2}0\}}}\right)_{theoretical} \times e^{-\frac{B}{4}\left(g^2_{\{10\bar{1}0\}}-g^2_{\{11\bar{2}0\}}\right)} = \left(\frac{I_{\{10\bar{1}0\}}}{I_{\{11\bar{2}0\}}}\right)_{experimental} \qquad \text{Eq. 4.1}$$

Solving Eq. 4.1 for B-factor, the obtained value is $B = 19.9\ \text{Å}^2 \pm 5.3\ \text{Å}^2$. For elemental crystals B-factors of such magnitude are only reported for alkali metals [136]. Much more plausible B-factor would be of magnitude $1.5\ \text{Å}^2$. For $B = 1.5\ \text{Å}^2$, the term $e^{-\frac{B}{4}\left(g^2_{\{10\bar{1}0\}}-g^2_{\{11\bar{2}0\}}\right)} = 1.2$ and theoretical ratio is only increased from 1.1 to 1.3. Hence, it can be concluded that for 2D *h*-BN and Debye-Waller factor cannot be solely responsible for the observed experimental ratio.

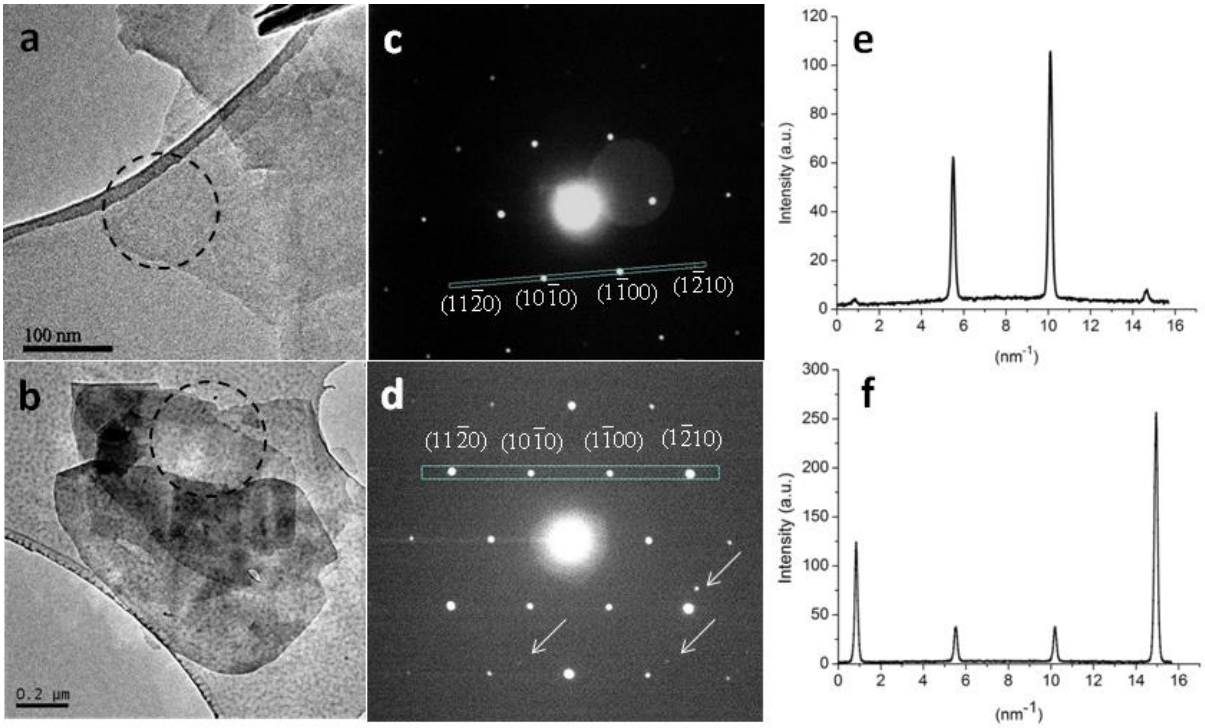


Figure 4.3. (a), (b) Low magnification CTEM images of *h*-BN nanoflakes with corresponding (c) and (d) SAED patterns and (e) and (f) measured intensity profiles as marked. Dotted circles in (a) and (b) indicate selected areas for diffraction. Additional spots marked with arrows in (e) are likely to correspond to the presence of in-plane rotated layers.

The analysis of SAED patterns on partially restacked nanoflakes was also carried out. For this purpose a larger amount of dispersed material was deposited onto the grid in order to induce re-stacking and full coverage of the TEM grid. An example of a typical image with corresponding SAED is given in Fig. 4.4. Thirty diffraction patterns were

recorded and the averaged ratio of the $\{10\bar{1}0\}$ and $\{11\bar{2}0\}$ diffraction ring intensities was calculated. The obtained averaged value was 1.18 ± 0.04, which is remarkably close to the expected AA' ratio. This implied that majority of the as-exfoliated flakes and the restacked nanofilms have an AA' structure.

Theoretical calculations predicted that while Van der Waals forces determine the interlayer distance, electrostatic forces dictate the optimal stacking sequence [137]. This suggests that modifications of stacking arrangements may occur through intercalation of ionic species between the layers and at the edges. In fact, theoretical calculations on *h*-BN intercalated with neutral potassium atoms have suggested the induction of an AA stacking between the *h*-BN layers [138]. In sight of this, the study of the partially restacked *h*-BN nanofilms was further extended to investigate the influence of contaminants and intercalated ionic species on the stacking sequence. In this experiment Na^+ species (in the form of NaCl) were deliberately added to the exfoliated nanosheets in solution before deposition. The obtained $I_{\{10\bar{1}0\}}/I_{\{11\bar{2}0\}}$ value, averaged again across 30 SAEDs, is 0.89 ± 0.02. This value is significantly lower than the one for pristine nanoflakes indicating the presence of stacking similar to AB and/or ABC structures (Table 4.1).

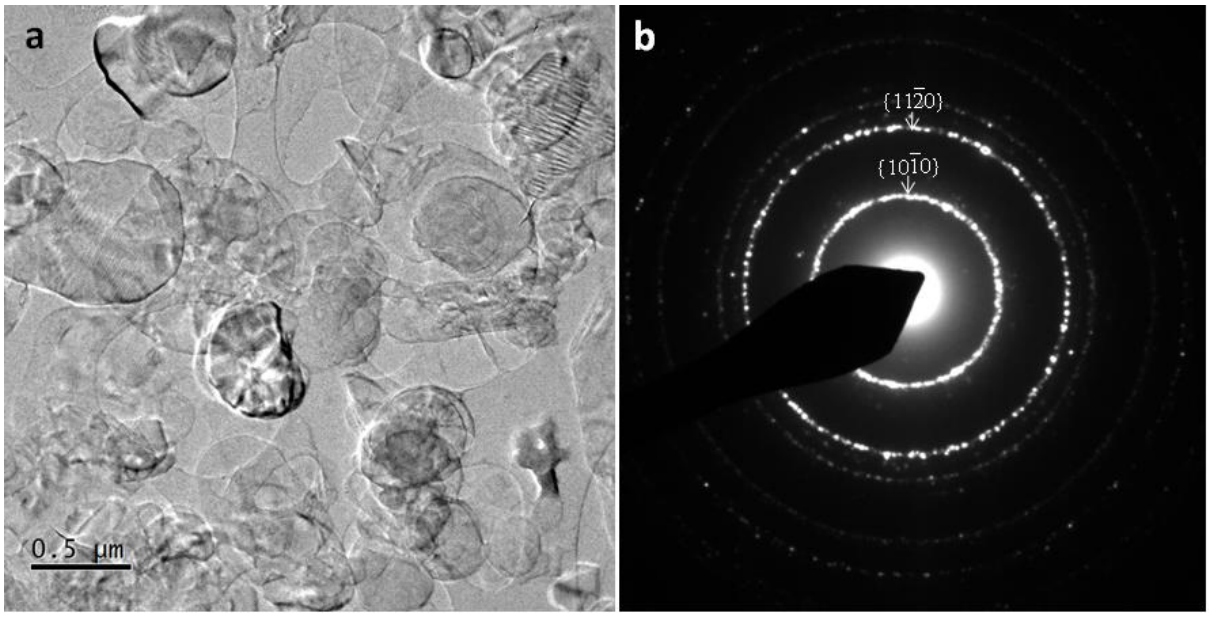


Figure 4.4. (a) Low-resolution CTEM image of the restacked *h*-BN with (b) corresponding SAED.

4.4 Aberration-corrected TEM

The reliable interpretation of HRTEM images requires careful image simulations of the phase-contrast mechanism . Figs. 4.5a, 4.5b, 4.5g, and 4.5h show stepped structures for different structural models with corresponding simulations (Figs. 4.5c, 4.5d, 4.5i and 4.5k) and intensity profiles (Figs. 4.5e and 4.5f). The following conditions were used: 80 keV, $C_s = 3\mu$m, $\Delta f_{Sch} = -4.3\ n$m . All other aberrations were set to zero. The simulated images indicate several points:

- AA' and AA are readily distinguished from AB and ABC on the basis of contrast observed in the stepped 2D nanoflakes. Such a result is not surprising since the calculated diffraction intensity ratios (Table 4.1) show significant variation and the information contained in the diffracted beams is merely modulated by the CTF of the microscope.
- Counting of the number of layers based solely on the intensity profile analysis is virtually impossible. The variation of intensity in AA' and AA is roughly 3-4% per layer. Such minor difference is difficult to distinguish in experimental images due to background noise.
- Potentially, it is possible to distinguish AA' and AA stacking on the basis of the intensity difference between the nearest neighbour atomic columns. In the AA' structure the intensity profile (Fig. 4.5e) shows slight asymmetry between the nearest neighbour atomic columns for odd number of layers and no asymmetry for even number of layers. Intuitively a similar difference can be observed in the trilayer region. For the AA structure the intensity profile (Fig. 4.5f) shows that the asymmetry between the nearest neighbour atomic columns increases with the number of layers.

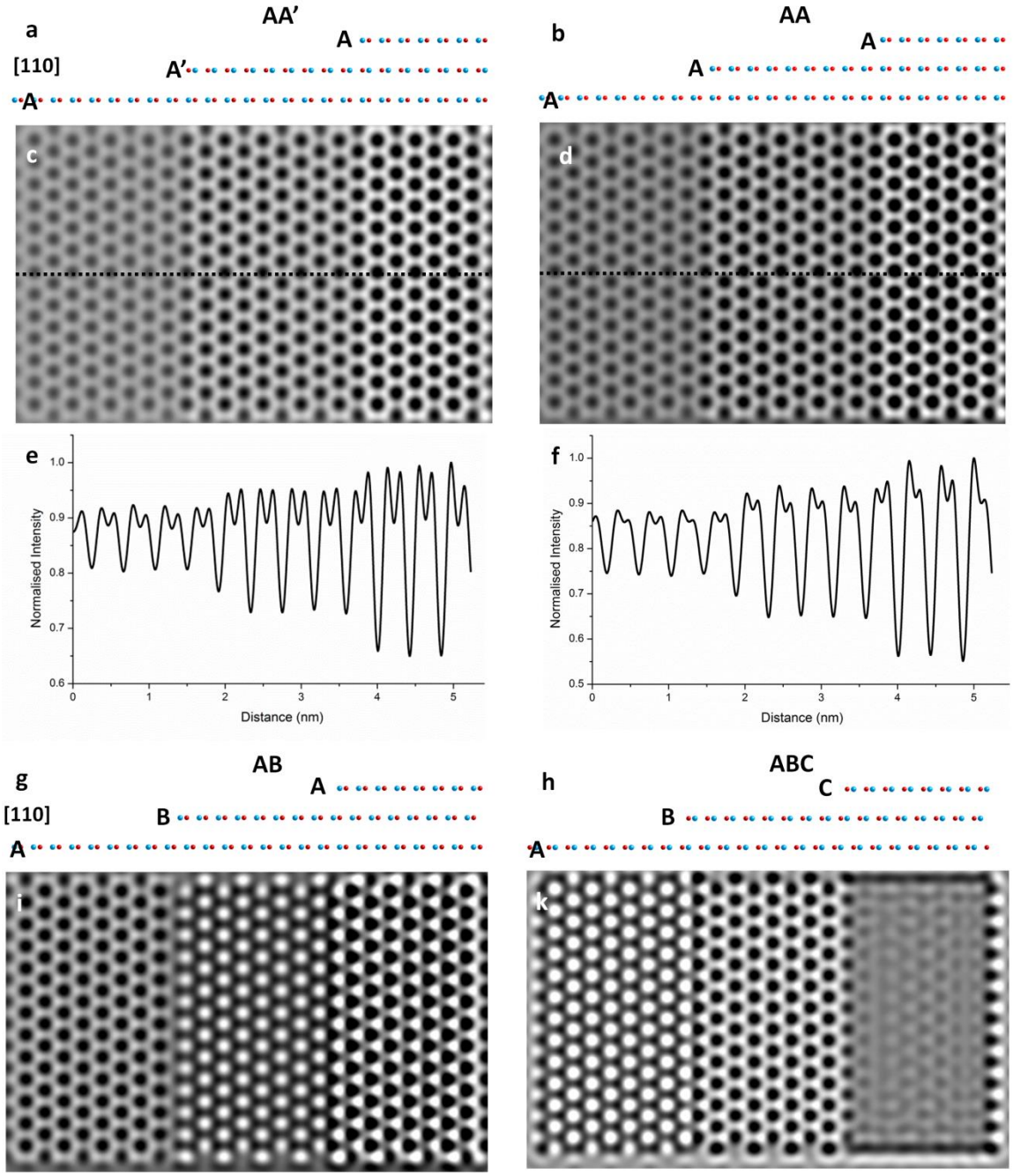


Figure 4.5. (a), (b) Schematics of the *h*-BN stepped structures (AA' and AA stacking) with corresponding (c) (d) simulated HRTEM images and (e) (f) intensity profiles. (g), (h) Schematics of the *h*-BN stepped structures (AB and ABC stacking) with corresponding (i), (k) simulated HRTEM images. $\boldsymbol{C_s = 3\ \mu m}$ and defocus is $\boldsymbol{\Delta f_{Sch} = -4.3\ nm}$. All other aberrations are set to zero. QSTEM code was used for the simulations.

Obtaining experimental images at the exact Δf_{Sch} can be rather challenging. Hence, simulations were performed for a range of defocus values going from 2 to 8 nm. All the points mentioned above were practically confirmed by the simulations. Surprisingly the relative intensities of the nearest neighbour atoms change only negligibly within this defocus range (Figs. 4.6a, 4.6b, and 4.6c). Finally, effect of non-round aberrations was investigated. The following values were used: A_1 = 0.5 nm, A_2 =

5nm, B_2 = 3 nm. As expected, first two points were verified. However, non-round aberrations had huge effect on the relative intensities of the nearest neighbour columns. A comparative study for the AA' stacking is given in Fig. 4.6e. Most noticeably, the bilayer region now shows some unexpected intensity asymmetry between the nearest neighbour columns. Moreover, instability of the microscope lenses can further complicate the analisis (Appendix B). On the basis of this study it can be concluded that the interpretation of the relative intensities in HRTEM data is an extremely sensitive matter and can easily lead to erroneous conclusions.

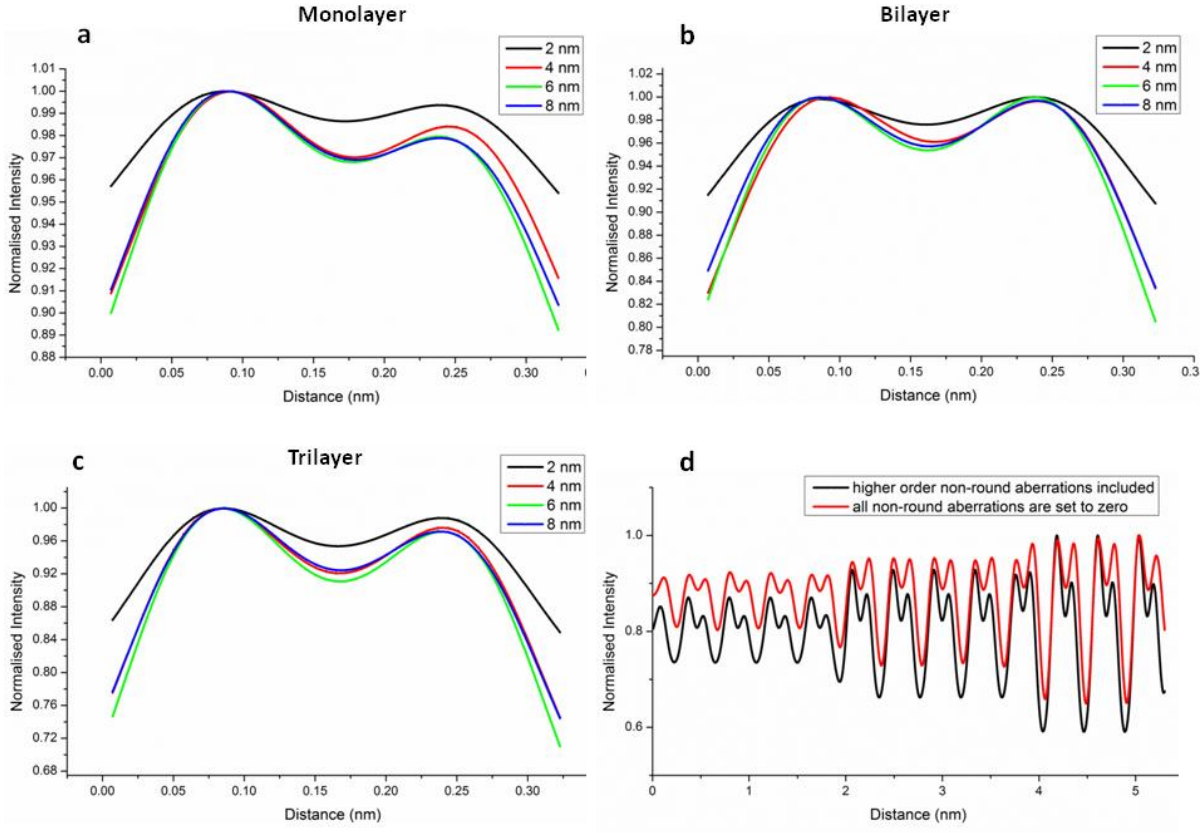


Figure 4.6. (a), (b), (c) Intensity profile of the nearest neighbour columns in the simulated *h*-BN (AA') images for range of defocus values for monolayer, bilayer and trilayer, correspondingly. $\mathbf{C_s = 3\ \mu m}$, while all other aberrations are set to zero. (d) Comparison between intensity profiles of *h*-BN (AA') simulated images using different values for non-round aberrations. Red colour intensity profiles is reproduction of the Fig. 4e. Black colour intensity profile corresponds to the image simulated using the following aberration values: $\mathbf{\Delta f = 4.3\ nm}$, $\mathbf{A_1 = 0.5\ nm}$, $\mathbf{A_2 = 50\ nm}$, $\mathbf{B_2 = 30\ nm}$, $\mathbf{C_s = 3\ \mu m}$.

A typical experimental HRTEM image is shown in Fig. 4.7. As expected, the sample is a 2D nanoctrystal with hexagonal structure. The low contrast makes it virtually impossible to count the number of layers or accurately define the edge boundaries. Contrast reversal can be clearly seen if we compare the top (Fig. 4.7b) and the bottom of the image (Fig. 4.7c). This is consistent with our simulated results for AB and/or ABC

stacking. Similar results were reported by Warner et al [129] where contrast reversal was interpreted as the presence of AB stacking. This provides indirect evidence about the existence of non-bulk stacking in *h*-BN. Moreover, it is possible that the stacking is bulk but nanoflake is not precisely perpendicular to the electron beam, and therefore at different foci in different regions.

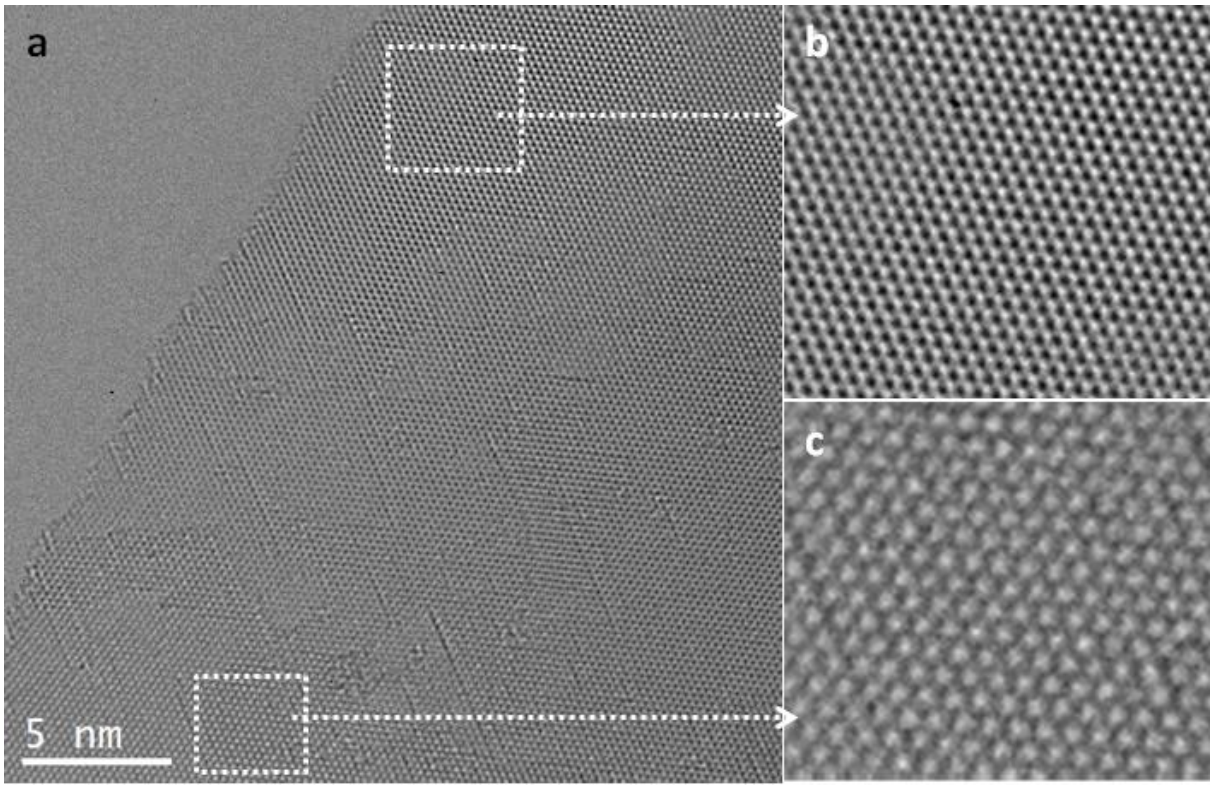


Figure 4.7. (a) Experimental HRTEM image of *h*-BN acquired at 80 keV. (b) and (c) magnified subregions of image (a).

In certain cases, it is only required to determine whether the exfoliated 2D nanostructures are mono- or multi-layers. Large underfocus settings can provide sufficient contrast at the edges. The presence of multiple edges typically suggests a multilayer stepped structure (Fig. 4.8). Converging beam onto the sample has effect of increasing the knock-on damage. Fig. 4.8 shows an image where a very intense electron beam formed typical triangular defects in the *h*-BN lattice. A crystalline lattice can still be seen underneath in the regions where the triangular defects were etched (arrows). This provides a further confirmation that the original area of the nanoflake was not monolayer. If sufficiently a low acceleration voltage is used (below 80 keV) is used, it is actually possible to etch the nanoflakes layer after layer, eventually obtaining a hole on

vacuum. This method can be used to obtain thickness values sufficiently accurate, at the expense of destroying the material.

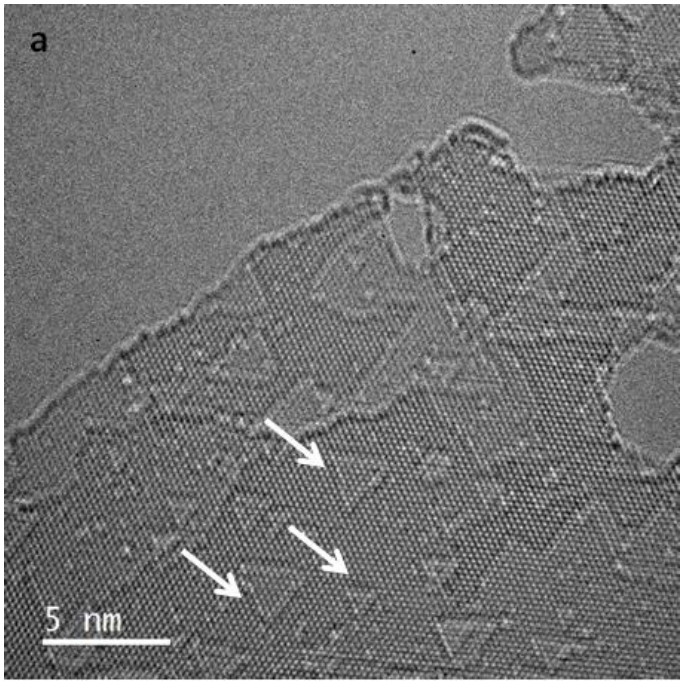


Figure 4.8. (a) Experimental HRTEM image of *h*-BN acquired at 80 keV under strong beam.

4.5 Aberration-corrected STEM

The main conclusion that could be drawn from the HRTEM and diffraction analysis was the possibility of having a non-bulk stacking in *h*-BN nanoflakes. ADF STEM was therefore used to get a more quantitative analysis in view of the incoherent nature of image formation (see Section 2.4.2).

A quantitative assessment of the atomic column intensities was performed in order to determine the stacking sequences present. Fig. 4.9a shows an atomic resolution ADF STEM image of a typical *h*-BN nanosheet. The analysis of the relative intensity profile (Fig. 4.9b) and calculation of a histogram of the column intensities (Fig. 4.9c) allowed an accurate identification of at least two main regions corresponding to a different discreet number of layers. This enabled the calculation of the mean column intensities in the B and N sub-lattices for each of these two regions (Table 4.2). In region 1, the average N atoms' peak intensity is higher than the average B atoms' peak intensity suggesting that this region is indeed a monolayer. We expect no difference in intensity between nearest neighbour sites in a bilayer that follows an AA' stacking sequence. The data presented in Table 4.2 follows this expected trend, confirming that region 2 is a bilayer and that this nanosheet has a bulk stacking. It must be pointed out that in Z-

contrast images for monolayer regions one would expect a much larger intensity difference between the boron and nitrogen sites. The reason for such discrepancy is the contribution of the probe tail as discussed in Section 3.3.3.

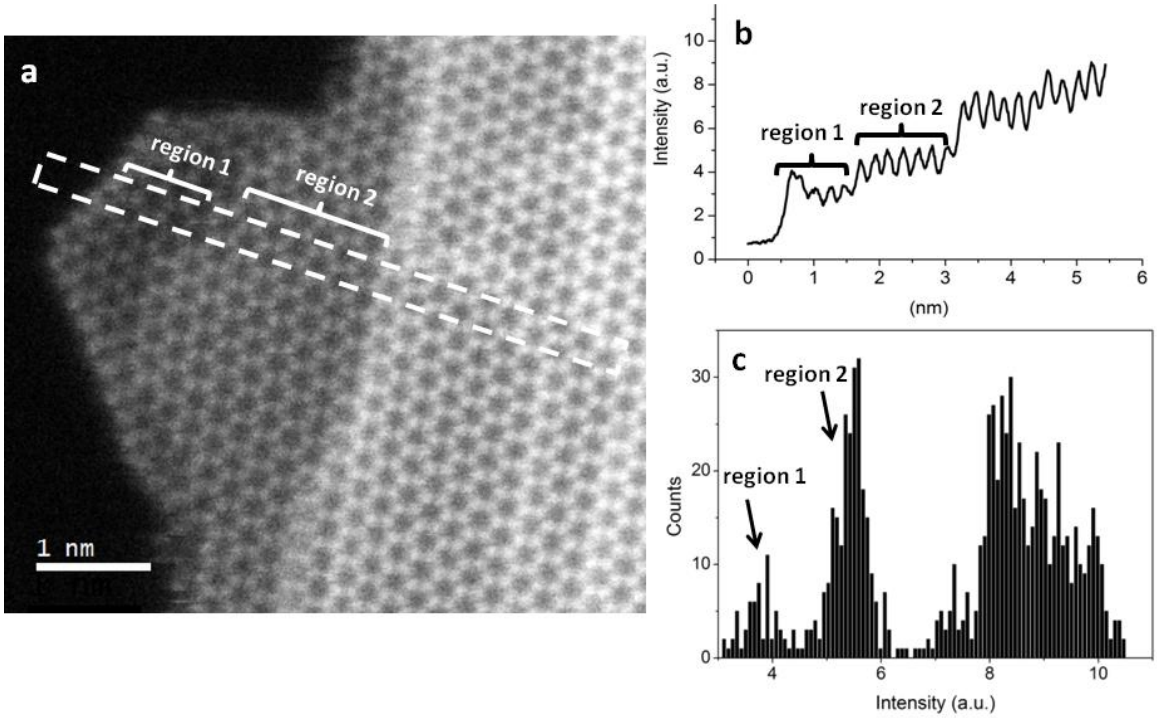


Figure 4.9. ADF STEM image of *h*-BN nanosheet with supplementary graphs used for the stacking analysis. (a) ADF STEM image of *h*-BN sheet acquired at 80 keV. (b) Intensity profile from the marked region. (c) Histogram of the column intensities of the unprocessed image. Integration width in (b) is 0.33 nm. The values in (c) are referenced to the vacuum level.

Table 4.2. Statistical analysis of the nearest neighbour columns (B and N sites) from the two thinnest regions marked in Fig. 4.9a. Sites B and N correspond to the 2 basis defining the structure of the monolayer. For the bilayer B and N sites are consistently defined relative to the monolayer by the translational symmetry. The averaged values for both regions are given. Mean intensity values are referenced to the vacuum level. The image used for this analysis was unprocessed.

	Region 1 (site B)	Region 1 (site N)	Region 2 (site B)	Region 2 (site N)
Mean Intensity	2.75 ±0.04	3.06 ±0.04	4.54 ±0.03	4.50 ±0.03
Mean Layer Intensity	2.90 ± 0.06		4.52 ± 0.04	

Interestingly, the vacuum to region 1 intensity step (2.90 ± 0.06) in Fig. 4.9 is nearly twice as high as that observed for the region 1 to region 2 step (1.62 ± 0.07). One explanation may be the presence of mobile physisorbed impurities at the nanosheet's surface. Although in such case streaking can be expected in the image. More plausible is that region 1 may be a bilayer and region 2 a trilayer. Moreover, region 1 displays unusually bright edge along armchair and partially distorted zig-zag edges. Similar

structural feature was observed by Alem et al. [139] and interpreted as reconstruction of the bilayer zigzag edge leading to a ‘‘closed’’ edge termination. To gain further insight, a time-sequence of images of the same *h*-BN nanosheet (Fig. 4.10) showing atoms diffusing from the edges was examined. Diffusion at the edge of regions 1 and 2 reveals underlying layer consistent with intensity of region 1, confirming that step from region 1 to region 2 is one layer thick. Unfortunately, diffusion at the edge of the vacuum and region 1 does not allow accurate assessment of the thickness. This particular case underlines challenges with accurate layer counting. Nonetheless, the presence of honeycomb pattern in the thicker regions of the nanoflake with equal intensity of the nearest neighbour columns is sufficient to confirm dominance of the bulk stacking.

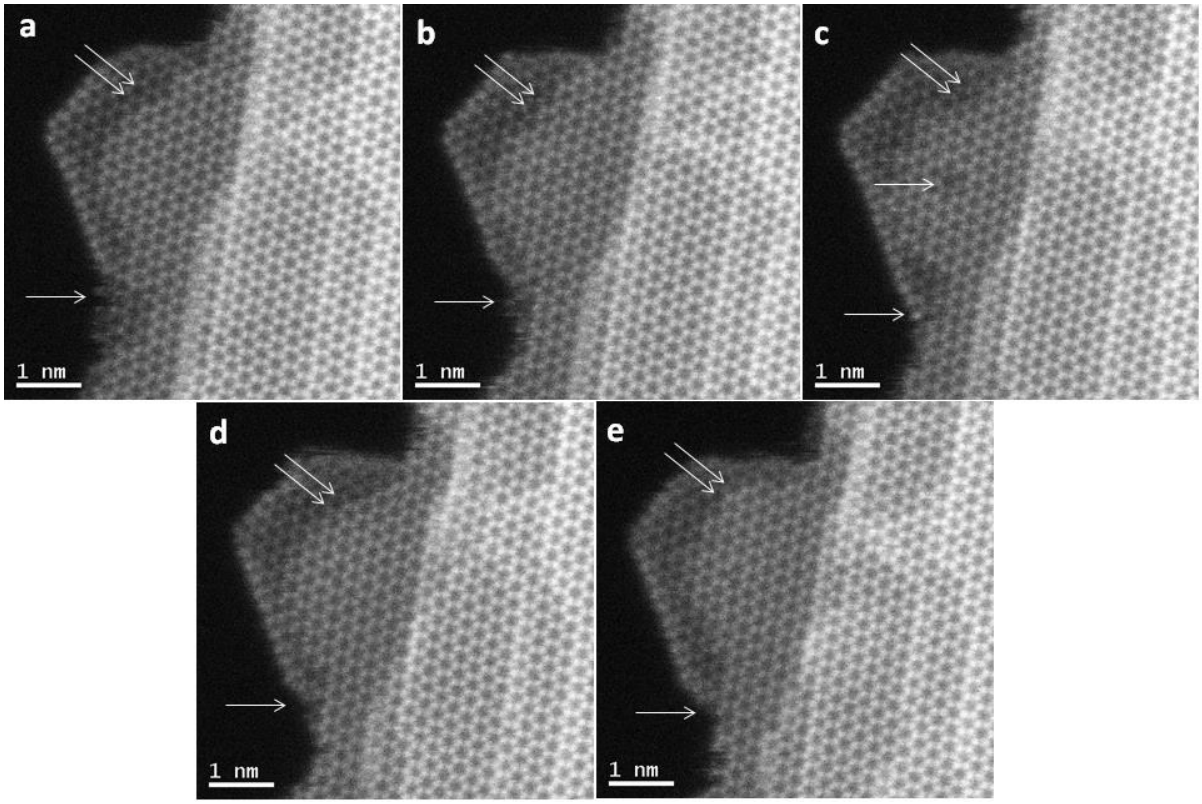


Figure 4.10. ADF STEM image time series of *h*-BN nanoflake. Time acquisition per image is 21 seconds. Single and double arrows are used to mark areas where structural changes are observed. The additional arrow in (c) indicates a vacancy site. Time series show the same region of the 2D nanocrystal as Fig. 4.9.

A small fraction (two out of 20) of the ADF images did not show a honeycomb pattern (Fig. 4.11a). For example, the image in Fig. 4.11a displays several regions where the stacking sequence appears to change throughout. Fig. 4.11b shows a region where an additional atomic column is present in the centre of the honeycomb lattice. Such projection is similar to the patterns formed by AB and ABC structures. Furthermore, in

the region of interest (Fig. 4.11c) each additional layer results in an increase of the intensity difference between the nearest neighbour sites. An accurate analysis of the atomic column intensities shows that the intensity difference between the nearest neighbour sites in this region is approximately equivalent to the product of the number of layers and the intensity difference measured in a monolayer. The averaged intensity difference between nearest neighbour sites for the different number of layers in Fig. 4.11c were 1.02±0.62, 1.85±0.90, 2.88±0.70, and 4.54±0.11 a.u. for the mono-, bi-, tri-, and four-layer regions respectively. This is consistent with a simple AA stacking. However, it should be pointed out that due to the high level of image noise the errors are rather high and a computed statistical histogram of the column intensities did not show discrete peaks. Consequently, our counting of the number of layers in Fig. 4.11c was based upon an assessment of the visual contrast.

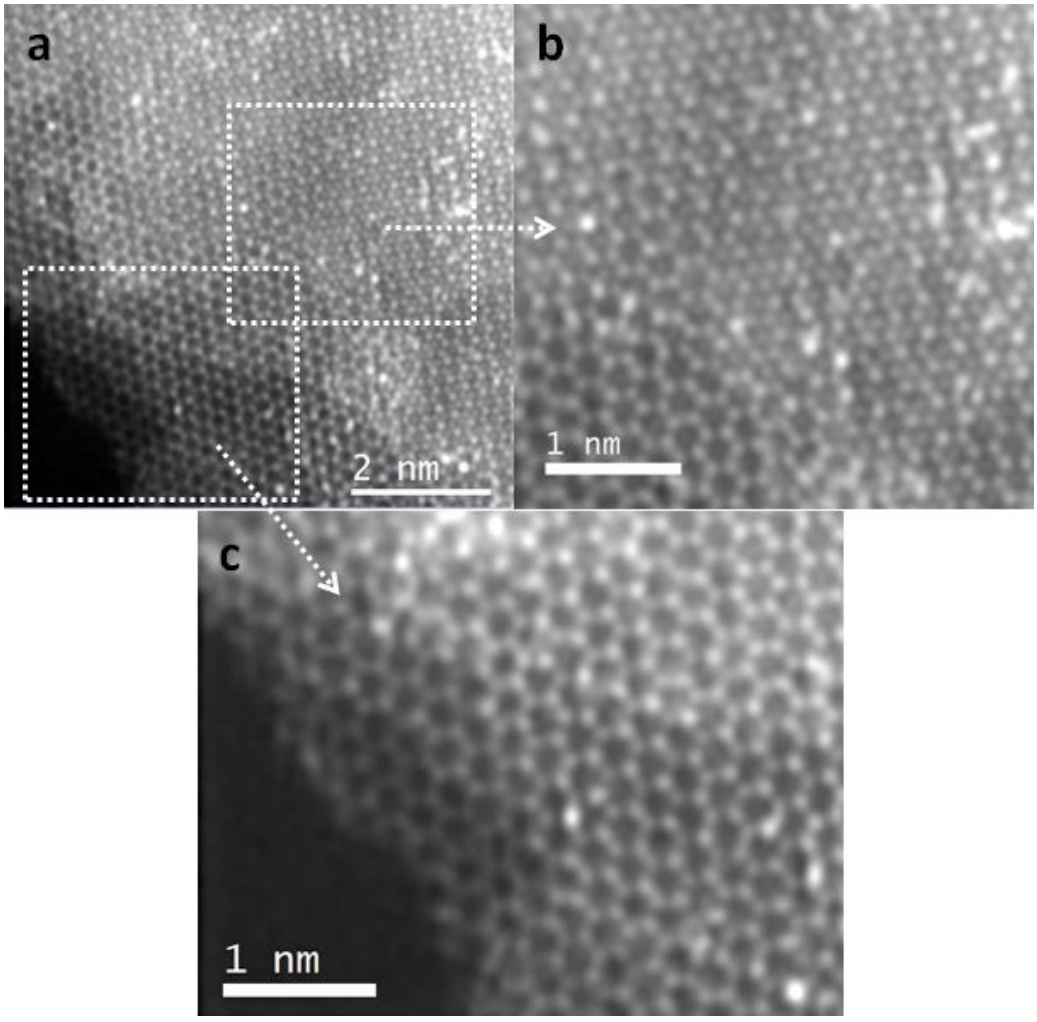


Figure 4.11. (a) ADF STEM image of *h*-BN nanoflake. (b) and (c) Magnified subregions of image (a). Image (a) was processed using Kirivanek's filter.

In order to obtain a better insight into possible stacking arrangements, ADF STEM image simulations were computed (Fig. 4.12) using the structures shown in Figs. 4.5a, 4.5b, 4.5g, 4.5h. The simulated image of the AA' structure agrees nearly perfectly with our experimental results (Fig. 4.9a). There is a clear contrast between nearest neighbour columns in the monolayer region. This contrast disappears for the bilayer. Simulated images of AA, AB, and ABC stacking sequences have one common feature: both the monolayer and the bilayer regions show asymmetry between nearest neighbour columns. This asymmetry is also observed in trilayers for AA and AB sequences; for ABC stacking this asymmetry becomes weaker and additional column becomes visible inside the honeycomb. This is the case where qualitative ADF image simulation predicts unexpected results. For the AB structure the expected projection is a honeycomb pattern with an additional column in the centre, however, the simulation predicts that the columns inside the honeycombs are obscured by the probe tails from the nearest neighbour columns. This means that the region shown in Fig. 4.11b is consistent with an ABC stacking, while region in Fig. 4.11c is consistent with either an AA or an AB stacking. Overall, it can be concluded that nanoflake in Fig. 4.11a displays a mixture of stacking sequences with several regions, where specific non-bulk arrangements (Fig. 4.12) appear to dominate.

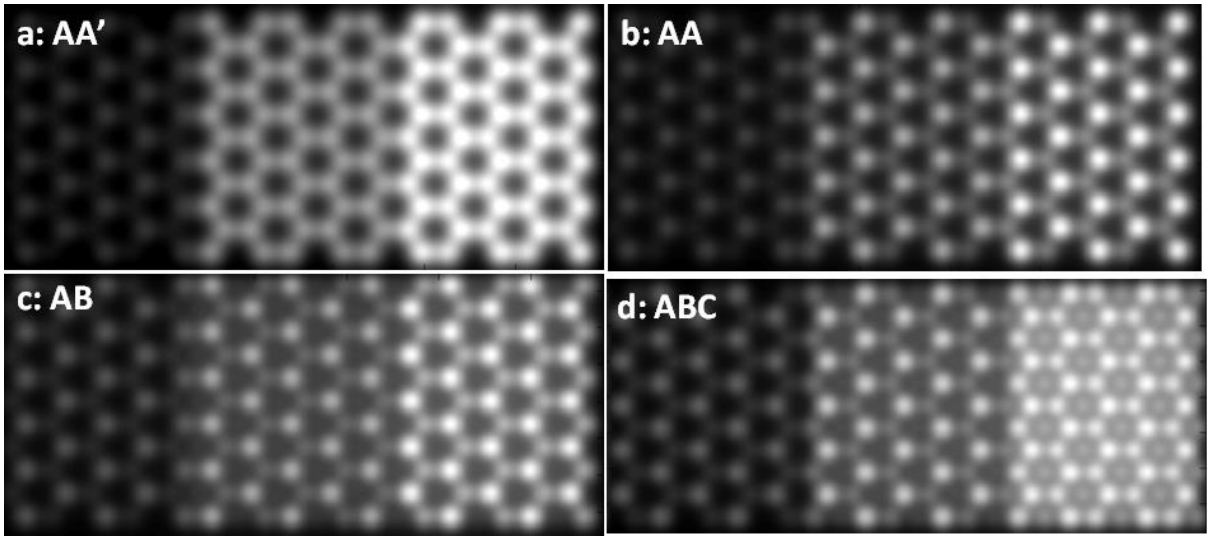


Figure 4.12. ADF STEM simulations of the different *h*-BN structural models calculated using QSTEM code. The structures used for simulations are shown in Figs. 4.5a, 4.5b, 4.5g, 4.5h.

There was additional concern that the observed intensity difference between nearest neighbour sites (Fig. 4.11c) could be caused by higher order non-round aberrations. In order to assess this possibility we investigated whether three-fold astigmatism, A_2, could

indeed generate such an asymmetry in the bilayer *h*-BN in conventional AA' stacking. In these simulations the rotational alignment of the A_2 with respect to the lattice was defined relative to the N-B bond direction (Fig. 4.13a). It must be noted that due to the three-fold symmetry A_2 cannot influence the relative intensity of nearest neighbour sites when at 0º, 60º, 120º, etc. Therefore, it should be sufficient to consider several angle-values of A_2 ranging between 0º and 30º. We decided to run simulations with A_2 at 0º, 11º, 15º and 30º. The reason for choosing the 11º direction shall be discussed later on in this chapter. A_2=50 nm was selected as a typical value for a well-corrected microscope [140].

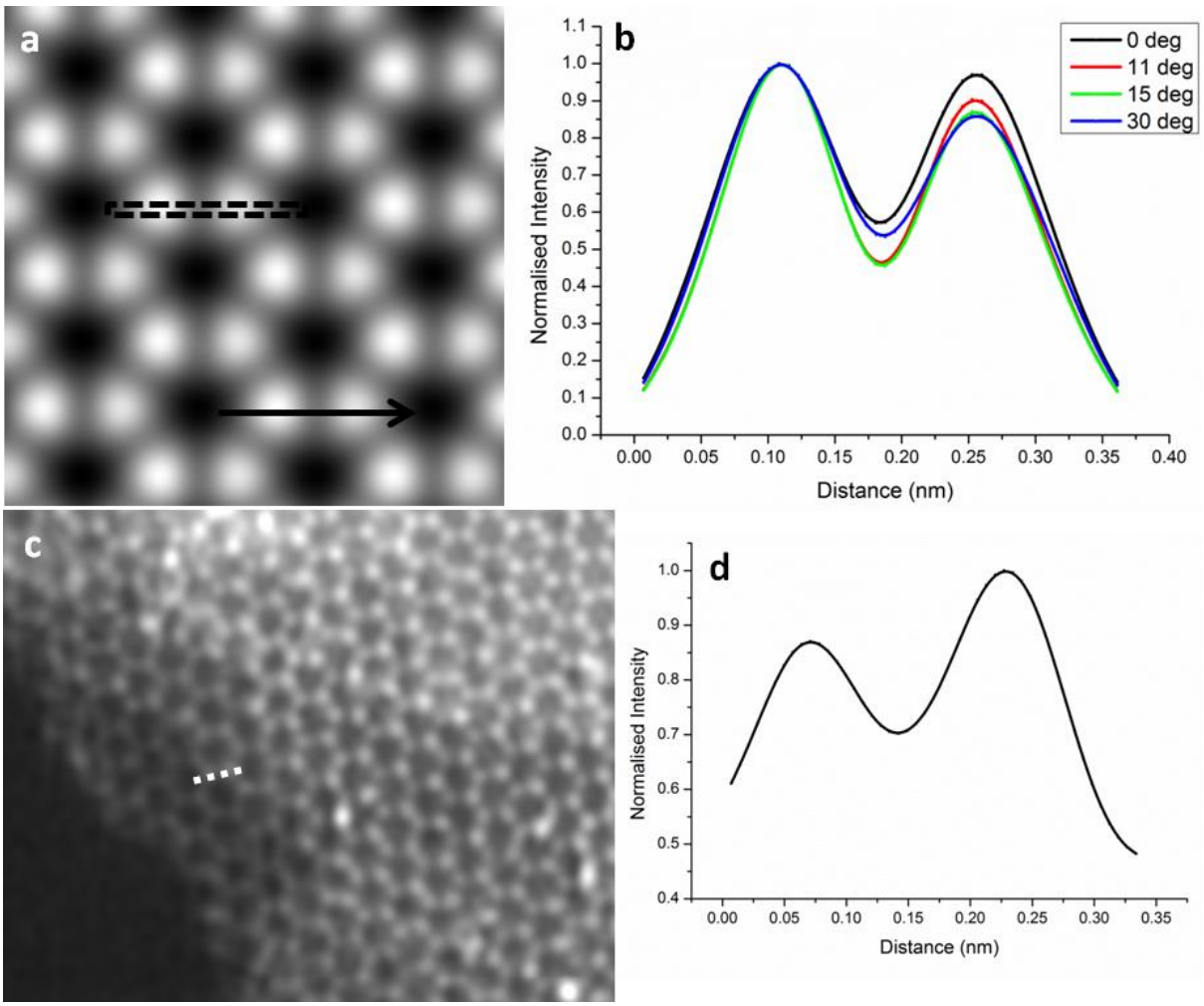


Figure 4.13. (a) Simulated image of the *h*-BN bilayer. (b) Intensity profiles across nearest neighbour columns (as indicated in part (a)) for the simulated images with A_2 = 50 nm for the different orientations. (c) Reproduction of Fig. 11(c). (d) Intensity profile corresponding to the dotted line in part (c). The arrow in part (a) indicates direction relative to which A_2 is aligned. Simulations were carried out using E. J. Kirkland code [141][140][140][139][138][137].

One of the simulated images is shown in Fig. 4.13a. Visually it is difficult to assess the asymmetry of the nearest neighbour site, therefore the corresponding intensity profiles

(dot-marked in Fig. 4.13a) are shown in Fig. 4.13b. A_2 at 11º, 15º, and 30º produce a noticeable difference in intensities, while 0º has no effect, as expected. It is therefore possible that the asymmetries evidenced in Fig. 4.11c are indeed related to the presence of residual A_2. The magnitude of the effect is approximately the same as the one displayed in experimental image (Fig. 4.13c). However, if A_2 was responsible for these asymmetries, it must have generated similar effect on other images acquired during the same microscope session. Interestingly, the bilayer and thicker regions of Fig. 9a (reproduced in Fig. 4.14a) did not exhibit such effect. This meant that A_2 is either negligible or is aligned along 0º, 60º, 120º directions. To disprove the latter point we will use a proof by contradiction. Let's assume that A_2 (> 50 nm) is considerably high and aligned along the 0 degrees direction. In this case, other images acquired during the same microscope session and rotated between 11 and 30 degrees must demonstrate asymmetry between nearest neighbour columns for the bilayers and the thicker regions. Fig. 4.14c shows a nanoflake which does not exhibit any difference in intensities between nearest neighbour sites and is rotated at 11º relatively to the original object (Fig. 4.14a). The angle between the two lattices was estimated from the FFTs in Figs. 4.14b and 4.14d. This case proves that A_2 is indeed negligible and makes us conclude that experimental asymmetries are truly due to non-bulk stacking sequences.

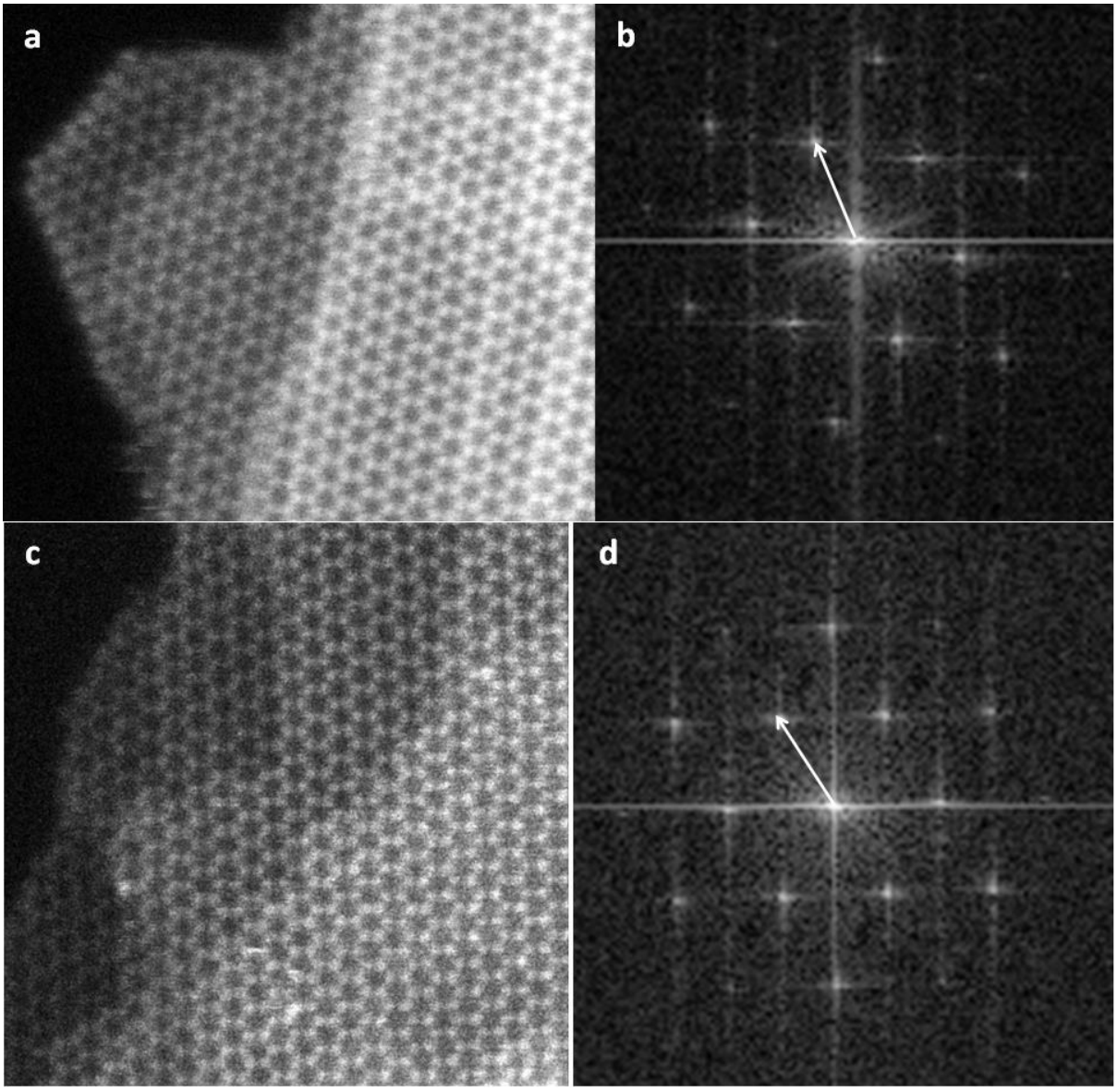


Figure 4.14. (a) Reproduction of Fig. 9a with (b) corresponding FFT. (c) ADF STEM image of *h*-BN nanoflake with (d) corresponding FFT. The arrows are drawn for easy visualisation of the lattice orientation. Images in (a) and (c) are not filtered.

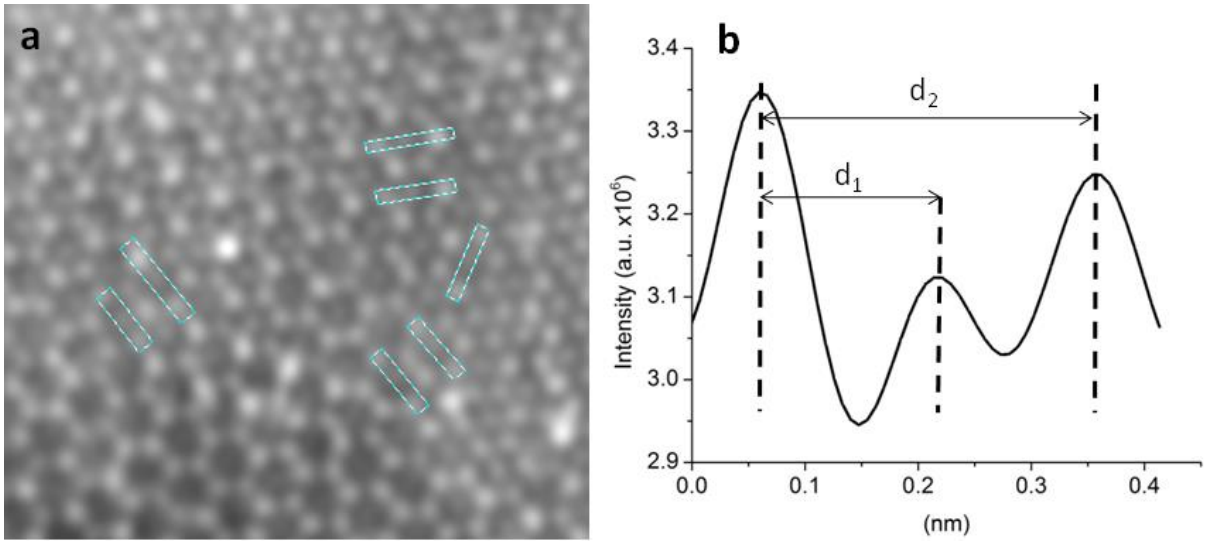


Figure 4.15. (a) Sub-region taken from the image in Fig. 4.11a with indications of the positions for shear strain measurements. (b) Example of the intensity profile from the part a.

One more important point we noticed experimentally was that some of the atomic columns in Fig. 4.11b appeared displaced from their normal lattice positions. The displacement was measured for several spots as indicated in Fig. 4.15a. Parameters, d_1 and d_2, (marked in Fig. 4.15b) were used to calculate the simple shear strain values according to the following equation:

$$\text{simple shear strain} = \frac{|0.5\mathrm{d}_2 - \mathrm{d}_1|}{d_{inter}} \qquad \text{Eq. 4.2}$$

where $d_{inter} = 0.33$ nm is interlayer distance in the *h*-BN (AA'). The calculated strain values are given in Table 4.3. These values are several times larger than those of crystalline materials with covalent bonding, due to the Van der Waals bonding in the layered materials. For example, shear strain of crystalline silicon at 1GPa of shear stress is 0.015 [142]. Moreover, the shear strain required to form an AB stacking fault from an AA stacked bilayer along the vector $\boldsymbol{R}$ (Fig. 4.2a) is 0.44.

A small tilt can also lead to the apparent displacement. However, in such case oval-shaped columns are expected, yet not observed here. A simplified estimate for the bilayer case (AB) predicts that displacement values given in the Table 4.3 can be produced by the tilt of sample between 3 and 6 degrees.

Table 4.3. Distance values $\mathbf{d_1}$, and $\mathbf{d_2}$ defined in Fig. 4.15b, and calculated strain values. Indications of the positions for shear strain measurement are shown in Fig. 4.15a.

d_1 (nm)	0.12	0.17	0.13	0.13	0.18	0.11	0.12
d_2 (nm)	0.32	0.29	0.30	0.29	0.30	0.28	0.29
simple shear strain	0.120	0.064	0.054	0.043	0.086	0.087	0.075

It was important to notice that a large number of impurity atoms appeared as bright spots in Fig. 4.11a (reproduced as Fig. 4.16). A comparison of the atomic columns intensities at impurity sites, I_{imp}, with equivalent crystallographic sites, I_{equiv}, can give a rough estimate of the atomic number of the impurity atom species.

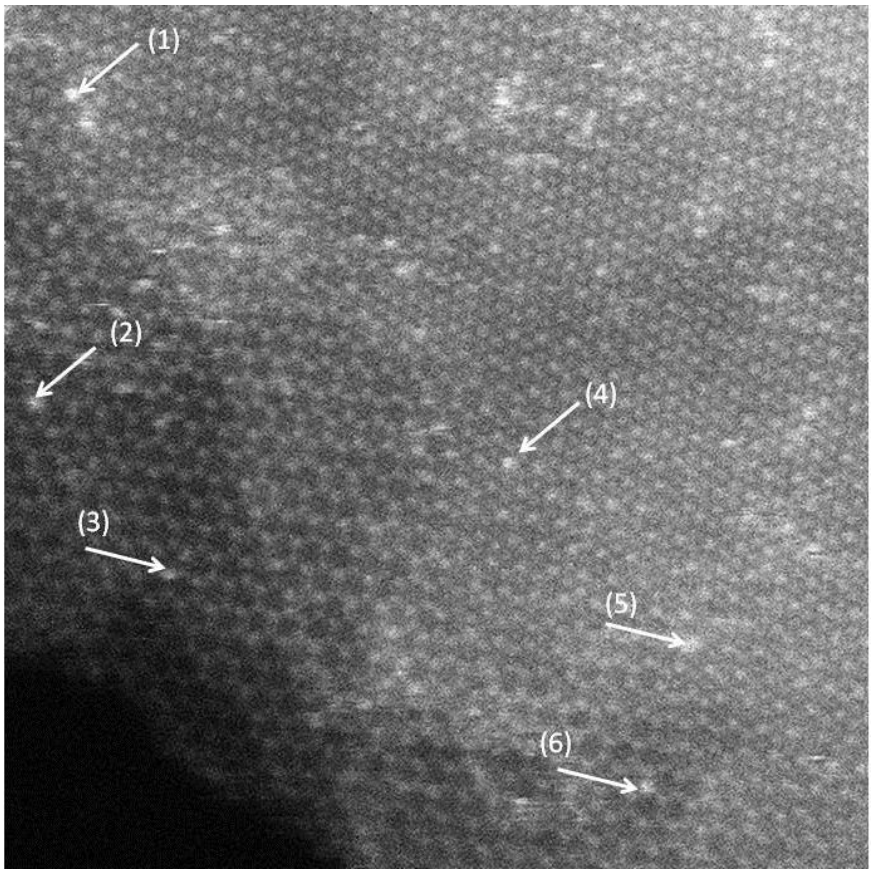


Figure 4.16. Unprocessed version of the image in Fig. 11a. Arrows indicate atomic columns containing impurity atoms.

The atomic number of the impurities, Z_{imp}, was calculated according to the following equation:

$$\frac{I_{\mathrm{diff}}}{I_{\mathrm{equiv}}} = \frac{1}{n_l}\left(\frac{Z_{\mathrm{imp}}}{Z_{\mathrm{BN}}}\right)^{1.7} \qquad \text{Eq. 4.3}$$

where $Z_{\mathrm{BN}} = 6$ is the mean atomic number of the *h*-BN, n_l is number of layer of the column with impurity and I_{diff} is the difference between intensities of the atomic columns with, I_{imp}, and without, I_{equiv}, impurity. Results are presented in Table 4.4. These calculations suggest that the atomic number of these impurities lies in the range of 7-14. It must be pointed out that this is only a rough estimate. Moreover, careful multislice calculations suggest that the atomic number of the impurity cannot be estimated precisely without knowing whether the impurity is substitutional or an ad-atom. Nonetheless, these results are consistent with previous work [96] where Na adatoms (Z = 11) were frequently found in *h*-BN nanosheets similarly exfoliated using NMP as solvent. Commercially available NMP typically in fact contains traces of Na (100 ppb) and other amine impurities at about 12 ppm. Experimentally, non-bulk stacking was only found in nanoflakes contaminated by impurities. It is therefore possible that the relatively high concentration of impurities stabilises the unconventional stacking sequences (which would not be energetically favourable in the pristine state) that we observed experimentally. This theory is indirectly confirmed by the electron diffraction results on the restacked nanofilms intentionally contaminated with NaCl presented earlier on in this chapter.

Table 4.4. Intensity at atomic columns containing impurities ($\boldsymbol{I_{\mathrm{imp}}}$); intensity of equivalent sites not containing impurities ($\boldsymbol{I_{\mathrm{equiv}}}$) and the difference between the two $\boldsymbol{I_{\mathrm{diff}}}$; the number of layers in equivalent sites ($\boldsymbol{n_l}$); and the atomic number corresponding to the impurities ($\boldsymbol{Z_{\mathrm{imp}}}$). The columns with impurities are indicated in Fig. 4.16.

Impurity No.	1	2	3	4	5	6
I_{imp} (a. u.)	1.04	0.6	0.45	0.8	0.85	0.71
I_{equiv} (a. u.)	0.555	0.36	0.28	0.55	0.68	0.44
I_{diff} (a. u.)	0.485	0.24	0.17	0.25	0.17	0.27
n_l	5	3	3	5	5	4
Z_{imp}	14	9	8	10	7	10

4.6 EELS

The final characterisation technique applied for the analysis of the 2D *h*-BN was EELS. It was already shown by Coleman et al [30] that there is an energy shift in the low loss EELS plasmon peaks which can be related to the transition from bulk to the 2D state. Han et al [52] also monitored possible variations in the K-edge of the nanoflakes as a

function of different number of layers without finding and appreciable effect. In our study EELS is used to confirm the chemical composition of the nanoflakes and identify changes in the electronic structure near the edges.

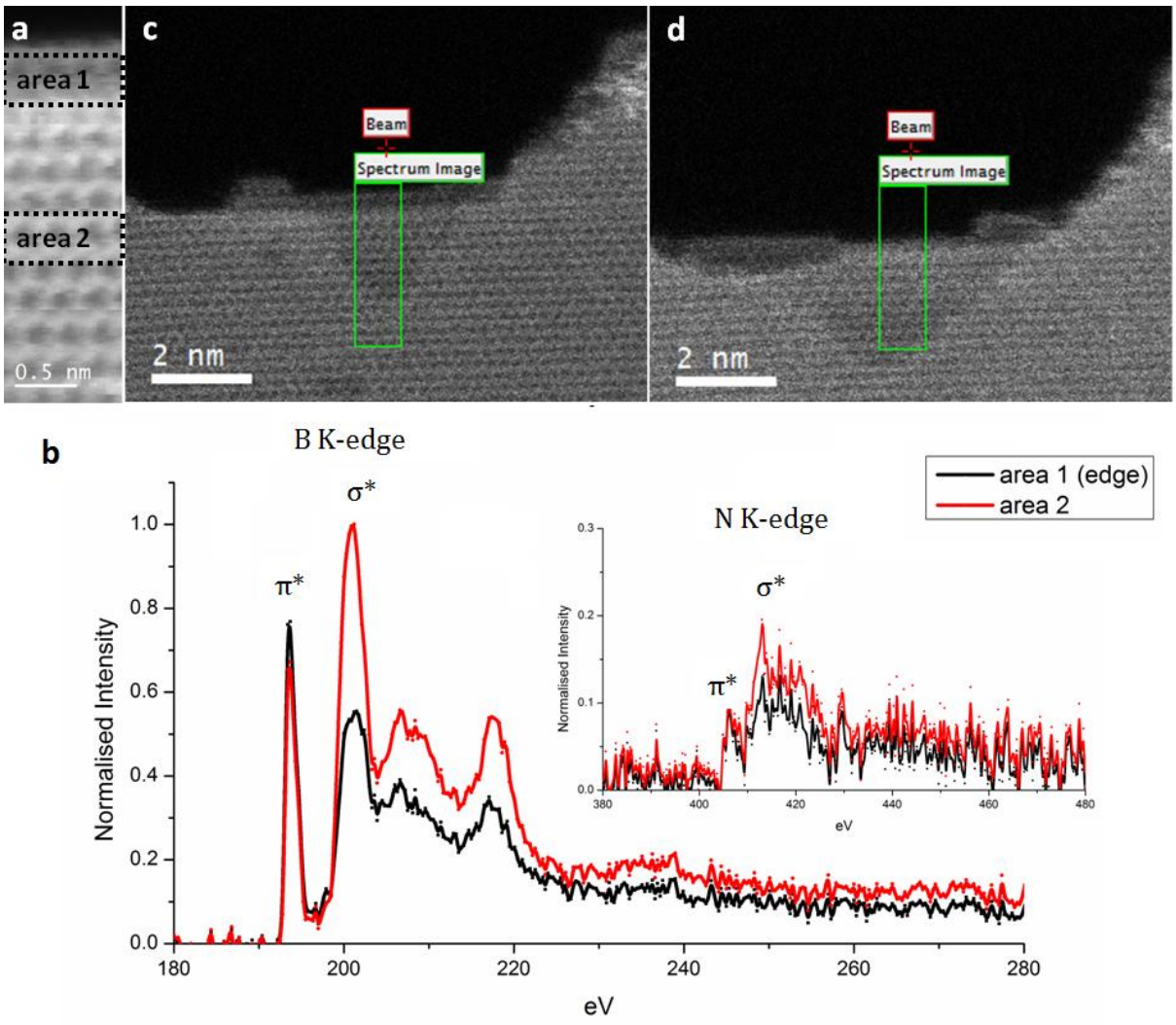


Figure 4.17. (a) ADF image of the *h*-BN with (b) EELS spectra, from the regions indicated in part (a). ADF image of the nanoflake (c) before and (d) after spectrum image acquisition. EELS data was averaged over 70 frames for both area 1 and 2. EELS acquisition details: drift tube voltage (140 V), exposure (0.2 s/frame), convergence semi-angle (37 mrad), collection semi-angle (32 mrad), dispersion (0.3 eV/ch).

Fig. 4.17a shows ADF STEM image of the *h*-BN nanoflake over which the spectrum image was acquired. Fig. 4.17b shows spectra with two distinct absorption features starting at approximately 190 eV and 405 eV; these correspond to the boron and nitrogen K-edges, respectively. Some fine structure, characteristic for sp^2 hybridisation are also readily identifiable. Peaks corresponding to the transitions to the π* and σ* antibonding orbitals are marked appropriately. The spectra shown in Fig 4.17b correspond to two different regions, marked as area 1 and area 2 in Fig. 4.17a. There is clear increase in the peak intensity of the σ* transition for the boron K-edge as we move away from the edge

of the nanoflake. The nitrogen K-edge shows a similar behaviour, although this appears to be less pronounced and somehow obscured by the noise. The changes in the intensity of the σ* transition are indicative of the variations in the electronic structure. In the given case the influence of the edge states extends for approximately 7 Å (approximately 3 unit cells) from the rim of the nanoflake. Additionally, ADF images before (Fig. 4.17c) and after (Fig 4.17d) acquisition of the spectrum image are shown. As expected, strong damage to the edge and the drift of the stage are observed.

4.7 Summary of the findings

The main structural feature investigated in this chapter was the stacking sequence in few-layer *h*-BN. Generally, it can be concluded that the vast majority of *h*-BN nanoflakes and restacked nanofilms exhibit AA' stacking as observed in bulk. Several cases of non-bulk stacking were, however, identified. Initially, SAED and HRTEM provided strong but indirect evidence about these stacking variations. Reliable, conclusive evidence of the non-bulk stacking came from ADF STEM image analysis. ADF STEM showed several nanoflake regions where the dominating stacking sequence was consistent with AA, AB, and ABC. Shear strain was observed for regions with AB and ABC stacking sequences. ADF STEM also revealed the presence of the impurities which seemed to stabilise the non-bulk stacking. The possibility to tune the sequence in restacked nanofilms by simple addition of Na^+ impurity ions was confirmed by electron diffraction analysis.

The electronic properties of liquid-phase exfoliated 2D *h*-BN were also probed by EELS. A change in the electronic properties near the rim of the nanoflake was observed on the basis of σ* peak intensity. This provides a way to assess how far from the rim of the nanoflake the electronic properties are dominated by edge states. For 2D *h*-BN the distance was assessed to be 7 Å.

Chapter 5: 2D Transition Metal Dichalcogenides

In this chapter detailed discussion of the imaging and structural analysis of the liquid exfoliated MoS_2, WS_2 and TiS_2 is given. Based on the conclusions of the 2D *h*-BN analysis, it was understood that HRTEM and SAED has limited potential in the structural analysis of the investigated materials. Hence, characterisation of other materials was primarily based on the ADF STEM.

5.1 2D MoS_2 and WS_2

5.1.1 Introduction

MoS_2 and WS_2 are isostructural with two naturally occurring polytypes 2H and 3R (Fig. 5.1). The coordination of the metal ion is trigonal prismatic. The unit cell lattice parameters are given in the Table 5.1. The stacking of the 2H polytype is very similar to *h*-BN with two S atoms and one Mo atom being stacked alternately on the top of each other.

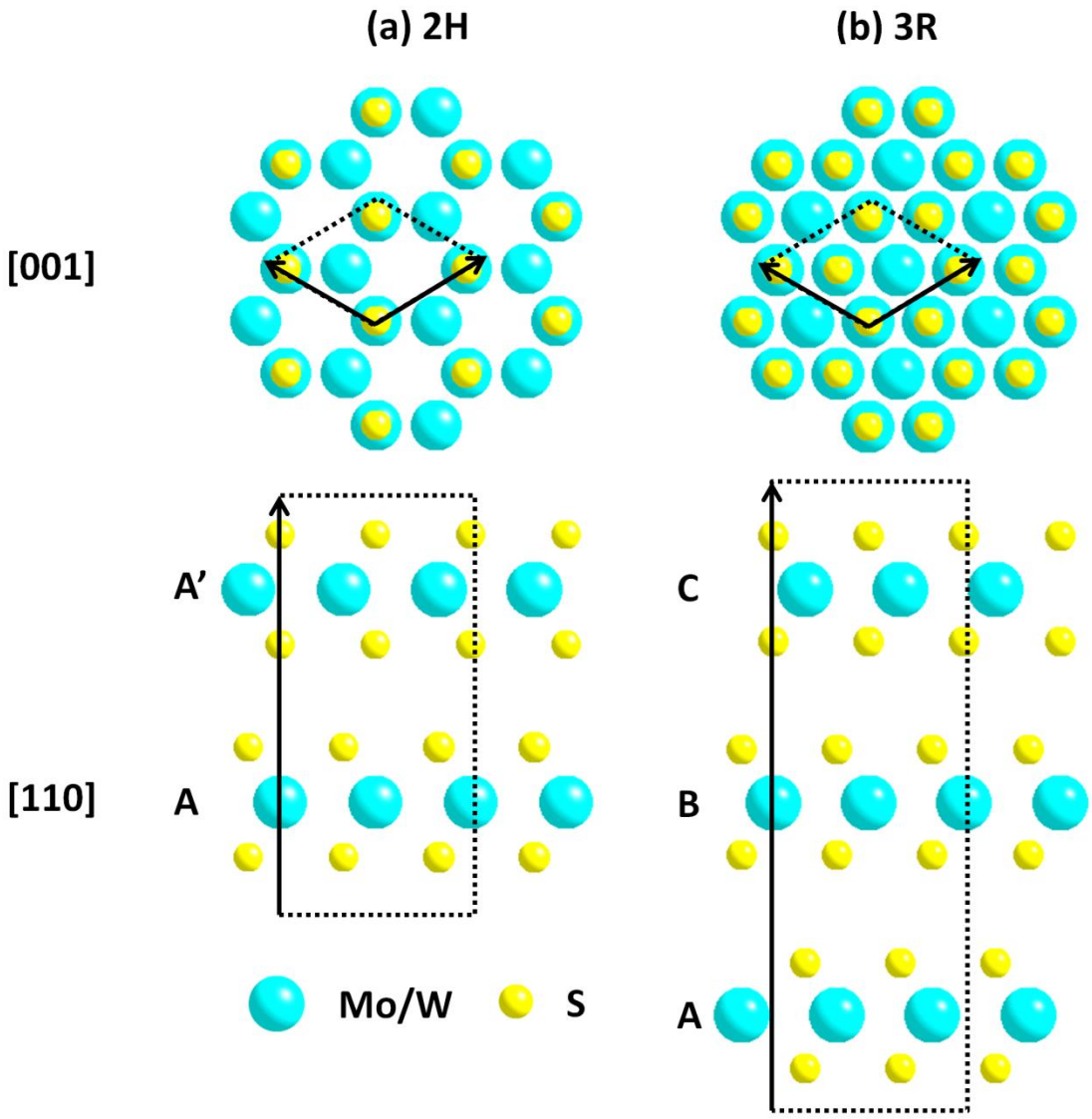


Figure 5.1. Structural models of the bulk Mo/WS_2. View along [001] shows the projected structures recorded in the atomically resolved images. View along [110] unambiguously shows stacking sequences. The interlayer distance of [110] view is shown to scale with respect to the interatomic distances of the [001] view. Dashed lines are used to indicate unit cell.

Table 5.1. Unit cell lattice parameters of the Mo/WS_2 for 2H and 3R polytypes.

	MoS_2	WS_2
2H	$\left\{0.316\ \text{nm}, 0.316\ \text{nm}, 1.230\ \text{nm}, \frac{\pi}{2}, \frac{\pi}{2}, \frac{\pi}{3}\right\}$	$\left\{0.315\ \text{nm}, 0.315\ \text{nm}, 1.230\ \text{nm}, \frac{\pi}{2}, \frac{\pi}{2}, \frac{\pi}{3}\right\}$
3R	$\left\{0.316\ \text{nm}, 0.316\ \text{nm}, 1.837\text{nm}, \frac{\pi}{2}, \frac{\pi}{2}, \frac{\pi}{3}\right\}$	$\left\{0.315\ \text{nm}, 0.315\ \text{nm}, 1.837\ \text{nm}, \frac{\pi}{2}, \frac{\pi}{2}, \frac{\pi}{3}\right\}$

Bulk MoS_2 and WS_2 are n-type diamagnetic [143] semiconductors with 1.2 eV (1.4 eV for WS_2) indirect band gap [34]. In the limit of complete exfoliation both become direct

gap, fluorescent 2D semiconductors [27][28][29]. In MoS_2 for edge-oriented thin films weak magnetism was observed which can be expected from unpaired edge states [144]. This effect was seen to drop off for thicker edges. Similar behaviour can be expected for WS_2.

One of the main industrial applications of bulk MoS_2 and WS_2 are as solid lubricants for mechanical parts [145][146][147] and catalysts in the petro-chemical industry [148][149] for a wide range of organic chemical reactions such as hydrodesulfurization, hydrodenitrogenation, hydrogenation, etc. Exfoliation by intercalation was shown to enhance catalytic properties for certain organic reactions [149]. These materials have also been proposed for applications in electro- photo-catalysis[150][151][40], photovoltaics [152], as a double layer capacitor [153], and as an anode material for Li ion batteries [154][155][156]. Electrical characterization of the few-layer MoS_2 has shown its potential as a thin flexible semiconductor [157]. However, much more promising was the demonstration of the transistor based on single-layer MoS_2 with high mobility (>200 cm^2/Vs and sometimes as high as 780 cm^2/Vs) and high current on/off ratios (>10^8)[42].

The layered nature of these materials allows alkali metals [158], transition metal ions [159], small and large organic molecules [160][161][162][163][164][165][166], and even inorganic complexes [167][168] to be intercalated between its layers, forming inclusion compounds. Intercalation with small atoms like Li can be done directly [158], while for large molecules exfoliation is required [168]. Intercalation allows modulation of its properties, such as conductivity, diffusivity and tribological properties. In particular, improved electrochemical lithiation capacity of the WS_2 nanosheets tested as anode material for batteries is due to the enhanced host capability, enlarged surface area and improved diffusion process upon the intercalation of guest molecules [169][155][170].

MoS_2 was the first layered material attempted to be exfoliated down to single layer [171][172]. In 1963 Frindt and Yoffe were able to obtain MoS_2 crystal nanoflakes with thickness below 10 nm using micromechanical cleavage [171]. Thickness measurements were based on the multiple beam interference. It is quite possible that single and few layers MoS_2 nanostructures were already present. However, multiple beam interference is not sensitive enough to measure thicknesses below 10 nm. Three years later Frindt published another paper [19] showing improvement in the thickness measurements using shadowing and electron microscopy. He was able to obtain electron

micrograph of a stepped structure of MoS_2 flake with the thicker part of the crystal being 7.5 nm and the thinner around 3.8 nm. His work also included the first mentioning about effects of 2D confinement of d-electrons in MoS_2 observed during the measurements of optical spectra [171][172].

Later MoS_2 and WS_2 crystals were again the first layered materials exfoliated using Li intercalation [20][21]. A novel 1T polytype was reported for the nanostructures prepared using this method [173]. The 2H → 1T transformation is accompanied by changes in coordination from trigonal prismatic to octahedral and metal-metal bond distortions[174],[175],[176],[173]. However, one outstanding issue of these studies was the lack of understanding whether these effects were intrinsically due to exfoliation or the presence of intercalated guest molecules trapped in the nanostructures. It was shown that MoS_2 composites prepared via lithium intercalation retained small amounts of lithium in the restacked nanofilms even after washing [164]. This, in turn, undermines the claim that 1T phase is metastable even after removal of Li [174].

Most of the initial techniques employed for the characterisation of nanosheets were X-ray diffraction [20][21][174], Raman [174] [177], X-ray absorption spectroscopy [175],[178] and scanning tunnelling microscopy (STM) [179] [176]. The majority of these studies were focused on the imaging and structural distortions. Several publications include CTEM and HRTEM imaging. They show shape of the nanoflakes under medium magnification [180][175][181], lattice resolution [182][180], and patches of atomic resolution of the basal planes [11]. Only recently due to advances in aberration-corrected microscopy the first structural studies based on atomically resolved ADF STEM images appeared in the literature. They include imaging of the grain boundaries of the CVD grown nanosheets [183], edge structure of the triangular nanocrystals [184] and coherent domains of the 2H and 1T polytypes of the Li-exfoliated nanosheets [59]. However, identification and differentiation between 2H and 1T polytypes is somewhat unsubstantiated. It requires imaging of the sulphur atomic columns which is challenging as will be shown later in this chapter. None of these studies reported the 3R polytype.

5.1.2 Conventional TEM and Diffraction

Similar to the work done in the *h*-BN chapter the first step was to calculate intensity ratios, $I_{\{10\bar{1}0\}}/I_{\{11\bar{2}0\}}$, for 2H and 3R polytypes with different number of layers. The

results of these calculations are given in the Table 5.2. The following conclusions can be drawn accordingly:

- Monolayers are distinguishable from multilayers for 3R polytype but not 2H. This is because the scattering strength of the 2S atoms is about equivalent to 1 Mo atom.
- 2H polytype is readily distinguishable from 3R.

Table 5.2. Calculated ratios of intensities, $\boldsymbol{I_{\{10\bar{1}0\}}/I_{\{11\bar{2}0\}}}$, for the 2H and 3R polytypes. Ratios were calculated using atomic scattering amplitudes for neutral atoms. The electron beam direction is perpendicular to the Mo/WS_2 basal plane.

	Ratio ($I_{\{10\bar{1}0\}}/I_{\{11\bar{2}0\}}$)					
No. of layers:	1	2	3	5	11	bulk
MoS_2 (2H)	0.75	0.74	0.74	0.74	0.74	0.74
MoS_2 (3R)	0.75	0.42	0	0.04	0.01	0
WS_2 (2H)	0.72	0.71	0.71	0.71	0.71	0.71
WS_2 (3R)	0.72	0.36	0	0.04	0.01	0

Relative to 2D *h*-BN, it proved more challenging to produce thin nanoflakes. Figs. 5.2a, 5.2b show typical multi-layered nanoflakes. Unfortunately such nanoflakes do not have uniform areas which are large enough to acquire good quality SAED. $I_{\{10\bar{1}0\}}/I_{\{11\bar{2}0\}}$ of the SAED patterns in Figs. 5.2c. 5.2d are 2.19±0.99 and 2.82±1.04, correspondingly. These values are much larger than calculated and have large error. This large error, most likely cause by the off-axis tilt, makes any further ratio analysis unreliable. Nonetheless, the fact that $I_{\{10\bar{1}0\}}/I_{\{11\bar{2}0\}} > 0$ suggests that neither of the nanoflakes have 3R polytype structure.

Attempts to acquire SAED patterns for partially restacked nanoflakes were also unsuccessful. Nanofilms of Mo/WS_2 require accurate thickness control for SAED characterisation because Mo and W are strong elastic scatterers. All deposited sample were either too thick or with poor coverage of the TEM grid.

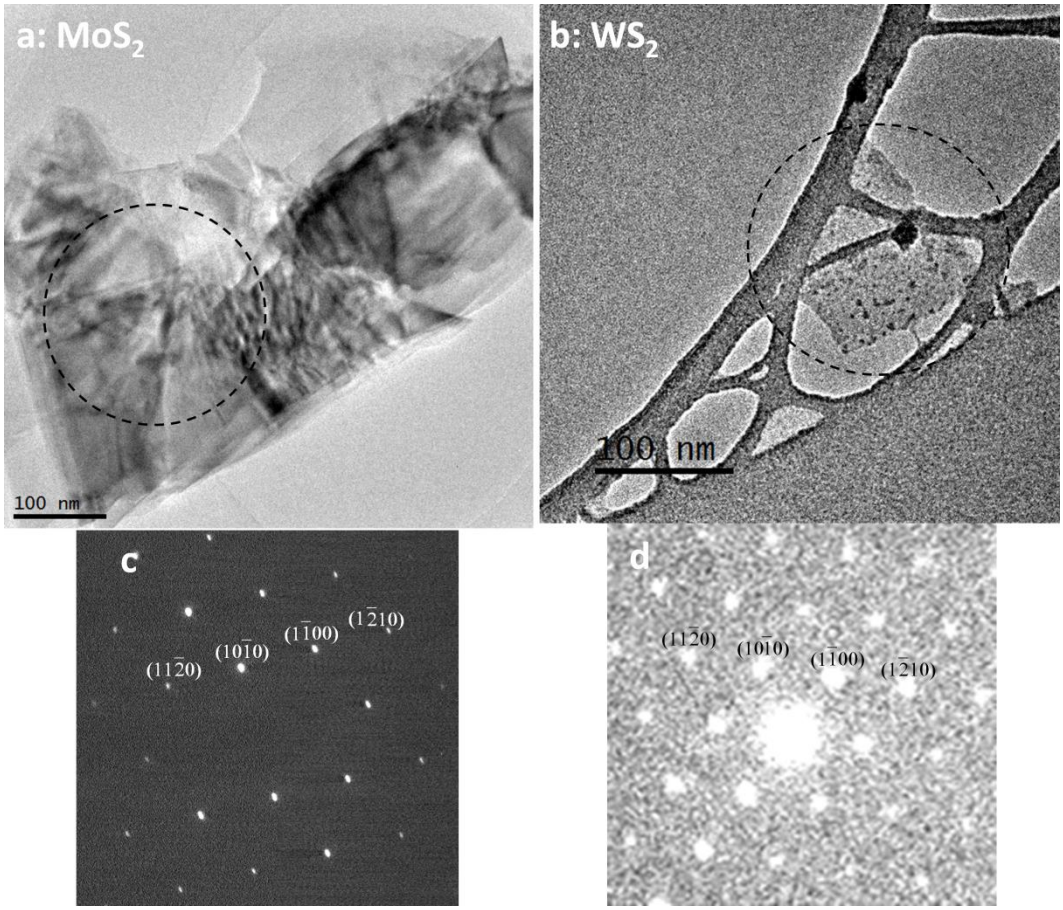


Figure 5.2. (a), (b) Low magnification CTEM images of Mo/WS_2 nanoflakes with corresponding (c) and (d) SAED patterns.

5.1.3 Aberration corrected TEM

The detailed simulations of the HRTEM images of *h*-BN have shown limitations of the oscillating phase-contrast in imaging layered materials with hexagonal symmetry. Therefore, HRTEM simulations were not carried out.

Typical experimental HRTEM images of MoS_2 and WS_2 are shown in Fig. 5.3. The low contrast makes it impossible to assess the thickness or accurately define edge boundaries. Nonetheless, HRTEM allows to assess the presence of structural distortions such as trimerisation and changes in the bond length reported for samples produced by Li-intercalation. Images in Fig. 5.3 show perfect hexagonal structure without detectable changes in the lattice constant. This gives sufficient evidence to claim that structural distortions are limited to the 2D nanostructures produced by intercalation. Finally, images in Fig. 5.3 have large number of the extra bright columns which might be impurities assembled on basal surface. The affinity for adsorbing carbon impurities stems directly from the fact that these materials are used as catalysts.

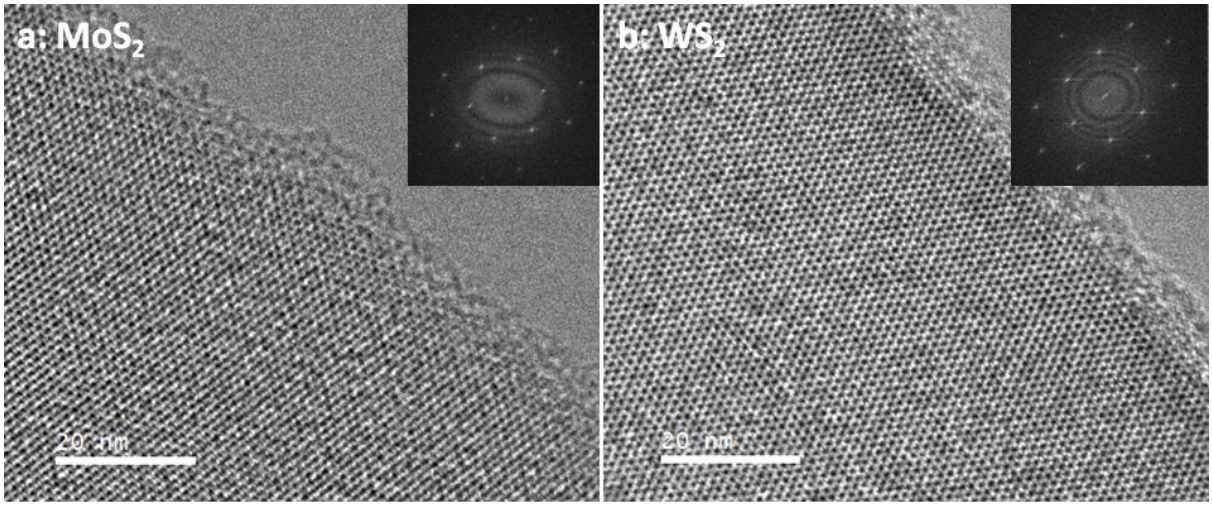


Figure 5.3. HRTEM images of (a) MoS_2 and (b) WS_2 nanosheets.

5.1.4 Aberration corrected STEM

The contrast features of the 2D MoS_2 and WS_2 ADF STEM images are expected to be dominated by the Z-contrast. In particular it should be possible to distinguish atomic columns containing Mo^{4+}(Z=42)/W^{4+}(Z=74) ions from those with S^{2-}(Z=16) ions, when observed in the [001] direction, perpendicular to the basal planes. Furthermore, the strong signal arising from atomic columns containing heavier metal ions can pose difficulty to observe the signal of the nearest, much lighter sulphur columns. The image pattern ultimately generated will depend heavily on the stacking sequence and the number of layers.

In the 2H polytype (Fig. 5.4a) the projected pattern of metal ions will depend on the number of layers: monolayers will produce a simple hexagonal pattern with a single atomic column around each of the 2D Bravais lattice point, whilst multilayers will produce a honeycomb pattern with two atomic columns around each of the 2D Bravais lattice point. The lattice spacings are 3.16 Å and 3.15 Å for MoS_2 and WS_2, respectively.

In the 3R polytype (Fig. 5.4b) the Mo^{4+}/W^{4+} ions in the monolayer and bilayer regions will form hexagonal and honeycomb patterns respectively, similar to the 2H polytype. However, the trilayers will form hexagonal patterns with much smaller lattice spacing (1.83 Å for MoS_2 and 1.82 Å for WS_2). It must be also noted that whilst the patterns formed in the bilayer regions is similar for both the 2H and 3R polytypes, the actual structures are fundamentally different.

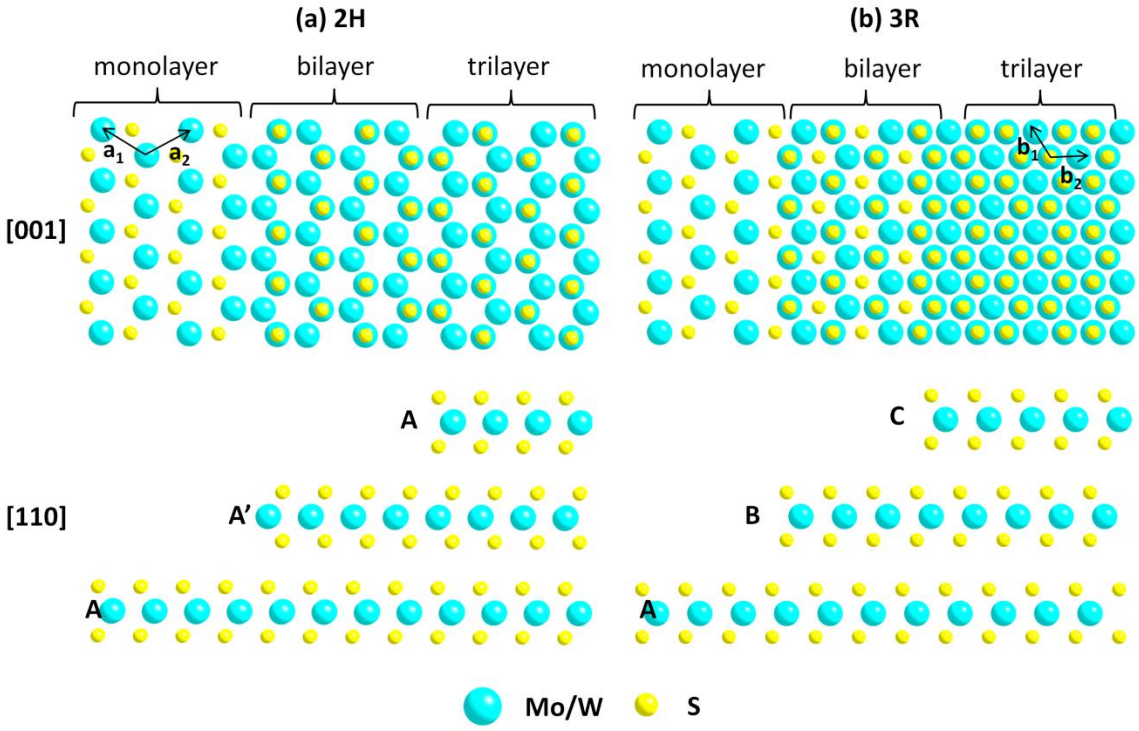


Figure 5.4. Schematic of the MoS_2 and WS_2 (a) 2H and (b) 3R polytypes. Views along [001] direction show the projected features expected to be observed in the experimental ADF STEM images. Views along [110] show unambiguously the alternative stacking sequences correlated with the two different polytypes. Vectors $\mathbf{a_1}$, $\mathbf{a_2}$ and $\mathbf{b_1}$, $\mathbf{b_2}$ represent position vectors of the 2D hexagonal Bravais lattice formed by the atomic columns. $|\mathbf{a_1}| = |\mathbf{a_2}| = \mathbf{3.16}$ Å and $|\mathbf{b_1}| = |\mathbf{b_2}| = \mathbf{1.83}$ Å for MoS_2. $|\mathbf{a_1}| = |\mathbf{a_2}| = \mathbf{3.15}$ Å and $|\mathbf{b_1}| = |\mathbf{b_2}| = \mathbf{1.82}$ Å for WS_2.

5.1.4.1 2D MoS_2

ADF STEM image simulations were computed on the basis of the structural models in Fig. 5.4 to support the discussions above. These are shown in Fig. 5.5. As expected, the image intensity is dominated by the presence of Mo^{4+} columns. In the 2H polytype proportional increase of the peak intensities in the columns with Mo^{4+} is observed with each additional layer (Fig. 5.5c). The situation is more complicated for the 3R polytype because some columns in bilayer and trilayer regions have the same number of equivalent Mo and S atoms, hence, similar peak intensities (Fig. 5.5d).

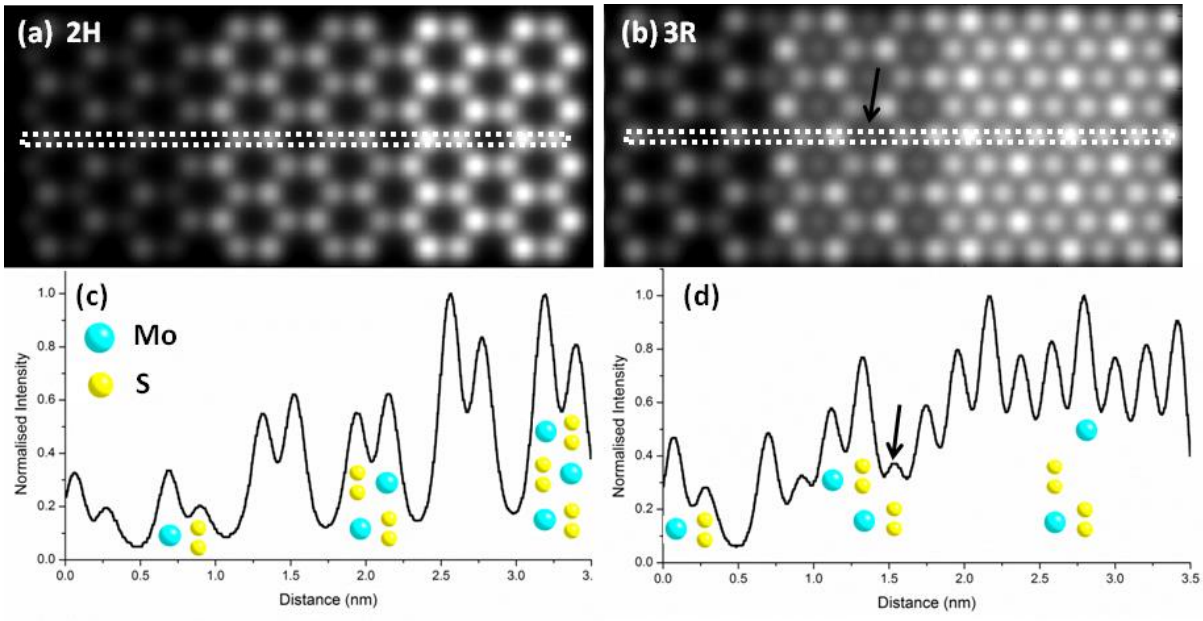


Figure 5.5. ADF STEM simulations of the (a) 2H MoS_2 structure shown in Fig 5.4a and (b) 3R MoS_2 structure shown in Fig. 5.4. (c) and (d) are the corresponding intensity profiles. The arrows in (b) and (c) indicate faint signal from sulphur columns in the bilayer region.

The experimental images agree well with these discussions. Fig. 5.6a shows an image where both hexagonal (region 1) and honeycomb (region 2) patterns are readily identifiable, with lattice spacing of 3.16 Å. On the bases of the above analysis¸ it can be concluded that this sheet is consistent with 2H and 3R polytypes, with region 1 being a monolayer and region 2 being a multi-layer.

In the monolayer region, the intensity arising from the Mo^{4+} ions partially obscures the signal from the S^{2-}. Nonetheless, the position of sulphur columns remains detectable as evidenced by the arrows in the intensity profile (Fig. 5.6b).

The peak intensity in the columns with Mo^{4+} doubles across the step into the multilayer region, correspondingly either to a one-to-two, two-to-four or three-to-six layers steps. Knowing that region 1 is a monolayer is information sufficient to establish that region 2 is indeed a bilayer.

For a 3R bilayer sheets we can expect a weak signal arising from the sulphur columns in the middle of honeycombs (marked with arrows in Figs. 5.5b and 5.5d). Such a signal is not observed in the bilayer region in Fig. 5.6a, implying that this nanosheet has 2H polytype structure. In reality, such faint sulphur signal is probably obscured by the nearby columns. Nonetheless, in the bilayer region of 3R polytype noticeable intensity difference is seen between nearest neighbour columns in the simulation. This is expected because one column has only single Mo^{4+} ion and the second Mo^{4+} and two S^{2-} ions. This difference is much smaller for the bilayer of 2H polytype (simulation) where

nearest neighbour columns have the same numbers of equivalent ions. Hence, it can be concluded that the image in Fig. 5.6 is indeed of 2H polytype. Moreover, unlike simulation (Fig. 5.5a), the experimental image in Fig. 5.6 does not show noticeable difference between nearest neighbour columns in the bilayer. This is explained by the fact that accurate values of the Debye-Waller factors for Mo and S atoms are not known.

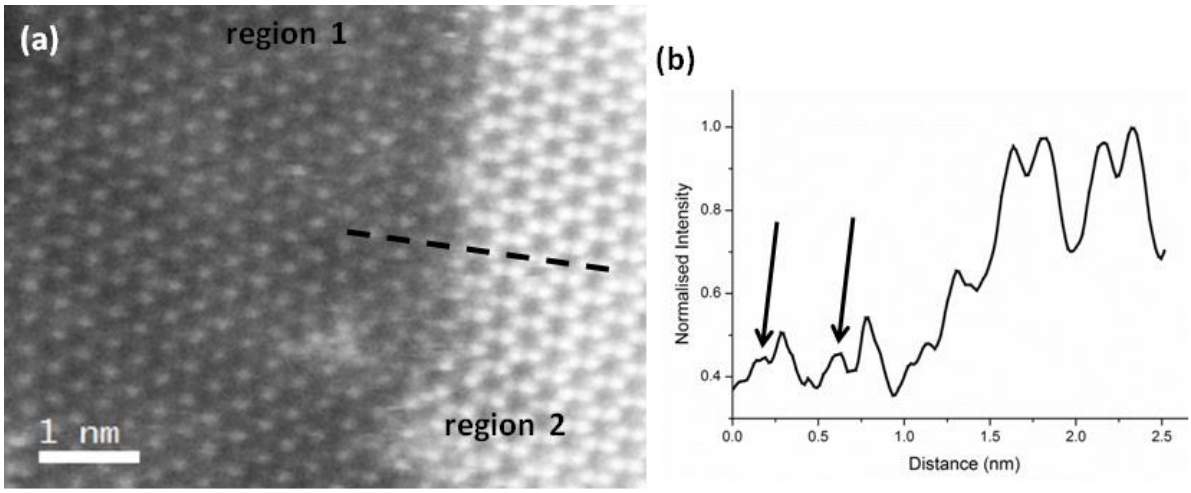


Figure 5.6. (a) ADF STEM image of a typical MoS_2 nanosheet with (b) intensity profile taken along the dotted line. The original image included a much larger field of view and was cropped so that the vacuum region is no longer visible.

The 2H and 3R polytypes can be reliably and quantitatively distinguished by simple analysis of the projected patterns when sheets are ≥ 3 layers thick. An example is given in Fig. 5.7. In Fig. 5.7a the atomic columns form a honeycomb pattern throughout the entire image, confirming a 2H polytype. In Fig. 5.7b the pattern deviates from the honeycomb as we move from the bottom to the top-left corner of the image, where additional atomic columns appear in the centre of each honeycomb, with formation of a hexagonal pattern with 1.83 Å lattice spacing. This projection is consistent with a 3R polytype.

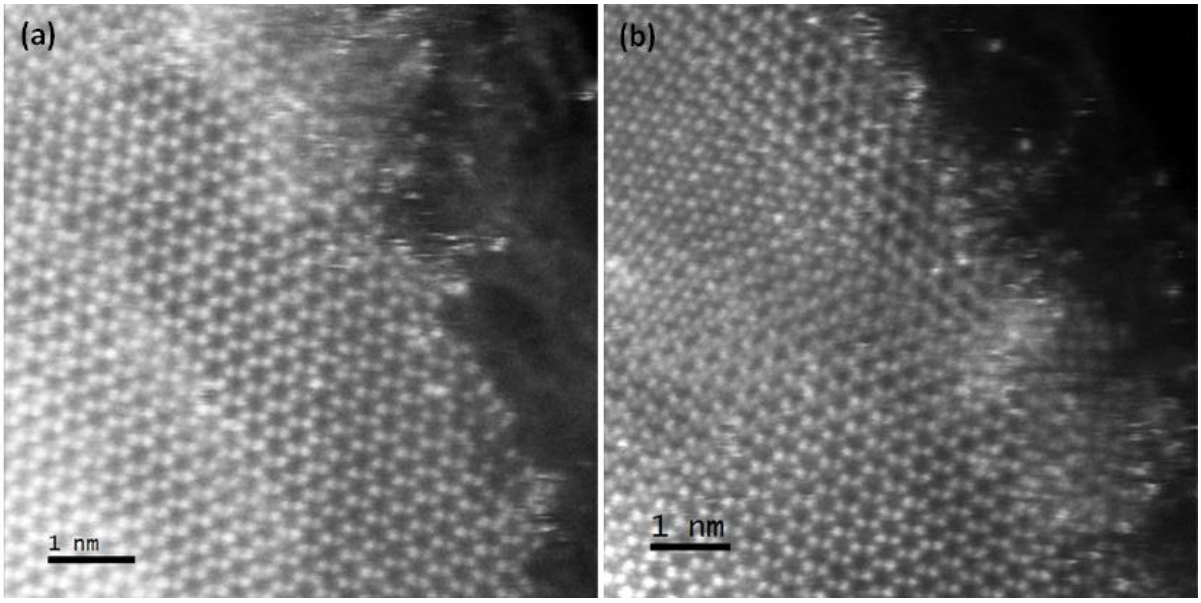


Figure 5.7. (a), (b) ADF STEM images of MoS_2 nanosheets.

An entirely different stacking sequence was however observed in a few cases. In Fig. 5.8a image of a nanosheet displays a hexagonal pattern with 3.16 Å spacing throughout the entire field of view. The intensity profile taken across the flake (Fig. 5.8b; black dotted line) reveals the presence of a step, with intensity doubling across the image, which indicates that monolayer and bilayer regions are both present. The sole explanation for the hexagonal pattern to be maintained throughout the image, both in the monolayer and the bilayer regions, is that the Mo atoms of the second layer are stacked on top of the Mo atoms belonging to the first layer (homonuclear stacking).

The position of the S atoms in this image must be identified in order to propose an appropriate structural model. The intensity profile relative to the monolayer region (taken across the white dotted line) shows diffuse S peaks in the expected positions (see arrows in Fig. 5.8c). In the bilayer region noise, probe tail effects, and off-axis tilts are magnified, hiding the S atoms entirely as a result.

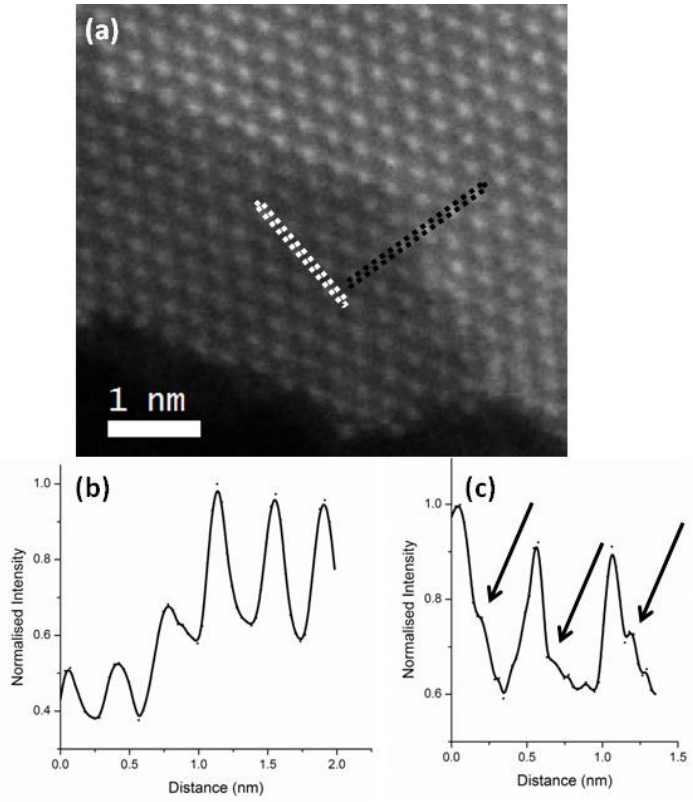


Figure 5.8. (a) ADF STEM image of a MoS_2 nanoflake. (b) Intensity profile taken along the black dotted line. (c) Intensity profile taken along the white dotted line.

The inability to identify the sulphur positions in the bilayer region results in two possible models which can consistently explain the multilayer region in Fig. 5.8a. These can be simply derived from the 2H and 3R polytypes respectively by shifting the second layer of one atomic plane along the vectors R or R* as shown in Fig. 5.9. The new structures can be referred as 1H and 2H' respectively. As indicated in Figs. 5.9c and 5.9d Mo atoms are stacked on the top of each other (homonuclear stacking) in both models. Fig. 5e shows 2D projection of the homonuclear stacked unit cell with two equivalent sites "B" and "C" which can be occupied by the S atoms. In 1H only "B" or "C" site is occupied by S atoms, while in 2H' both sites are occupied. The ADF STEM image simulations of these novel polytypes are given in the Fig. 5.10. They show good agreement with experimental data.

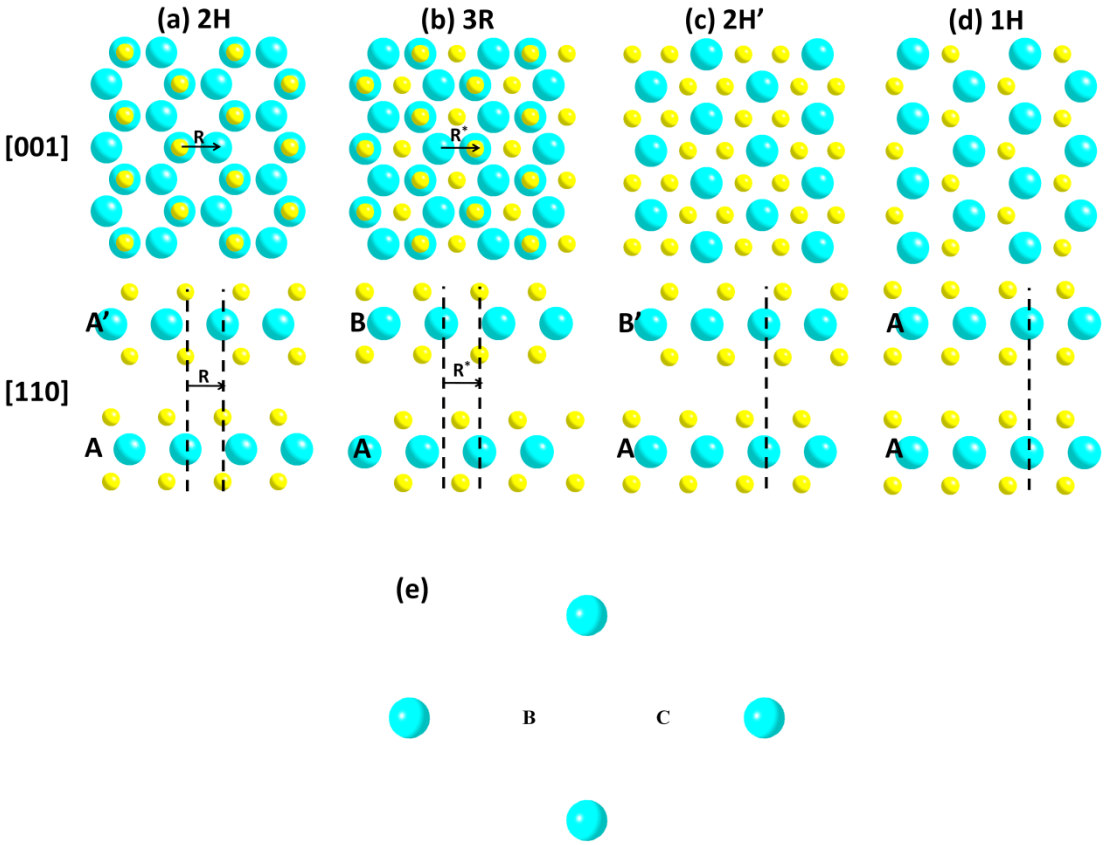


Figure 5.9. The second layers of the (a) 2H and (b) 3R polytypes are shifted respectively along the R and R^* vectors in order to obtain homonuclearly stacked (c) 2H' and (d) 1H structures. (e) 2D projection of the homonuclear stacked unit cell with two equivalent sites "B" and "C" which can be occupied by the S atoms.

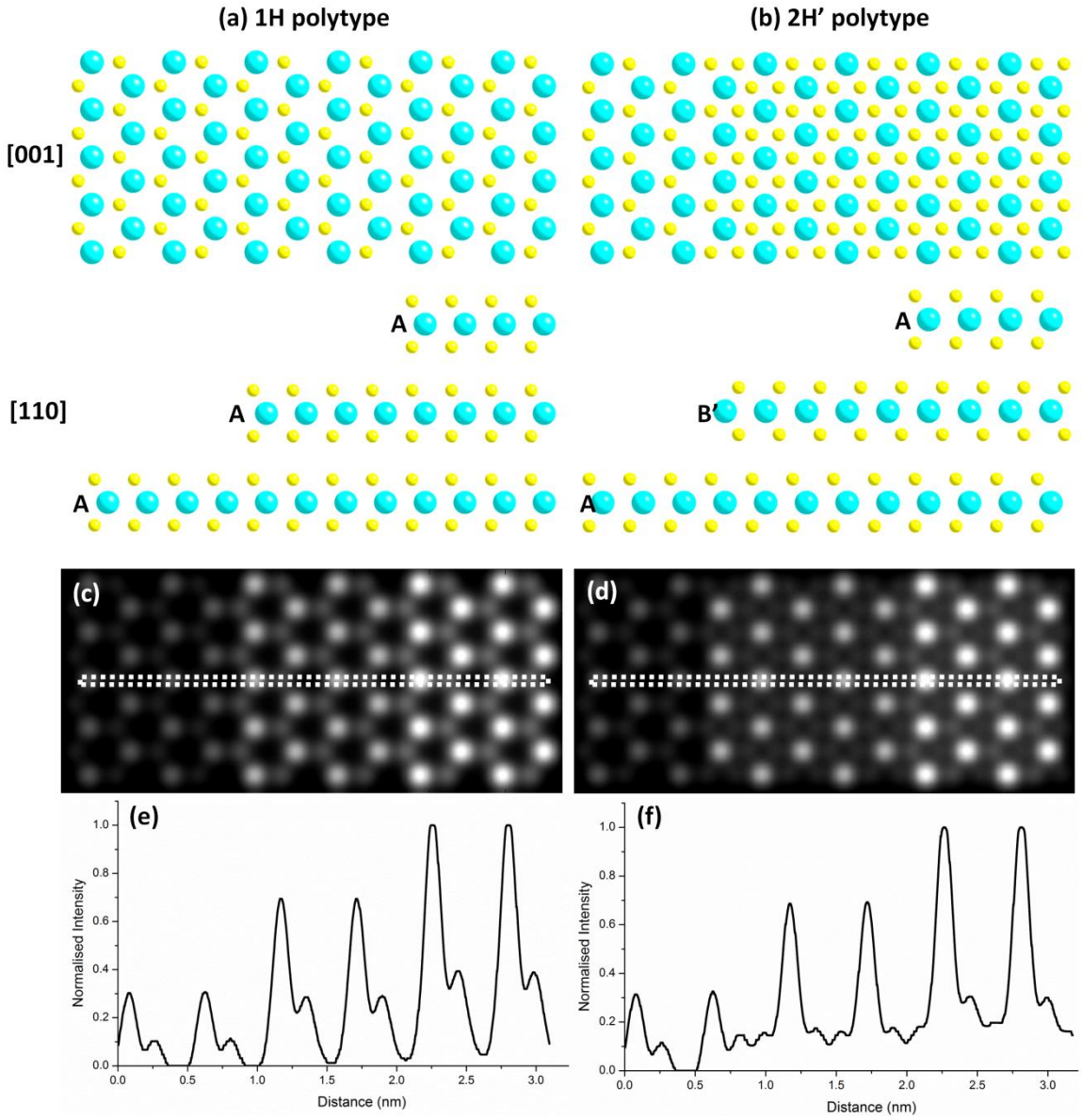


Figure 5.10. Schematic of the MoS_2 (a) 1H and (b) 2H' polytypes with corresponding (c), (d) ADF STEM simulations and (e), (f) intensity profiles.

In addition to the evidence of unusual crystal stacking in liquid-phase exfoliated few-layers MoS_2 nanosheets, some lattice distortions beyond scan noise were noted in the 3R polytype nanosheet (Fig. 5.7b). The displacement was measured for several spots as indicated in Fig. 5.11. Parameters, d_1 and d_2, (marked in Fig. 5.11b) were used to calculate the simple shear strain values using Eq. 4.2 (reproduced here as Eq. 5.1).

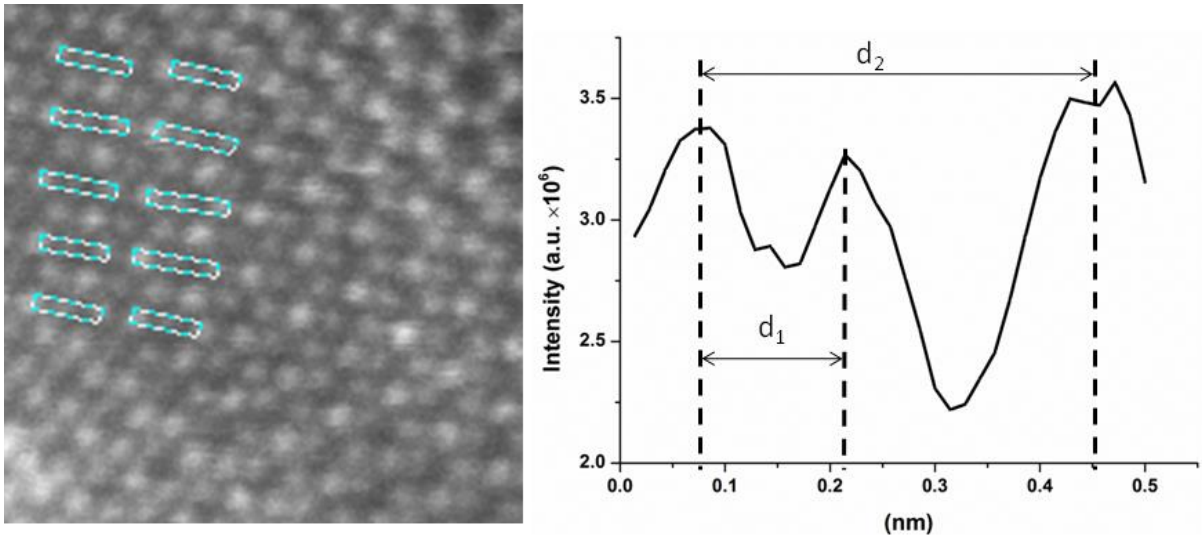


Figure 5.11. (a) Sub-region taken from the image in Fig. 5.7b with indications of the positions for shear strain measurements. (b) Example of the intensity profile from the part a.

$$\text{Simple shear strain} = \frac{|0.5\mathrm{d}_2 - \mathrm{d}_1|}{d_{inter}} \qquad \text{Eq. 5.1}$$

Interlayer distance in the MoS_2 is $d_{inter} = 0.31$ nm. The simple shear strain values were calculated to be between 0.07 and 0.14. The shear strain required to form a 1H from a 3R polytype in a bilayer configuration is 0.61. These distortions are similar to those observed in the non-bulk *h*-BN nanoflakes. However, in this case the observed displacement can also be caused by the sample tilt because the region is only three layers thick. The tilt which can produce the observed displacement for the trilayer is between 2 and 5 degrees.

From the 27 different MoS_2 nanoflakes imaged and analysed, 17 were found to be consisted with a 2H polytype, 9 with a homonuclear stacking and only one with a 3R polytype. A single case where the nanoflake displayed combination of stacking sequences was also observed (Fig. 5.12). In Fig. 5.12 three layers have homonuclear stacking and the fourth is shifted resembling distorted 2H.

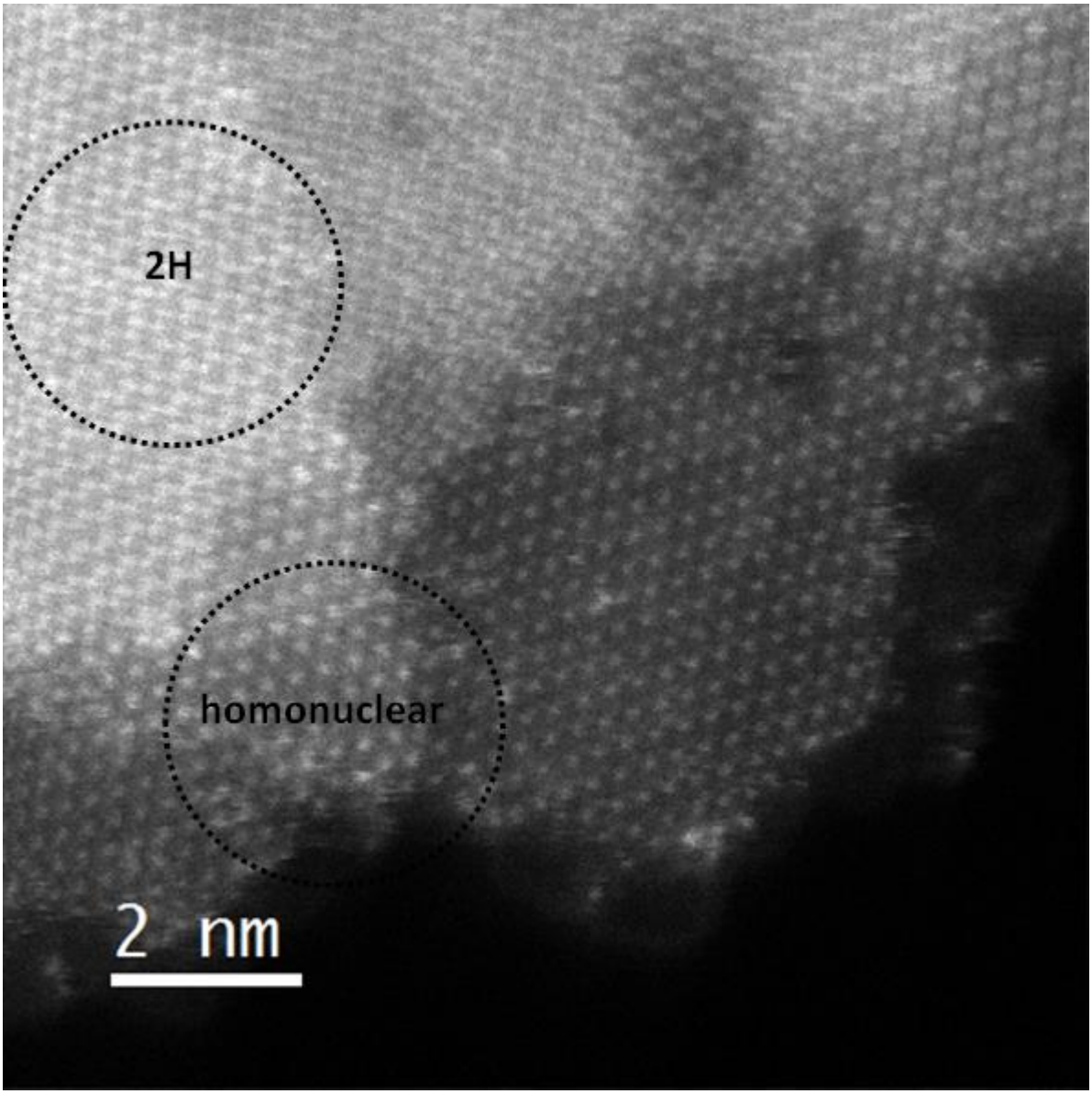


Figure 5.12. ADF STEM image of a MoS_2 nanoflake.

5.1.4.2 2D WS_2

A similar structural analysis was carried out on ADF STEM images of WS_2 nanosheets. In Fig. 5.13a the image of a WS_2 nanosheet is consistent with the 2H polytype. Similarly to MoS_2, the monolayer region has a hexagonal pattern with 3.15 Å spacing whilst the multilayer region shows a honeycomb pattern. Counting of the number of layers can once again be confirmed by analysis of the intensity profile across the sheet, revealing a step transition between a monolayer and bilayer (Fig. 5.13b). The strong contrast originating from high-Z W atoms (Z = 74) makes the S atoms (Z = 32) in monolayers completely disappear.

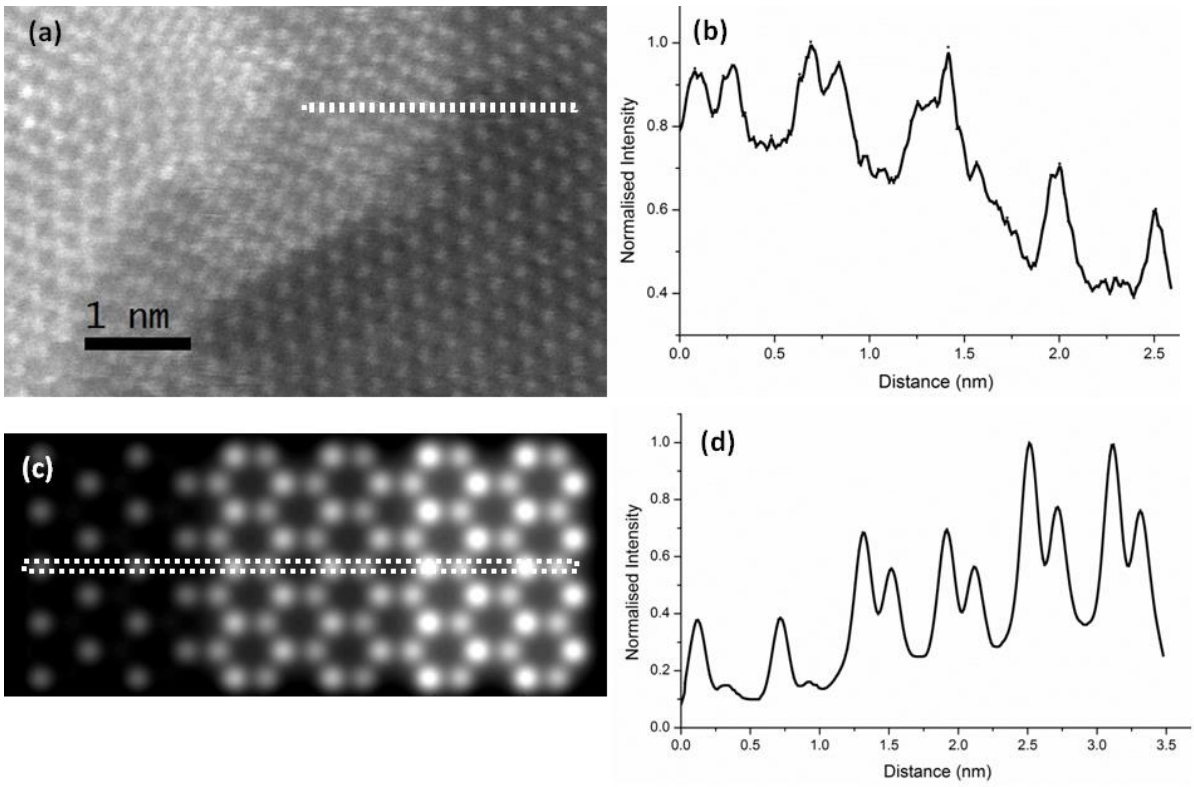


Figure 5.13. (a) ADF STEM image of WS_2 nanosheet with corresponding (b) intensity profile drawn across the white dotted line. The image in (a) was originally cropped to remove the vacuum from the field of view. (c) ADF image simulation of the WS_2 structure shown in Fig. 5.4a with (d) corresponding intensity profile.

ADF simulations were carried out to corroborate image interpretation. Since WS_2 is isostructural to MoS_2 we used the same model as in Fig. 5.4a, with the appropriate modification of the lattice spacing. The simulation results are shown in Fig. 5.14c, together with the relative intensity profile across the step (Fig. 5.14d). As expected, the intensity on the monolayer region is dominated by a very strong signal generated by the W atoms, whilst the S atoms are almost completely hidden.

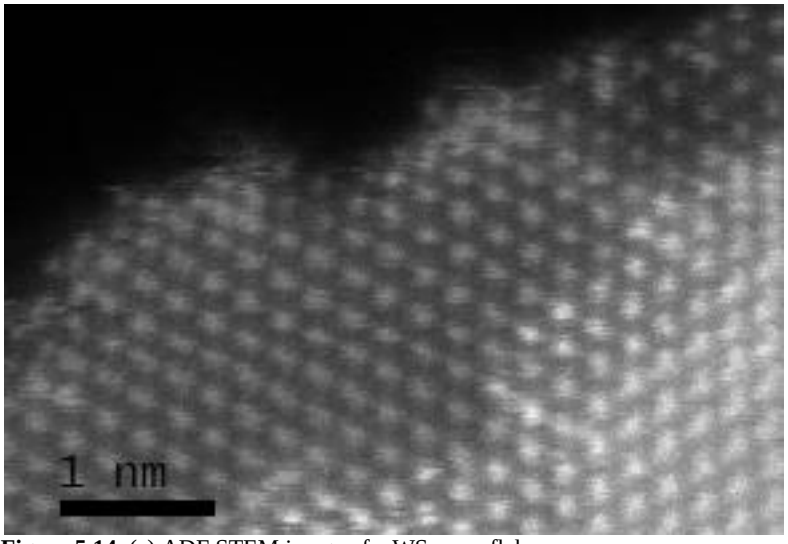


Figure 5.14. (a) ADF STEM image of a WS_2 nanoflake.

As in the case of liquid-phase exfoliated MoS_2 flakes, WS_2 did not always show sole evidence for 2H polytype. Fig. 5.14 shows a stepped nanoflake where the hexagonal pattern is preserved over the whole field of view. Once again, the only explanation can be that the W atoms of each consecutive layer are stacked homonuclearly on the top of the W atoms of the previous layer. The two possible models are the 2H' and the 1H described in Fig. 5.9.

Finally, the position of the S atoms in the protruding monolayer in Fig. 5.13a can be determined by careful statistical analysis on the ADF intensities. Similar to MoS_2, W atoms form hexagonal structure with two equivalent sites "B" and "C" (Fig. 5.9e) which can be occupied by the S atoms. The calculated normalised averaged intensities at the "B" and "C" sites in the monolayer region of the Fig. 5.13a are 1.000 ± 0.010 and 0.959 ± 0.012 respectively. The difference is small but nevertheless statistically distinguishable and significant. Furthermore, positions of the S columns might be accurately determined by collecting ADF and annular BF signal. The missing sulphur columns are expected to be resolved in the annular BF image.

Overall, from the 5 different WS_2 nanosheets imaged and analysed only one was consistent with the 2H polytype, while all the others possessed homonuclear stacking. A 3R polytype was never observed.

5.2 2D TiS2

5.2.1 Introduction

Stoichiometric TiS_2 is chemically synthesized compound with 1T polytype structure (Fig. 5.15) where the monolayer structure repeats itself along [001] direction. Its unit cell lattice parameters are $\{0.340\ \text{nm}, 0.340\ \text{nm}, 0.570\ \text{nm}, \pi/2, \pi/2, \pi/3\}$ [185].

Bulk TiS_2 is a semi-metal [186] with several theoretical papers predicting semiconductor transition upon exfoliation [187] resulting in 1 eV indirect bandgap for a monolayer [188]. This material is well known for its high diffusion rate of Li ions into the crystal lattice being used in the past as cathode material in rechargeable batteries [189]. Its use in the batteries was discontinued due to fast degradation of the cathode.

Exfoliated TiS_2 was only recently reported by Zeng et al who produced it using Li-intercalated intermediate [47]. Thin films prepared from exfoliated nanosheets demonstrated high electrical conductivity and were proposed for stamp transferrable electrodes [190]. The only structural characterisation reported up-to-date involves basic TEM imaging complemented by the SAED [191].

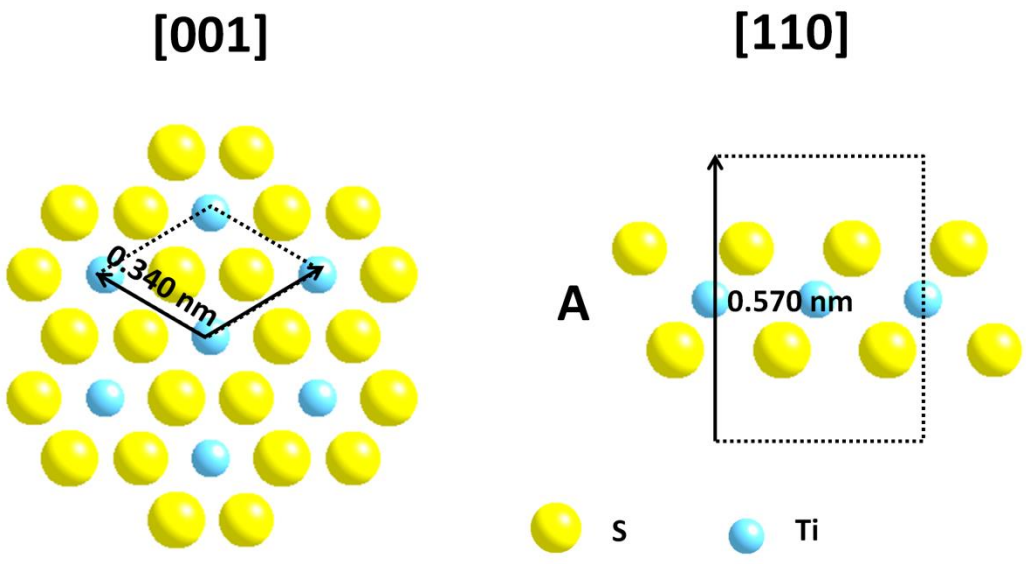


Figure 5.15. Structural model of the bulk TiS_2. View along [001] shows the projected structures recorded in the atomically resolved images. View along [110] unambiguously shows stacking sequences. The interlayer distance of [110] view is shown to scale with respect to the interatomic distances of the [001] view. Dashed lines are used to indicate unit cell.

5.2.2 Conventional TEM and Diffraction

Conventional CTEM of TiS_2 nanoflakes provided initial insight about the samples. Figs. 5.16a, 5.16b show typical multi-layered nanoflakes. The 1T structure of the TiS_2 crystals consists of layers stacking exactly on the top of each other. In projection, 2D structure and structure factors for [001] beam direction are the same for monolayer and multi-layers. Therefore, intensity ratio of the diffracted spots cannot be used to distinguish monolayer and multi-layer regions. Instead, the calculated intensity ratio, $I_{\{10\bar{1}0\}}/I_{\{11\bar{2}0\}}$, can be compared with experimental ratios to check for abnormalities in the stacking. Experimental ratios: 0.074 ± 0.014 (Fig. 5.16c) and 0.076 ± 0.030 (Fig. 5.16d) are approximately four times larger than calculated (0.017). Assuming that B-factor is 1.5 Å^2 the contribution of the Debye-Waller factor is $e^{-\frac{B}{4}\left(g^2_{\{10\bar{1}0\}}-g^2_{\{11\bar{2}0\}}\right)} = 1.1$, which is negligible.

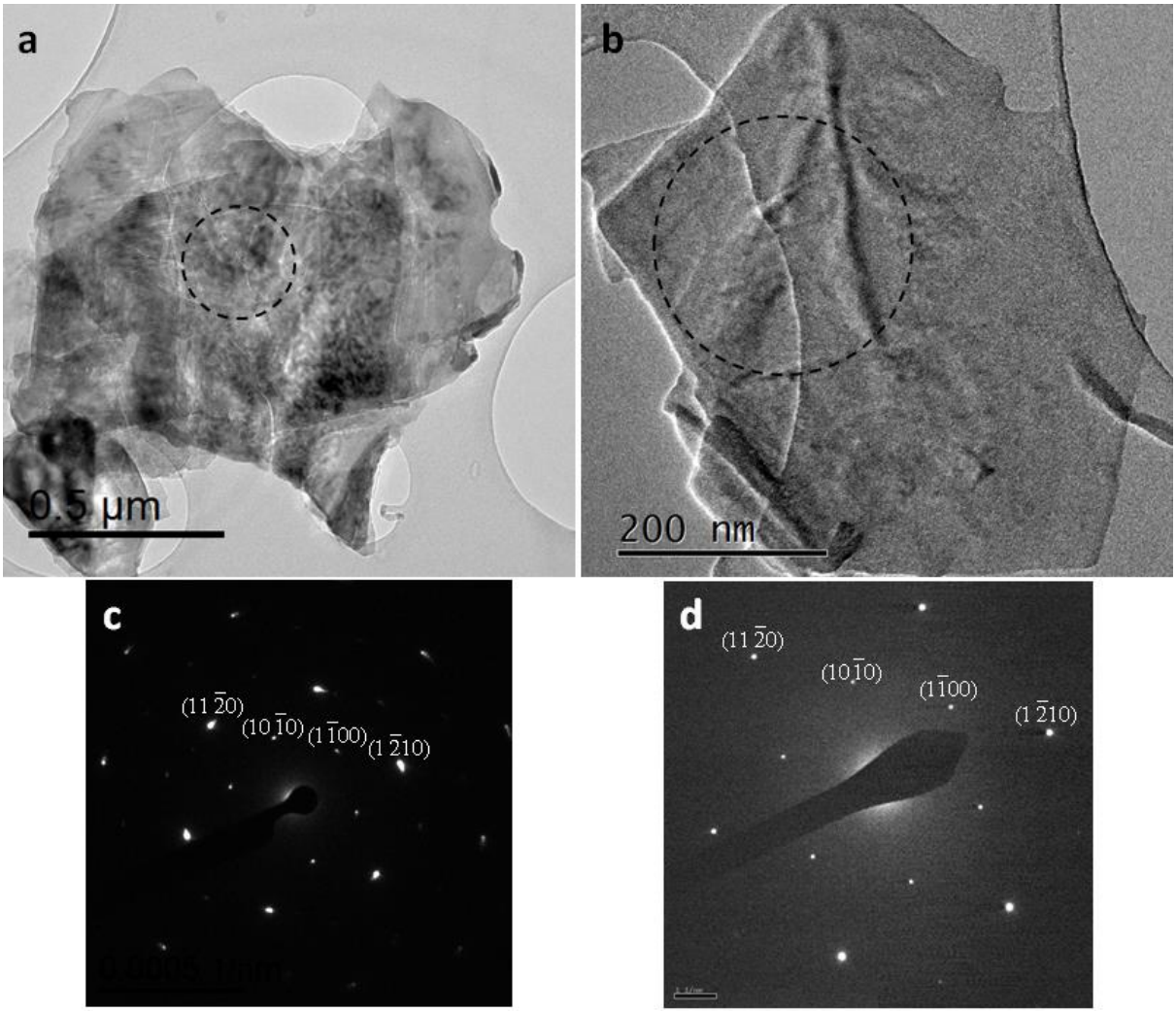


Figure 5.16. (a), (b) Low magnification CTEM images of TiS_2 nanoflakes with corresponding (c) and (d) SAED patterns.

The first attempt to explain this difference was to consider several high-symmetry models and calculate corresponding intensity ratios. These models are AB and ABC, produced by shifting appropriate layers along vector ***R*** marked in Fig. 5.17, similar to the models described for *h*-BN. The diffraction spot intensity ratios for AB and ABC are 4.34×10^{-3} and 0, respectively.

The second step was to consider changes in the internal structure of the layers. The majority of the transition metal dichalcogenides have either octahedral coordination or trigonal prismatic. Hence, a 1T → 2H transformation was assumed with no changes in the Mo-Mo distance. The calculated diffraction spot intensity ratio for TiS_2 2H structure is 0.77. This indicates that it might be possible to obtain experimentally observed ratio in structure consisting of monolayers with different coordination of the Ti^{4+} ion.

Again, it must be stressed that different structures considered here only serve to provide initial insight into the sample's structure. Due to the reasons already explained for MoS_2 and WS_2, SAED of the restacked TiS_2 nanoflakes was not carried out.

5.2.3 Aberration-corrected STEM

Similar to the case of MoS_2 and WS_2, Z contrast is expected to provide distinction between atomic columns containing Ti^{4+} (Z = 22) ions and S^{2-} (Z = 16), when observed in the [001] direction perpendicular to the basal planes. Again for the interpretation of the structure and the stacking it is easier to consider the projected pattern formed by the Ti^{4+} ions.

In the 1T polytype (Fig. 5.17) the projected pattern of the Ti^{4+} ions does not depend on the number of layers. It always forms simple hexagonal pattern with a single atomic column around each of the 2D Bravais lattice points with the bulk lattice spacing. Hence any deviation from this pattern is direct evidence of the novel stacking.

ADF image simulation was computed on the basis of the structural model in Fig. 5.19 to support the discussion above and is shown in Fig. 5.18. The image intensity is still dominated by the Ti^{4+} ions but S^{2-} columns are now more pronounced relative to the Mo/WS_2 cases.

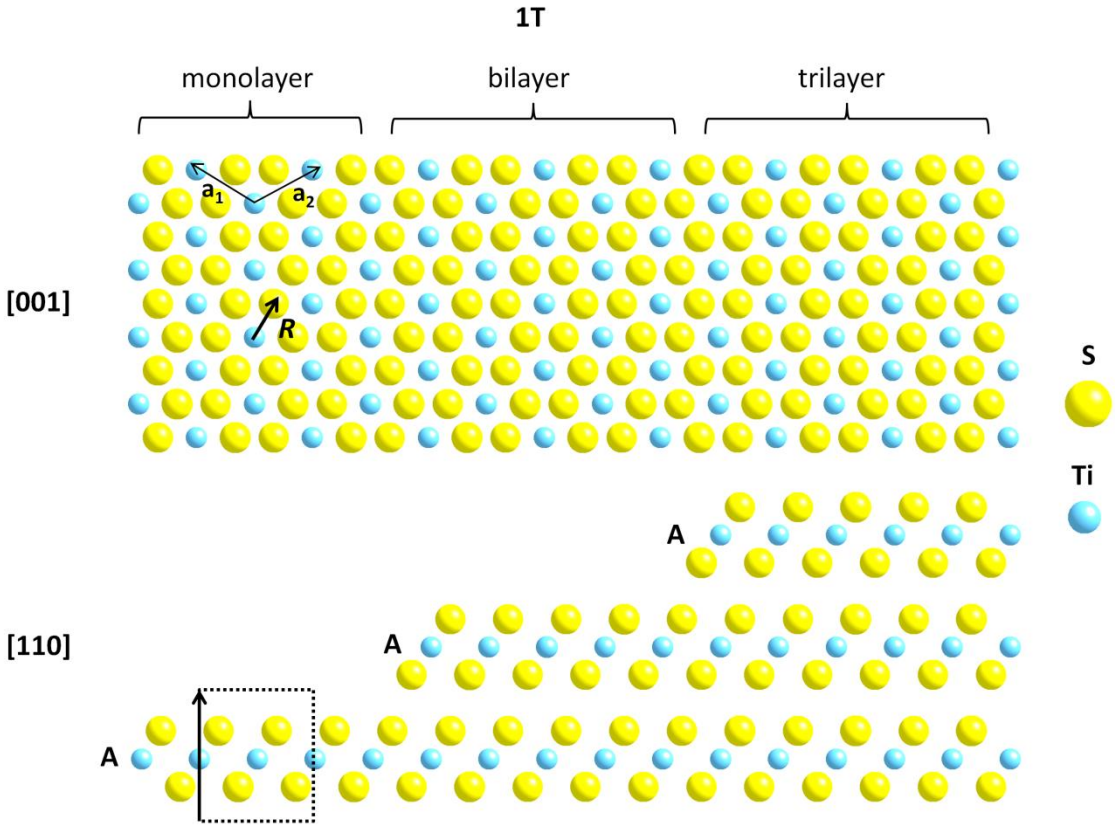


Figure 5.17. Schematic of the TiS_2 1T polytype. View along [001] direction shows the projected features expected to be observed in the experimental ADF STEM images. View along [110] shows unambiguously stacking sequence.

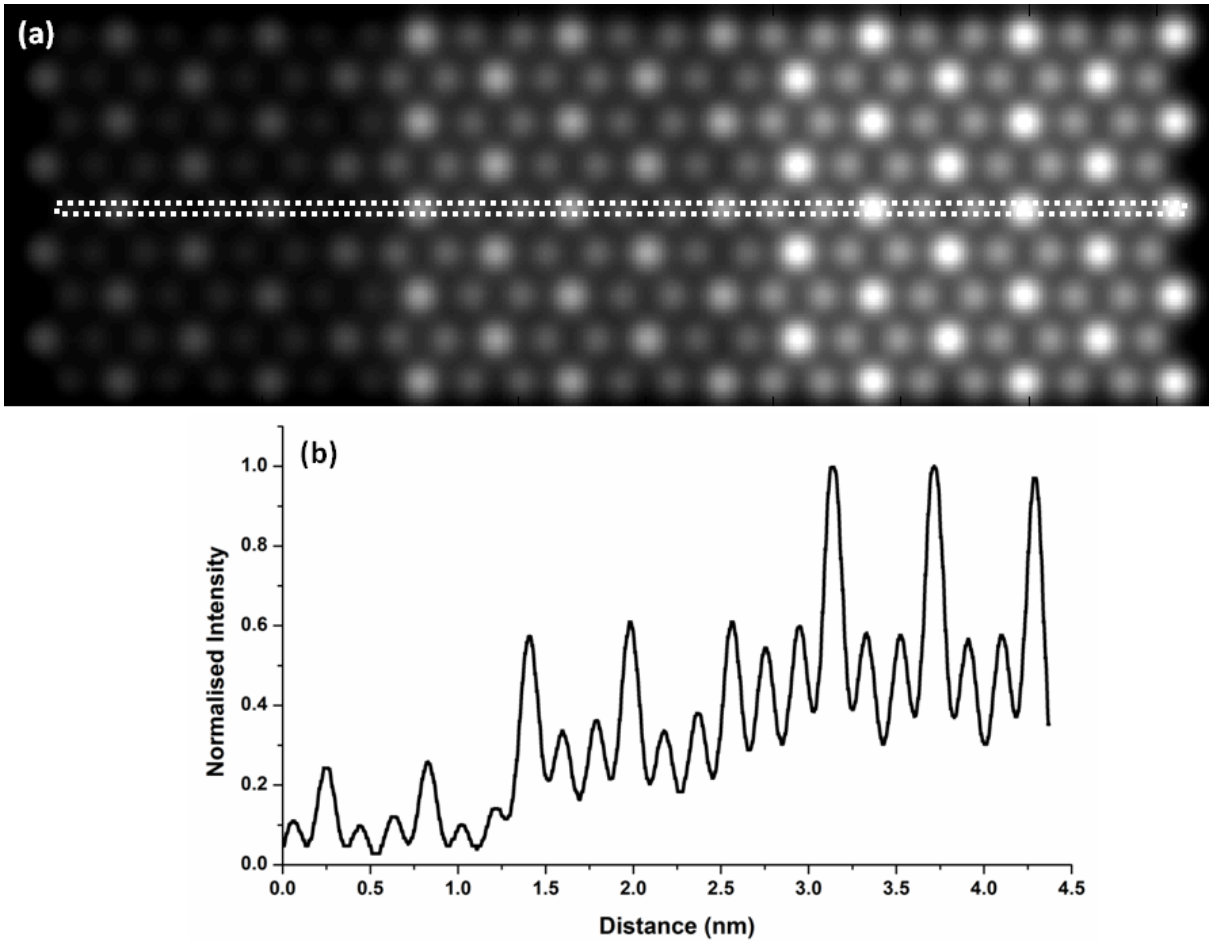


Figure 5.18. (a) ADF STEM simulation of the 1T TiS_2 structure shown in Fig. 5.17 with (b) corresponding intensity profile.

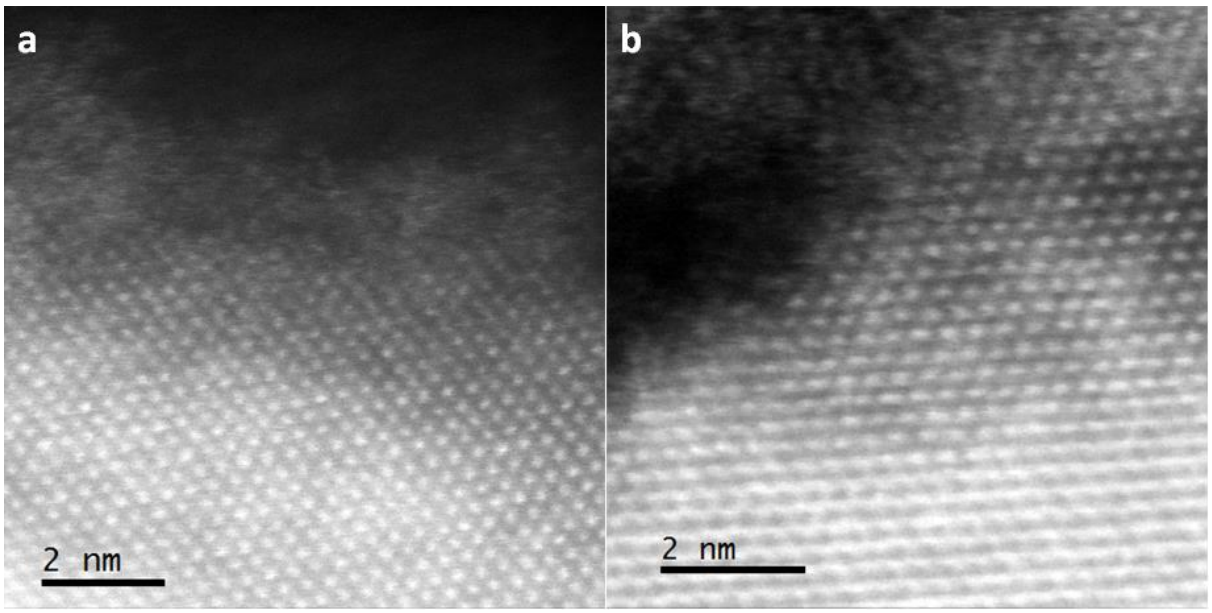


Figure 5.19. (a), (b) ADF STEM images of the TiS_2.

Simple hexagonal pattern of the Ti^{4+} columns is readily observed in the experimental images (Fig. 5.19a). In a single case (Fig. 5.19b) the image displays both simple hexagonal (upper part of the image) and honeycomb patterns (lower part of the image). The presence of honeycomb pattern provides direct evidence of the non-bulk stacking in the exfoliated TiS_2 nanoflakes. Additionally, an image where 1T structure was contaminated with the unknown phase was identified (Fig. 5.20a). As can be seen from FFT of this image (Fig. 5.20b) there are spatial frequencies (marked with red circles) which are not present in the 1T structure. This unidentified phase retains hexagonal symmetry with 4.34 Å in-plane lattice constant. It is ~27% higher than lattice constant of the 1T phase. Finally, none of the images displayed step-wise increase in intensity which could assist in estimating the thickness of the nanoflakes. Moreover, some of the images displayed local variation in the contrast (Fig. 5.20a) which is unusual feature for chemically exfoliated nanoflakes. Typically intensity/thickness increases step-wise or continuously from the edge towards the middle of the nanoflakes. Out of 6 imaged nanoflakes 4 demonstrated bulk structure. Other two cases are described above.

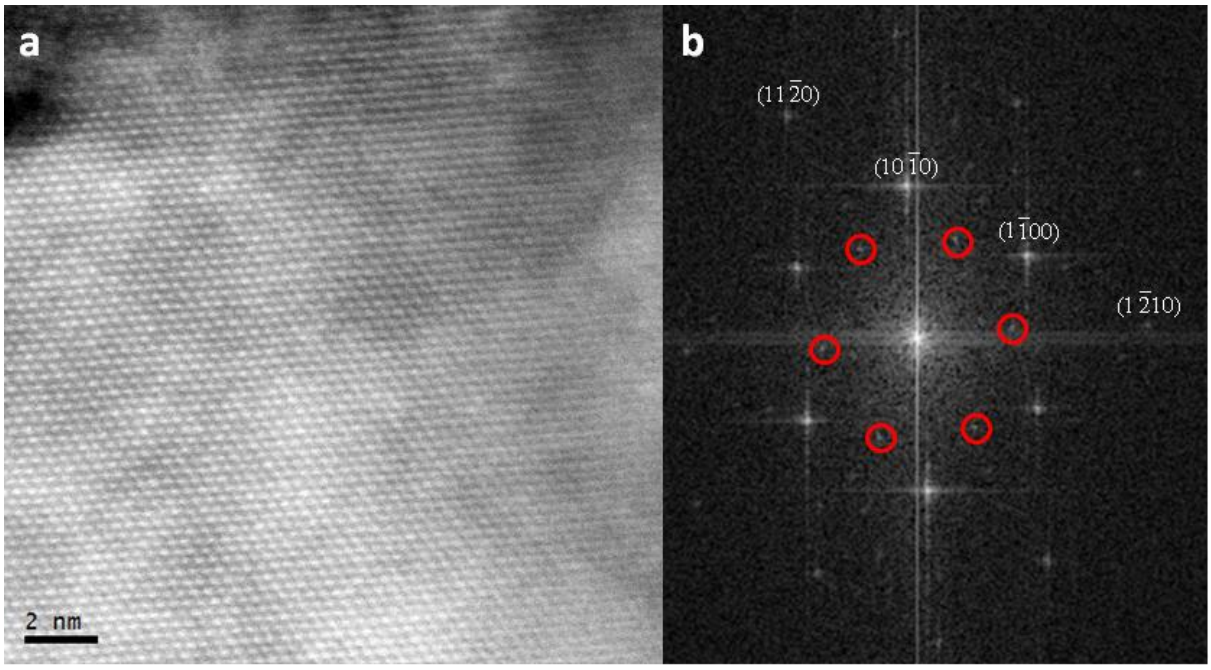


Figure 5.20. (a) ADF image of TiS_2 nanoflake with (b) corresponding FFT. The broken six-fold symmetry in the FFT is attributed to the sample drift.

5.2.4 EELS

The unexpected local variations in contrast were attributed to the possible deterioration of the nanoflakes due to oxidation. The validity of this assumption was assessed using EELS analysis. Fig. 5.21a shows ADF STEM image of the nanoflake and region over which spectrum image was acquired. The averaged spectrum (Fig. 5.21b; 230 frames) shows carbon K-edge at ~300 eV and Ti $L_{2,3}$ edge at ~460 eV. Oxygen K-edge is expected at ~535 eV, however, only very weak signal is observed in Fig. 5.21b. An attempt to produce oxygen map based on the spectrum image was not successful due to the poor signal. Strong carbon K-edge indicates that sample is badly contaminated making it impossible to resolve the atomic structure (Fig. 5.21a).

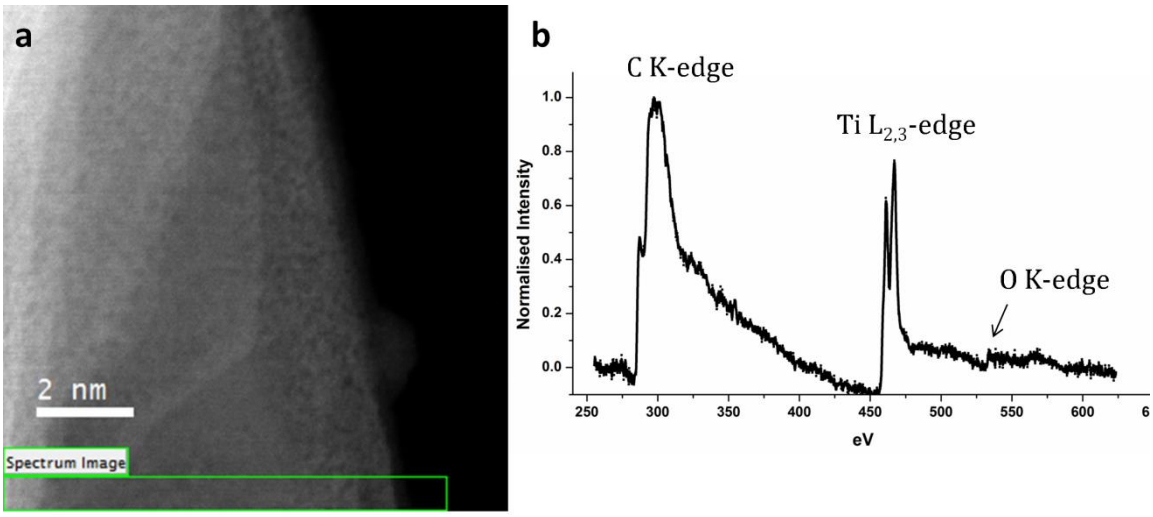


Figure 5.21. (a) ADF image of the TiS_2 nanoflake with EELS spectrum averaged over 230 frames. EELS acquisition details: drift tube voltage (280 V), exposure (0.5 s/frame), convergence semi-angle (33 mrad), collection semi-angle (31 mrad), dispersion (0.3 eV/ch).

5.3 Summary of the findings

2D nanostructures of the MoS_2, WS_2 and TiS_2 were investigated for structural differences as compared with 3D equivalents. On the basis of ADF STEM and image simulations it was determined that in all three cases non-bulk stacking can exist. Two structural models, here referred as 1H and 2H' polytypes, were proposed for 2D MoS_2 and WS_2 with non-bulk stacking. This previously unreported homonuclear stacking consists of metal ions placed exactly on top of each other for each consecutive layer. The reason for the two possible models is inability to resolve sulphur column positions in ADF STEM images. This problem might be resolved by simultaneous acquisition of the BF and DF signals.

In addition ADF STEM images of 2D TiS_2 showed unexpected local variations in contrast. The assumption that this is caused by oxidation of the samples was not fully confirmed, although EELS indicated the presence of oxygen.

27 different MoS_2 nanoflakes were imaged and analysed. Amongst these 17 were consistent with a 2H polytype, 9 with a homonuclear stacking and only 1 with a 3R polytype. Moreover, a nanoflake displaying both homonuclear and 2H stacking was also observed. The nanoflake in 3R polytype configuration exhibited a significantly strained lattice. Amongst the 5 examined WS_2 nanoflakes, one exhibited a 2H structure, whilst all the others were consistent with homonuclear stacking. The 3R polytype was never observed for WS_2. 6 TiS_2 nanoflakes were analysed. 4 were consistent with 1T polytype and one with non-bulk stacking. In the last case 1T structure and unknown phase with non-bulk lattice constant was identified.

Chapter 6: Hexabenzocoronene

In this chapter results of the imaging of liquid-phase exfoliated hexabenzocoronene (HBC) molecules are discussed. The aim of this investigation was imaging of individual HBC molecules in order to confirm successful liquid-phase exfoliation. HRTEM images are acquired by Prof. Valeria Nicolosi. ADF STEM images are acquired by Mervyn Shannon.

6.1 Introduction

HBC is a polycyclic aromatic hydrocarbon (PAH) and a member of the coronene family (Fig. 6.1). It was first synthesized and studied by Erich Clar in 1959 [197]. Initial interest in the large PAHs stemmed from synthetic chemistry [198] but with the discovery of graphene, PAHs are now considered transition molecules from benzene to graphene [199] [200]. Graphene itself can be regarded as a giant PAH. An interest towards HBC was also noted in astrophysics where the presence of this molecule is used to explain diffuse interstellar visible absorption bands [201][202][203].

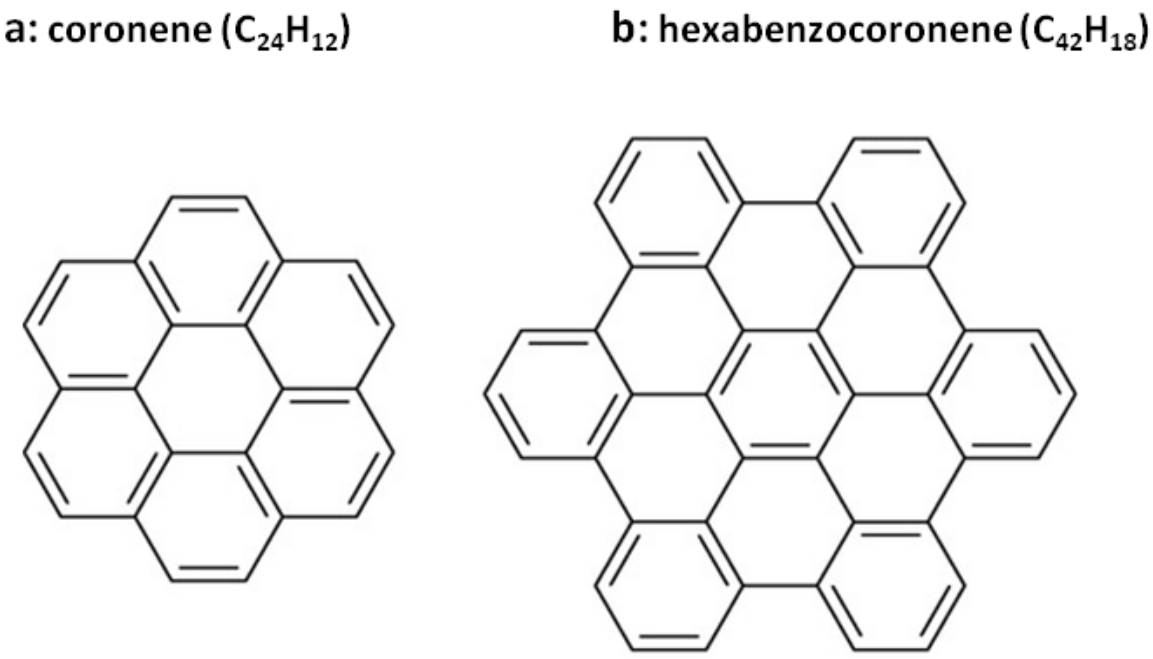


Figure 6.1. Schematics of the (a) coronene and (b) hexabenzocoronene molecules.

For the effective study of HBC and other PAHs, solubility in common solvents is required. For a long time only one organic solvent (1,2,4-trichlorobenzene) was known

to disperse HBC. This problem was solved by attaching functional groups to the edge carbon, rendering HBC soluble [204] [205]. Practical possibilities of applying chemically modified HBC were quickly noted. Thin films drop-cast from solution showed potential in thin film transistors [206] [207] [208] and heterojunction solar cells [209][207][210]. Unfortunately functional groups attached to the edge of HBC are expected to change morphology of the deposited films. Therefore, the drive to exfoliate HBC in ordinary solvents remained. It has recently been demonstrated that HBC can be dispersed to the level of single molecules in aqueous surfactant solutions [211]. Later, exfoliation of HBC was extended to the solvents used for chemical exfoliation of graphene following the same methodology [91].

6.2 Imaging

Imaging and manipulation of individual light molecules is a challenging task. Certain success was achieved using STM [212] and AFM [213] techniques but unfortunately such techniques are less suitable than TEM for searching large areas. In the past, the TEM approach was only partially successful in imaging individual light molecules due to the strong radiation damage. The samples were limited to small molecules immobilised in carbon nanotubes [214]. Here, the relatively large size of the HBC is expected to increase the chances of observing individual molecules [91]. On account of the deposition of the samples from solution alongside the individual molecules, self-assembled and partially-exfoliated clusters are expected. It is important to highlight that challenge in TEM imaging comes from the fact that HBC is a light carbon based molecule. Imaging of heavy molecules and even individual atoms is routine and does not pose a challenge [79].

6.2.1 Aberration-corrected TEM

HBC samples were deposited on ultrathin amorphous carbon (< 3nm thick). Therefore any crystalline phase can be attributed to the individual HBC molecules or its agglomerates. The best image with the greatest resemblance to the HBC molecule is given in Fig. 6.2, where the appropriate area is marked with the white circle. Lattice spacing is 0.24 nm which agrees with the spacing of HBC. Upon closer examination, this crystalline patch consists of two self-assembled HBC molecules where one of them has been partially destroyed by the electron beam. Unfortunately, in the majority of cases,

instead of the individual molecules, patches of crystalline phase with area much larger than the HBC molecule are observed (Fig. 6.3). Moreover, the crystalline patches have well-resolved 90^{o} symmetry with 0.24 nm lattice spacing. It appears that these non-hexagonal structures are formed under the electron beam. Such behaviour is particularly interesting from an application viewpoint because similar phase transformation can be expected in HBC based electronic devices. The approximate radiation dose for a 1s exposure and ~30 nm in diameter viewing area is $\sim 10^{4}$ $e^{-}/Å^{2}$. In reality larger radiation dose can be expected because it takes at least 10-20 seconds to locate the suitable patch and zoom in on the sample.

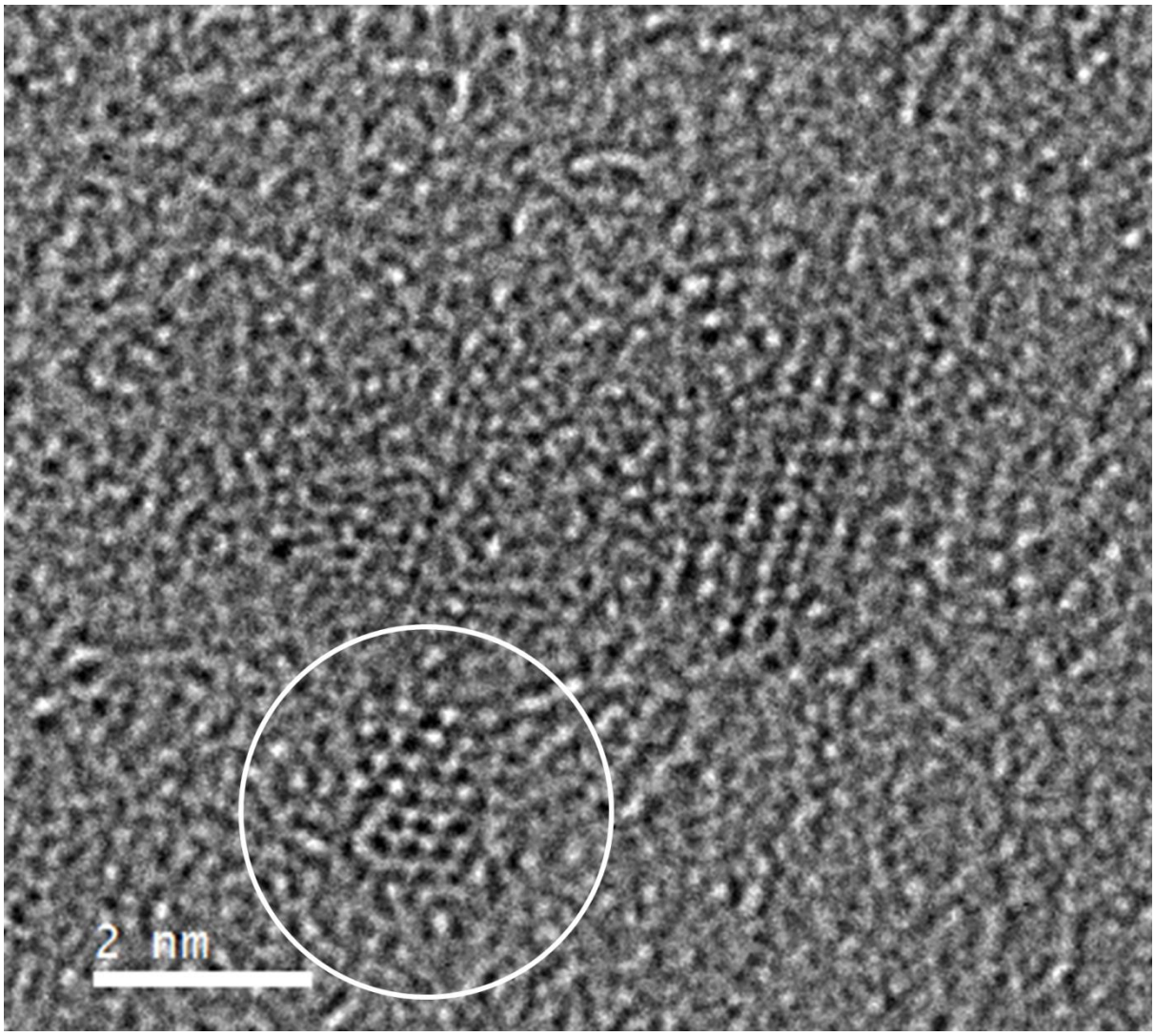


Figure 6.2. HRTEM image of the HBC molecules on ultrathin amorphous carbon.

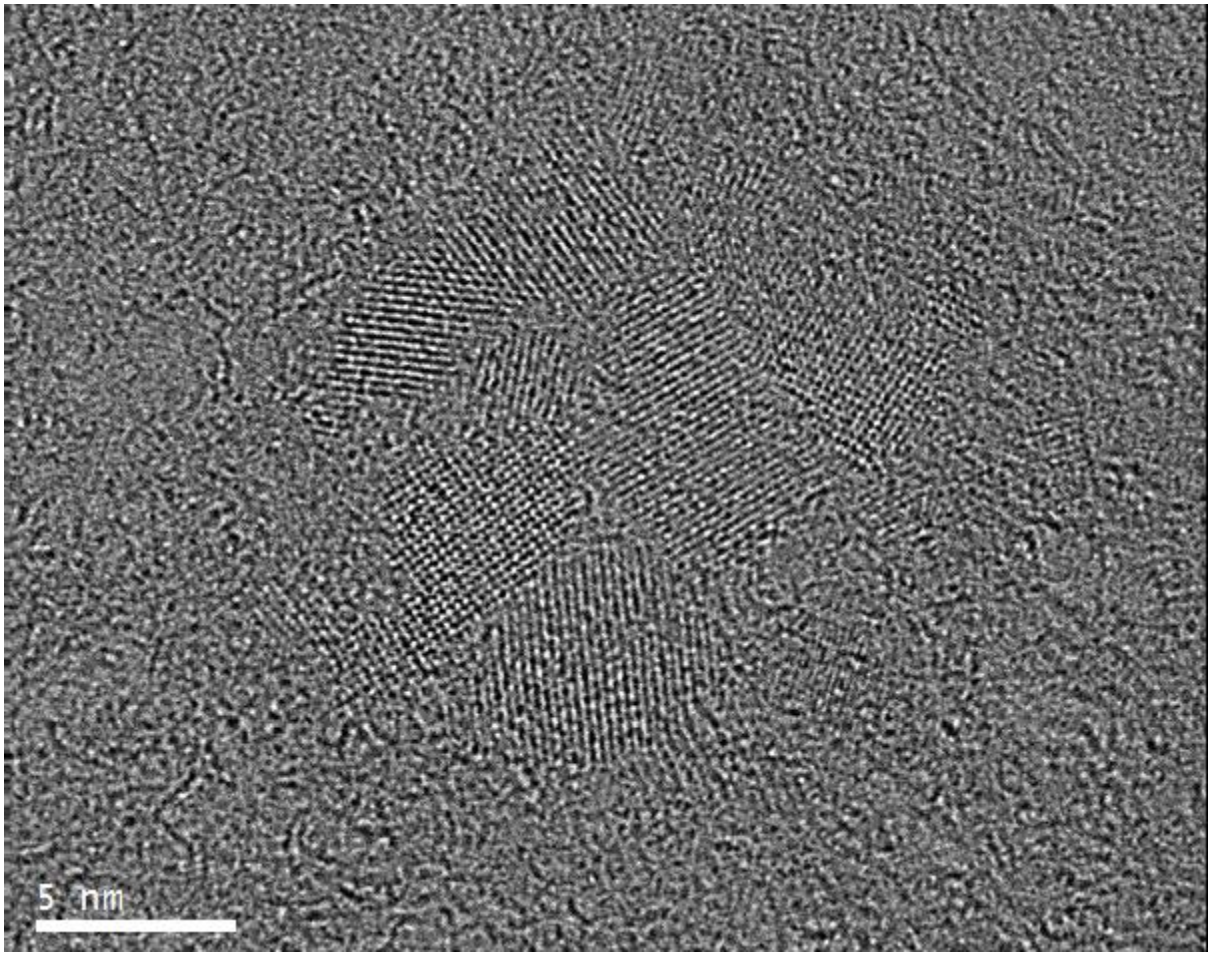


Figure 6.3. HRTEM image of the HBC molecules on ultrathin amorphous carbon.

6.2.2 Aberration-corrected STEM

For the ADF STEM characterisation HBC dispersion was drop-cast onto the holey-carbon grids with pre-deposited *h*-BN nanoflakes. 2D *h*-BN was to serve as a substrate for HBC molecules providing the possibility to confirm the presence of HBC using EELS. Before carrying out the actual experiment simulations were performed to assess the visibility of HBC on 2D *h*-BN with different numbers of layers (Fig. 6.4). Simulations show that contrast is quickly reduced as the thickness of the substrate grows. Therefore it was decided to limit imaged regions to the edges of the *h*-BN where protruding monolayers and bilayers can be found.

The typical image of the HBC deposited TEM grid is shown in Fig. 6.5a. Although it is not directly interpretable, the structure resembles an agglomerate of HBC molecules. The white circle indicates the area where the EELS carbon signal was detected and the red dotted circle corresponds to the area without a carbon signal. On account of the fact that EELS does not confirm the presence of HBC but only shows the

presence of carbon molecules, possibility of carbon contamination must be considered. The CHP solvent used for exfoliation of the HBC is believed to be the main possible source of carbon contamination. For this reason a control sample was deposited where pure CHP solvent was drop-cast on pre-deposited *h*-BN nanoflakes. Both the HBC and the control sample were baked identically prior to ADF STEM imaging. Although the control sample was relatively carbon free, certain areas (Fig. 6.5 b) displayed carbonaceous areas similar to the HBC sample.

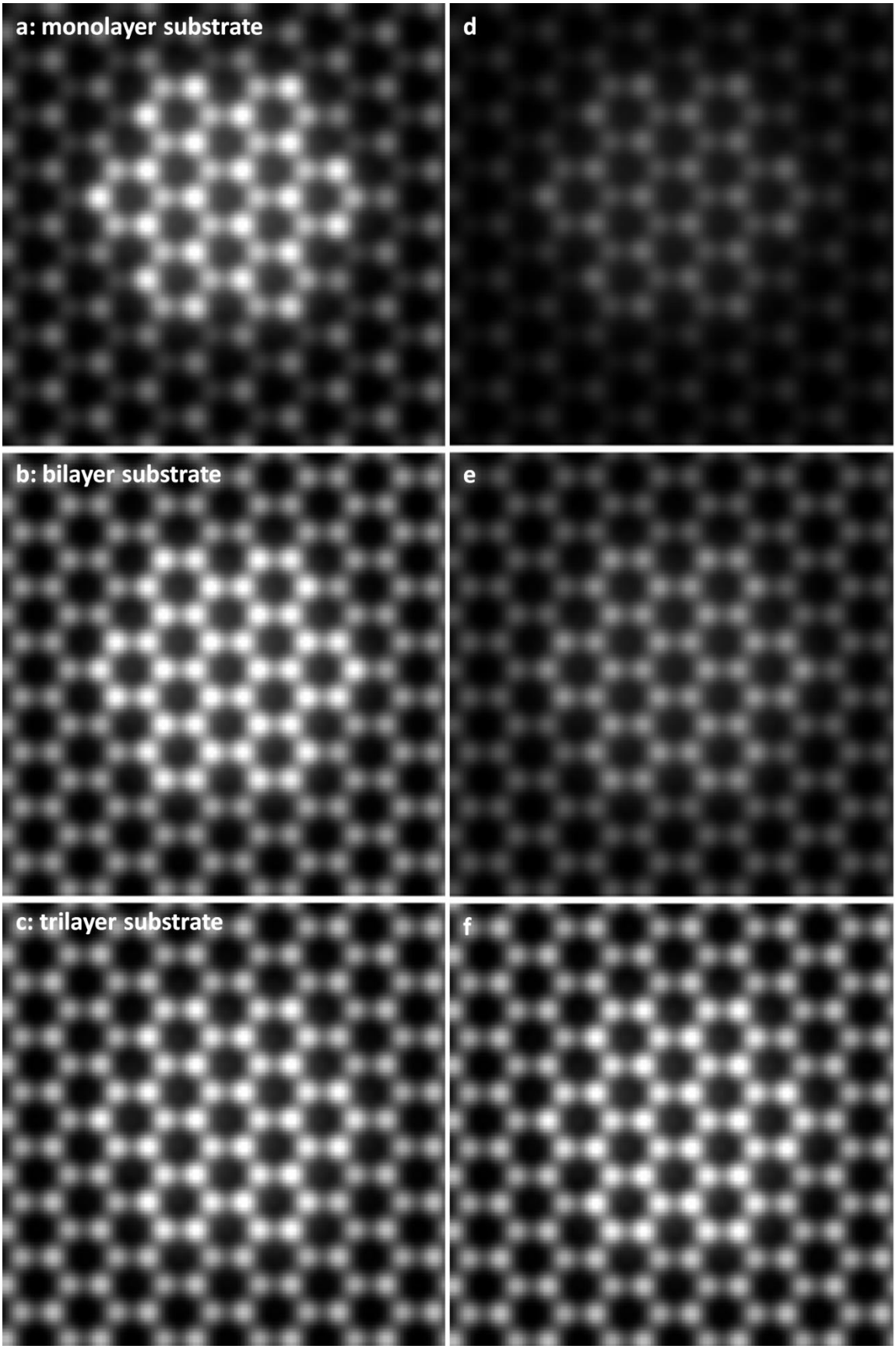


Figure 6.4. ADF STEM simulations of the HBC molecule on the 2D *h*-BN substrate. Substrate is (a) monolayer, (b) bilayer and (c) trilayer. Images a, b, c are shown on individual grayscale. (d), (e), (f) are images of (a), (b) and (c), correspondingly, shown on the same grayscale range.

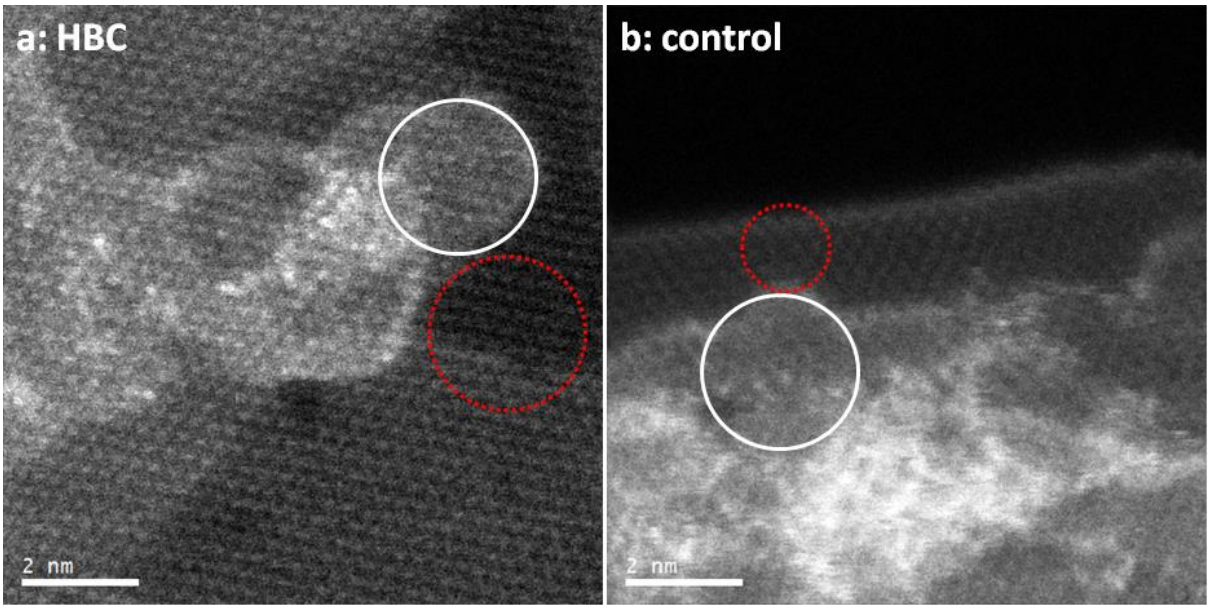


Figure 6.5. ADF STEM images of (a) HBC molecules in CHP solvent (b) pure CHP solvent deposited on *h*-BN nanoflakes. White circle indicates region where EELS carbon signal was detected and red dotted circle indicates region where carbon signal was not detected.

6.3 Summary of the findings

Aberration corrected TEM and STEM were used to image individual molecules of HBC in order to confirm successful liquid-phase exfoliation of HBC molecules. Unfortunately, the desired result was not fully achieved. HRTEM of the HBC molecules deposited on ultrathin carbon was the most successful. Several images displaying agglomerates of several HBC molecules were acquired. Moreover, strong electron beam damage was observed. Surprisingly, under the influence of electron beam HBC agglomerates were transformed into new crystalline phase with 90^{o} symmetry.

Chapter 7: Conclusions

7.1 Characterisation techniques

Over the course of this study a general routine was developed for the analysis of liquid exfoliated nanoflakes.

The first step involves optimisation of the sample using low resolution CTEM and SAED. These techniques give a rough estimate of the TEM grid coverage, nanoflake thickness and crystallinity. If the produced nanoflakes contain large uniform areas of the 2D nanocrystals SAED can be used to assess stacking sequences. Furthermore, for Li-intercalated samples SAED is expected to provide accurate measurement of the changes in the lattice parameters. For certain 2D nanocrystals SAED allows for differentiation between monolayer and multilayer regions. Although each different 2D nanocrystal requires separate analysis, a general trend can be deduced for the nanosheets with hexagonal lattice structure. This work suggests that differentiation between monolayer and multilayers is limited to the hexagonal structures with Bernal (ABA: graphite) and rhombohedral stacking (ABC: 3R MoS_2 and WS_2).

The second step is atomically resolved ADF STEM which allows direct, reliable interpretation of the images. Thickness, stacking point and substitutional defects are readily identifiable. Assessment of the results can be further assisted by image simulations. Moreover, simultaneous acquisition of EELS provides additional characterisation potential. Low-loss plasmon peaks of 2D nanostructures have a strong dependence on the number of layers. Core-loss major edges are sensitive to the changes in the electronic properties which can be useful in characterisation of the edge states. However, for the reliable EELS results comparison with modelling, which was not done here, is required.

The main challenges in using ADF STEM are the stringent requirements of the sample purity and stability of the microscope set-up. The draw-back of the ADF STEM is the difficulty in resolving low-Z columns next to the high-Z columns as in WS_2.

HRTEM has shown only limited potential in characterisation of the 2D nanomaterials. The oscillating contrast transfer function and low thickness sensitivity greatly hinders image interpretation. HRTEM might be preferable to ADF STEM in samples with grain boundaries like CVD grown graphene where diffractive imaging is

better suited. Also, HRTEM demonstrated better results in imaging light 2D molecules like HBC.

7.2 Structural findings

The main structural feature investigated in this thesis was the stacking sequences in few-layer *h*-BN, MoS_2, WS_2 and TiS_2 prepared by liquid-phase exfoliation. Bulk stacking and novel stacking sequences were reliably confirmed for all above 2D nanomaterials on the basis of ADF STEM.

20 different *h*-BN nanoflakes were imaged and analysed but only two of them demonstrated non-bulk stacking. Both of them consisted of regions where features of AA, AB and ABC sequences were confirmed. Shear strain was observed for regions with AB and ABC features. Also, the presence of impurities was identified for these nanoflakes which seemed to stabilise the non-bulk stacking. The possibility to tune the stacking sequence by addition of Na^+ impurity ions in restacked nanofilms was confirmed by electron diffraction analysis.

Two structural models, here called 1H and 2H' polytypes, were proposed for 2D MoS_2 and WS_2 with non-bulk stacking. These stacking sequences consist of metal ions placed exactly on top of each other for each consecutive layer and are referred to as homonuclear stacking. The reason for the two possible models is the inability to resolve sulphur column positions in ADF STEM images. 28 different MoS_2 nanoflakes were imaged and analysed. Amongst these, 17 were consistent with a 2H polytype, 9 with a homonuclear stacking and only 1 with a 3R polytype. In addition, one nanoflake displayed both homonuclear and 2H stacking. The nanoflake in the 3R polytype configuration exhibited a significantly shear strained lattice. Amongst the 5 examined WS_2 nanoflakes, one exhibited a 2H structure, whilst all the others were consistent with homonuclear stacking. The 3R polytype was never observed for 2D WS_2.

Although 2D TiS_2 was imaged with atomic resolution, it was impossible identify the steps in the nanoflakes. Hence, the structure was not assigned to the nanoflakes with non-bulk stacking. 6 TiS_2 nanoflakes were analysed. 4 were consistent with 1T polytype and one with non-bulk stacking. In the last case 1T structure and unknown phase with non-bulk lattice constant were identified.

Finally, an interesting structural transformation was observed in HBC molecules. Under the influence of electron beam HBC agglomerates were transformed into new crystalline phase with 90^{o} symmetry.

Generally, it can be concluded that 2D nanoflakes produced by liquid-phase exfoliation consist of several layers with gradual step-wise increase in the thickness from the edge towards the middle of the nanoflakes. In practical terms such nanomaterial is suitable as filler for nanocomposites and applications where deposition of nanofilms is required.

7.3 Future work

2D nanomaterials are still a relatively new topic of scientific research which has unlimited potential for future expansion. Below, several upcoming areas of research are outlined from the perspective of the 2D nanomaterials produced by liquid-phase exfoliation.

Deeper insight into the formation of non-bulk stacking sequences and their tuning by the ad-atoms is necessary. Moreover, changes in the stacking sequences must be correlated with electronic and mechanical properties.

Better quality SAED of 2D nanostructures with known thickness could provide an accurate estimate of the Debye-Waller factor. Moreover, the Debye-Waller factor might have dependence on the thickness of 2D nanostructures.

Only a fraction of layered materials have been exfoliated to date. Foreseeable expansion of the 2D nanomaterials family will require timely detailed structural and electronic characterisation of these novel 2D nanomaterials. Moreover, liquid-phase exfoliation as a production method must be further improved, delivering an increase in the monolayer yield and lateral flake size.

Functionalisation of the 2D nanomaterials is another unexplored area of the 2D nanoworld. Attachment of the functional groups can provide better quality liquid dispersions and improved filler for the nanocomposites. TEM characterisation of the successfully functionalised 2D nanomaterials will pose further challenges for the researchers.

References

[1] P. Wallace, “The band theory of graphite,” *Phys. Rev.*, vol. 71, no. 9, pp. 622–634, 1947.

[2] J. Slonczewski and P. Weiss, “Band structure of graphite,” *Phys. Rev.*, vol. 109, no. 2, pp. 272–279, 1958.

[3] S. Iijima, “Helical microtubules of graphitic carbon,” *Nature*, vol. 354, no. 6348, pp. 56–58, 1991.

[4] N. G. Chopra, R. J. Luyken, K. Cherrey, V. H. Crespi, M. L. Cohen, S. G. Louie, and a Zettl, “Boron nitride nanotubes.,” *Science*, vol. 269, no. 5226, pp. 966–7, Aug. 1995.

[5] A. Rubio, J. Corkill, and M. Cohen, “Theory of graphitic boron nitride nanotubes,” *Physical Review B*, vol. 49, no. 7. pp. 5081–5084, Feb-1994.

[6] K. S. Novoselov, A. K. Geim, S. V Morozov, D. Jiang, Y. Zhang, S. V Dubonos, I. V Grigorieva, and A. A. Firsov, “Electric field effect in atomically thin carbon films.,” *Science*, vol. 306, no. 5696, pp. 666–9, Oct. 2004.

[7] K. S. Novoselov, a K. Geim, S. V Morozov, D. Jiang, M. I. Katsnelson, I. V Grigorieva, S. V Dubonos, and a a Firsov, “Two-dimensional gas of massless Dirac fermions in graphene.,” *Nature*, vol. 438, no. 7065, pp. 197–200, Nov. 2005.

[8] Y. Zhang, Y.-W. Tan, H. L. Stormer, and P. Kim, “Experimental observation of the quantum Hall effect and Berry’s phase in graphene.,” *Nature*, vol. 438, no. 7065, pp. 201–4, Nov. 2005.

[9] K. S. Novoselov, D. Jiang, F. Schedin, T. J. Booth, V. V Khotkevich, S. V Morozov, and a K. Geim, “Two-dimensional atomic crystals.,” *Proc. Natl. Acad. Sci. U. S. A.*, vol. 102, no. 30, pp. 10451–3, Jul. 2005.

[10] D. Pacilé, J. C. Meyer, C. O. Girit, and a. Zettl, “The two-dimensional phase of boron nitride: Few-atomic-layer sheets and suspended membranes,” *Appl. Phys. Lett.*, vol. 92, no. 13, p. 133107, 2008.

[11] H. S. S. Ramakrishna Matte, a Gomathi, A. K. Manna, D. J. Late, R. Datta, S. K. Pati, and C. N. R. Rao, “MoS(2) and WS(2) Analogues of Graphene.,” *Angew. Chem. Int. Ed. Engl.*, vol. 064, pp. 4059 –4062, Apr. 2010.

[12] P. K. Dutta, A. S. M, and K. A. Carrad, *Handbook of Layered Materials*. CRC Press, 2004.

[13] L. D. Landau and E. M. Lifshitz, *Statistical Physics*, Third. Oxford: Pergamon Press, 1980, p. Part 1.

[14] N. Mermin, “Crystalline order in two dimensions,” *Phys. Rev.*, 1968.

[15] J. A. Venables, *Introduction to surface and thin film processes*. Cambridge University Press, 2003, p. 146.

[16] R. Kaischew, S. Stoyanov, and D. Kashchiev, “Recent investigations on nucleation and crystal growth processes,” *J. Cryst. Growth*, vol. 52, pp. 3–13, 1981.

[17] J. Venables, G. Spiller, and M, “Nucleation and growth of thin films,” *Reports Prog. Phys.*, Apr. 1984.

[18] G. Ruess and F. Vogt, “Höchstlamellarer Kohlenstoff aus Graphitoxyhydroxyd.,” *Monatshefte für Chemie*, vol. 78, no. 3–4, pp. 222–242, 1948.

[19] R. Frindt, “Single Crystals of MoS2 Several Molecular Layers Thick,” *J. Appl. Phys.*, vol. 37, pp. 1928–1929, 1966.

[20] P. Joensen, R. Frindt, and S. Morrison, “Single-layer MoS2,” *Mater. Res. Bull.*, vol. 21, no. 4, pp. 457–461, 1986.

[21] B. K. Miremadi and S. R. Morrison, “The intercalation and exfoliation of tungsten disulfide,” *J. Appl. Phys.*, vol. 63, no. 10, pp. 4970–4, 1988.

[22] A. Nagashima, N. Tejima, Y. Gamou, T. Kawai, and C. Oshima, “Electronic dispersion relations of monolayer hexagonal boron nitride formed on the Ni(111) surface,” *Physical Review B*, vol. 51, no. 7. pp. 4606–4613, Feb-1995.

[23] W. Auwärter, “XPD and STM investigation of hexagonal boron nitride on Ni(111),” *Surf. Sci.*, vol. 429, no. 1–3, pp. 229–236, Jun. 1999.

[24] J. Meyer, A. Geim, M. Katsnelson, K. Novoselov, D. Obergfell, S. Roth, C. Girit, and A. Zettl, “On the roughness of single- and bi-layer graphene membranes,” *Solid State Commun.*, vol. 143, no. 1–2, pp. 101–109, Jul. 2007.

[25] K. Xu, P. Cao, and J. R. Heath, “Scanning tunneling microscopy characterization of the electrical properties of wrinkles in exfoliated graphene monolayers.,” *Nano Lett.*, vol. 9, no. 12, pp. 4446–51, Dec. 2009.

[26] U. Bangert, M. H. Gass, A. L. Bleloch, R. R. Nair, and A. K. Geim, “Manifestation of ripples in free-standing graphene in lattice images obtained in an aberration-corrected scanning transmission electron microscope,” *Phys. status solidi*, vol. 206, no. 6, pp. 1117–1122, Jun. 2009.

[27] A. Splendiani, L. Sun, Y. Zhang, T. Li, J. Kim, and C. Chim, “Emerging Photoluminescence in Monolayer MoS2,” *Nano Lett*, vol. 10, no. 4, pp. 1271–5, Apr. 2010.

[28] K. Mak, C. Lee, J. Hone, J. Shan, and T. Heinz, “Atomically Thin MoS_{2}: A New Direct-Gap Semiconductor,” *Phys. Rev. Lett.*, vol. 105, no. 13, pp. 2–5, Sep. 2010.

[29] W. Zhao, Z. Ghorannevis, L. Chu, M. Toh, C. Kloc, P.-H. Tan, and G. Eda, “Evolution of electronic structure in atomically thin sheets of WS2 and WSe2.,” *ACS Nano*, vol. 7, no. 1, pp. 791–7, Jan. 2013.

[30] J. N. Coleman, M. Lotya, A. O’Neill, S. D. Bergin, P. J. King, U. Khan, K. Young, A. Gaucher, S. De, R. J. Smith, I. V. Shvets, S. K. Arora, G. Stanton, H.-Y. Kim, K. Lee, G. T. Kim, G. S. Duesberg, T. Hallam, J. J. Boland, J. J. Wang, J. F. Donegan, J. C. Grunlan, G. Moriarty, A. Shmeliov, R. J. Nicholls, J. M. Perkins, E. M. Grieveson, K. Theuwissen, D. W. McComb, P. D. Nellist, and V. Nicolosi, “Two-dimensional nanosheets produced by liquid exfoliation of layered materials,” *Science (80-.).*, vol. 331, no. 6017, pp. 568–571, Feb. 2011.

[31] C. Tusche, H. Meyerheim, and J. Kirschner, “Observation of Depolarized ZnO(0001) Monolayers: Formation of Unreconstructed Planar Sheets,” *Phys. Rev. Lett.*, vol. 99, no. 2, p. 026102, Jul. 2007.

[32] R. Addou, A. Dahal, and M. Batzill, “Growth of a two-dimensional dielectric monolayer on quasi-freestanding graphene.,” *Nat. Nanotechnol.*, vol. 8, no. 1, pp. 41–5, Jan. 2013.

[33] J. a. Wilson and a. D. Yoffe, “The transition metal dichalcogenides discussion and interpretation of the observed optical, electrical and structural properties,” *Adv. Phys.*, vol. 18, no. 73, pp. 193–335, May 1969.

[34] K. K. Kam and B. A. Parkinson, “Detailed photocurrent spectroscopy of the semiconducting group VI transition metal dichalcogenides,” *J. Phys. Chem.*, vol. 86, no. 4, pp. 463–467, Feb. 1982.

[35] M. Osada, K. Akatsuka, Y. Ebina, H. Funakubo, T. Kiguchi, K. Takada, and T. Sasaki, “Solution-Based Fabrication of High-κ Dielectric Nanofilms Using Titania Nanosheets as a Building Block,” *Jpn. J. Appl. Phys.*, vol. 46, no. No. 10B, pp. 6979–6983, Oct. 2007.

[36] R. Frindt, “Superconductivity in Ultrathin NbSe2 ayers,” *Physical Review Letters*, vol. 28, no. 5. pp. 299–301, Jan-1972.

[37] P. Williams, C. Scruby, and G. Tatlock, “Charge density waves in 2H—NbSe2,” *Solid State Commun.*, vol. 17, no. 9, pp. 1197–1200, 1975.

[38] S. Mishra, S. Satpathy, and O. Jepsen, “Electronic structure and thermoelectric properties of bismuth telluride and bismuth selenide,” *J. Phys. Condens. Matter*, vol. 9, p. 461, 1997.

[39] B. Poudel, Q. Hao, Y. Ma, Y. Lan, A. Minnich, B. Yu, X. Yan, D. Wang, A. Muto, D. Vashaee, X. Chen, J. Liu, M. S. Dresselhaus, G. Chen, and Z. Ren,

"High-thermoelectric performance of nanostructured bismuth antimony telluride bulk alloys.," *Science*, vol. 320, no. 5876, pp. 634–8, May 2008.

[40] F. A. Frame and F. E. Osterloh, "CdSe-MoS2: A Quantum Size-Confined Photocatalyst for Hydrogen Evolution from Water under Visible Light," *J. Phys. Chem. C*, vol. 114, no. 23, pp. 10628–10633, Jun. 2010.

[41] J. R. Miller, R. a. Outlaw, and B. C. Holloway, "Graphene Double-Layer Capacitor with ac Line-Filtering Performance," *Science (80-.).*, vol. 329, no. 5999, pp. 1637–1639, Sep. 2010.

[42] B. Radisavljevic, A. Radenovic, J. Brivio, V. Giacometti, and A. Kis, "Single-layer MoS2 transistors.," *Nat. Nanotechnol.*, vol. 6, no. 3, pp. 147–50, Mar. 2011.

[43] H. Li, Z. Yin, Q. He, H. Li, X. Huang, G. Lu, D. W. H. Fam, A. I. Y. Tok, Q. Zhang, and H. Zhang, "Fabrication of single- and multilayer MoS2 film-based field-effect transistors for sensing NO at room temperature.," *Small*, vol. 8, no. 1, pp. 63–7, Jan. 2012.

[44] A. K. Geim and I. V Grigorieva, "Van der Waals heterostructures.," *Nature*, vol. 499, no. 7459, pp. 419–25, Jul. 2013.

[45] L. a. Ponomarenko, a. K. Geim, a. a. Zhukov, R. Jalil, S. V. Morozov, K. S. Novoselov, I. V. Grigorieva, E. H. Hill, V. V. Cheianov, V. I. Fal'ko, K. Watanabe, T. Taniguchi, and R. V. Gorbachev, "Tunable metal–insulator transition in double-layer graphene heterostructures," *Nat. Phys.*, vol. 7, no. 12, pp. 958–961, Oct. 2011.

[46] S. J. Haigh, a Gholinia, R. Jalil, S. Romani, L. Britnell, D. C. Elias, K. S. Novoselov, L. a Ponomarenko, a K. Geim, and R. Gorbachev, "Cross-sectional imaging of individual layers and buried interfaces of graphene-based heterostructures and superlattices.," *Nat. Mater.*, vol. 11, no. 9, pp. 764–7, Sep. 2012.

[47] Z. Zeng, Z. Yin, X. Huang, H. Li, Q. He, G. Lu, F. Boey, and H. Zhang, "Single-layer semiconducting nanosheets: high-yield preparation and device fabrication.," *Angew. Chem. Int. Ed. Engl.*, vol. 50, no. 47, pp. 11093–7, Dec. 2011.

[48] Z. Zeng, T. Sun, J. Zhu, X. Huang, Z. Yin, G. Lu, Z. Fan, Q. Yan, H. H. Hng, and H. Zhang, "An effective method for the fabrication of few-layer-thick inorganic nanosheets.," *Angew. Chem. Int. Ed. Engl.*, vol. 51, no. 36, pp. 9052–6, Sep. 2012.

[49] Y. Hernandez, V. Nicolosi, M. Lotya, F. M. Blighe, Z. Sun, S. De, I. T. McGovern, B. Holland, M. Byrne, Y. K. Gun'Ko, J. J. Boland, P. Niraj, G. Duesberg, S. Krishnamurthy, R. Goodhue, J. Hutchison, V. Scardaci, A. C. Ferrari, and J. N. Coleman, "High-yield production of graphene by liquid-phase exfoliation of graphite.," *Nat. Nanotechnol.*, vol. 3, no. 9, pp. 563–8, Sep. 2008.

[50] M. Lotya, Y. Hernandez, P. King, R. Smith, and V, "Liquid phase production of graphene by exfoliation of graphite in surfactant/water solutions," *J. Am. Chem.*, vol. 131, no. 10, pp. 3611–20, Mar. 2009.

[51] R. J. Smith, P. J. King, M. Lotya, C. Wirtz, U. Khan, S. De, A. O'Neill, G. S. Duesberg, J. C. Grunlan, G. Moriarty, J. Chen, J. Wang, A. I. Minett, V. Nicolosi, and J. N. Coleman, "Large-scale exfoliation of inorganic layered compounds in aqueous surfactant solutions.," *Adv. Mater.*, vol. 23, no. 34, pp. 3944–8, Sep. 2011.

[52] W.-Q. Han, L. Wu, Y. Zhu, K. Watanabe, and T. Taniguchi, "Structure of chemically derived mono- and few-atomic-layer boron nitride sheets," *Appl. Phys. Lett.*, vol. 93, no. 22, p. 223103, 2008.

[53] S. Stankovich, D. Dikin, R. Piner, K. Kohlhaas, a Kleinhammes, Y. Jia, Y. Wu, S. Nguyen, and R. Ruoff, "Synthesis of graphene-based nanosheets via chemical reduction of exfoliated graphite oxide," *Carbon N. Y.*, vol. 45, no. 7, pp. 1558–1565, Jun. 2007.

[54] Y. Lin, T. V. Williams, and J. W. Connell, "Soluble, Exfoliated Hexagonal Boron Nitride Nanosheets," *J. Phys. Chem. Lett.*, vol. 1, no. 1, pp. 277–283, Jan. 2010.

[55] G. Eda and M. Chhowalla, "Graphene-based composite thin films for electronics.," *Nano Lett.*, vol. 9, no. 2, pp. 814–8, Feb. 2009.

[56] H. A. Becerril, J. Mao, Z. Liu, R. M. Stoltenberg, Z. Bao, and Y. Chen, "Evaluation of solution-processed reduced graphene oxide films as transparent conductors.," *ACS Nano*, vol. 2, no. 3, pp. 463–70, Mar. 2008.

[57] V. Nicolosi, M. Chhowalla, M. G. Kanatzidis, M. S. Strano, and J. N. Coleman, "Liquid Exfoliation of Layered Materials," *Science (80-.).*, vol. 340, no. 6139, pp. 1226419–1226419, Jun. 2013.

[58] X. Li, W. Cai, J. An, S. Kim, J. Nah, D. Yang, R. Piner, A. Velamakanni, I. Jung, E. Tutuc, S. K. Banerjee, L. Colombo, and R. S. Ruoff, "Large-area synthesis of high-quality and uniform graphene films on copper foils.," *Science*, vol. 324, no. 5932, pp. 1312–4, Jun. 2009.

[59] Y. Shi, W. Zhou, A.-Y. Lu, W. Fang, Y.-H. Lee, A. L. Hsu, S. M. Kim, K. K. Kim, H. Y. Yang, L.-J. Li, J.-C. Idrobo, and J. Kong, "van der Waals epitaxy of MoS_2 layers using graphene as growth templates.," *Nano Lett.*, vol. 12, no. 6, pp. 2784–91, Jun. 2012.

[60] Y. Zhan, Z. Liu, S. Najmaei, P. M. Ajayan, and J. Lou, "Large-area vapor-phase growth and characterization of MoS(2) atomic layers on a SiO(2) substrate.," *Small*, vol. 8, no. 7, pp. 966–71, Apr. 2012.

[61] Y. Cheng, K. Yao, Y. Yang, L. Li, Y. Yao, Q. Wang, X. Zhang, Y. Han, and U. Schwingenschlögl, "Van der Waals epitaxial growth of MoS2 on SiO2/Si by chemical vapor deposition," *RSC Adv.*, vol. 3, no. 38, p. 17287, 2013.

[62] P. Y. Huang, C. S. Ruiz-Vargas, A. M. van der Zande, W. S. Whitney, M. P. Levendorf, J. W. Kevek, S. Garg, J. S. Alden, C. J. Hustedt, Y. Zhu, J. Park, P. L. McEuen, and D. a. Muller, "Grains and grain boundaries in single-layer graphene atomic patchwork quilts," *Nature*, vol. 469, no. 7330, pp. 389–392, Jan. 2011.

[63] O. V. Yazyev and S. G. Louie, "Topological defects in graphene: Dislocations and grain boundaries," *Phys. Rev. B*, vol. 81, no. 19, p. 195420, May 2010.

[64] J. Hass, W. a de Heer, and E. H. Conrad, "The growth and morphology of epitaxial multilayer graphene," *J. Phys. Condens. Matter*, vol. 20, no. 32, p. 323202, Aug. 2008.

[65] Y. Zhang, L. Zhang, and C. Zhou, "Review of chemical vapor deposition of graphene and related applications.," *Acc. Chem. Res.*, vol. 46, no. 10, pp. 2329–39, Oct. 2013.

[66] S. D. Bergin, V. Nicolosi, P. V. Streich, S. Giordani, Z. Sun, A. H. Windle, P. Ryan, N. P. P. Niraj, Z.-T. T. Wang, L. Carpenter, W. J. Blau, J. J. Boland, J. P. Hamilton, and J. N. Coleman, "Towards Solutions of Single-Walled Carbon Nanotubes in Common Solvents," *Adv. Mater.*, vol. 20, no. 10, pp. 1876–1881, May 2008.

[67] D. B. Williams and B. C. Carter, *Transmission Electron Microscopy: A Textbook for Materials Science*, 2nd ed. New York: Springer Science, 2009.

[68] M. De Graef, *Introduction to Conventional Transmission Electron Microscopy (Cambridge Solid State Science Series)*. Cambridge University Press, 2003, p. 742.

[69] R. Brydson, Ed., *Aberration-Corrected Analytical Transmission Electron Microscopy*. Chichester, UK: John Wiley & Sons, Ltd, 2011.

[70] S. J. Pennycook and P. D. Nellist, Eds., *Scanning Transmission Electron Microscopy: Imaging and Analysis*. Springer, 2011, p. 774.

[71] E. J. Kirkland, *Advanced Computing in Electron Microscopy*. Springer, 2010, p. 299.

[72] L. de Broglie, "A tentative theory of light quanta," *Philos. Mag.*, vol. 47, pp. 446–458, 1924.

[73] C. Davisson and L. Germer, "Diffraction of Electrons by a Crystal of Nickel," *Phys. Rev.*, vol. 30, no. 6, pp. 705–740, Dec. 1927.

[74] G. P. Thomson, "Experiments on the Diffraction of Cathode Rays," in *Proceedings of the Royal Society of London. Series A, Containing Papers of a Mathematical and Physical Character*, 1928, pp. 600–609.

[75] M. Knoll and E. Ruska, "Das elektronenmikroskop," *Zeitschrift für Phys.*, vol. 78.5–6, pp. 318–339, 1932.

[76] O. Scherzer, “Uber einige Fehler von Elektronenlinsen,” *Zeitschrift fur Phys.*, vol. 101, no. 9–10, pp. 593–603, Sep. 1936.

[77] M. Ardenne, “Die Grenzen fur das Auflosungsvermogen des Elektronenmikroskops,” *Zeitschrift fur Phys.*, vol. 108, no. 5–6, pp. 338–352, May 1938.

[78] O. Scherzer, “Das theoretisch erreichbare Auflosungsvermogen des Elektronenmikroskops,” *Zeitschrift fur Phys.*, vol. 114, no. 7–8, pp. 427–434, Jul. 1939.

[79] A. Crewe, J. Wall, and J. Langmore, “Visibility of Single Atoms.,” *Sci. (New York, NY)*, vol. 168, no. 3937, pp. 1338–1340, 1970.

[80] J. Zach and M. Haider, “Aberration correction in a low voltage SEM by a multipole corrector,” *Nucl. Instruments Methods Phys. Res. Sect. A Accel. Spectrometers, Detect. Assoc. Equip.*, vol. 363, no. 1–2, pp. 316–325, Sep. 1995.

[81] S. Uhlemann and M. Haider, “Residual wave aberrations in the first spherical aberration corrected transmission electron microscope,” *Ultramicroscopy*, vol. 72, no. 3–4, pp. 109–119, May 1998.

[82] O. L. Krivanek, N. Dellby, and a. R. Lupini, “Towards sub-Å electron beams,” *Ultramicroscopy*, vol. 78, no. 1–4, pp. 1–11, Jun. 1999.

[83] E. Kirkland, B. Siegel, N. Uyeda, and Y. Fujiyoshi, “Digital reconstruction of bright field phase contrast images from high resolution electron micrographs,” *Ultramicroscopy*, vol. 5, pp. 479–503, 1980.

[84] A. I. Kirkland, W. O. Saxton, K.-L. Chau, K. Tsuno, and M. Kawasaki, “Super-resolution by aperture synthesis: tilt series reconstruction in CTEM,” *Ultramicroscopy*, vol. 57, no. 4, pp. 355–374, Mar. 1995.

[85] L. S. Ramsdell, “Studies on silicon carbide,” *Am. Mineral.*, vol. 32, pp. 64–83, 1947.

[86] A. Guinier (Chairman), G. B. Bokij, K. Boll-Dornberger, J. M. Cowley, S. Ďurovič, H. Jagodzinski, P. Krishna, P. M. de Wolff, B. B. Zvyagin, D. E. Cox, P. Goodman, T. Hahn, K. Kuchitsu, and S. C. Abrahams, “Nomenclature of polytype structures. Report of the International Union of Crystallography Ad hoc Committee on the Nomenclature of Disordered, Modulated and Polytype Structures,” *Acta Crystallogr. Sect. A Found. Crystallogr.*, vol. 40, no. 4, pp. 399–404, Jul. 1984.

[87] E. Prince, Ed., *International Tables for Crystallography*, vol. C. Chester, England: International Union of Crystallography, 2006, p. 752.

[88] A. P. Pogany and P. S. Turner, “Reciprocity in electron diffraction and microscopy,” *Acta Crystallogr. A*, vol. 24, no. 1, pp. 103–109, Jan. 1968.

[89] P. Hartel, “Conditions and reasons for incoherent imaging in STEM,” *Ultramicroscopy*, vol. 63, no. 2, pp. 93–114, Jun. 1996.

[90] R. F. Egerton, *Electron Energy-Loss Spectroscopy in the Electron Microscope*, 3rd ed. Springer, 2011, p. 6.

[91] J. M. Hughes, Y. Hernandez, D. Aherne, L. Doessel, K. Müllen, B. Moreton, T. W. White, C. Partridge, G. Costantini, A. Shmeliov, M. Shannon, V. Nicolosi, and J. N. Coleman, “High quality dispersions of hexabenzocoronene in organic solvents.,” *J. Am. Chem. Soc.*, vol. 134, no. 29, pp. 12168–79, Jul. 2012.

[92] C. O. Girit, J. C. Meyer, R. Erni, M. D. Rossell, C. Kisielowski, L. Yang, C.-H. Park, M. F. Crommie, M. L. Cohen, S. G. Louie, and A. Zettl, “Graphene at the edge: stability and dynamics.,” *Science*, vol. 323, no. 5922, pp. 1705–8, Mar. 2009.

[93] J. S. Kim, K. B. Borisenko, V. Nicolosi, and A. I. Kirkland, “Controlled radiation damage and edge structures in boron nitride membranes.,” *ACS Nano*, vol. 5, no. 5, pp. 3977–86, May 2011.

[94] A. Shmeliov, J. S. Kim, K. B. Borisenko, P. Wang, E. Okunishi, M. Shannon, A. I. Kirkland, P. D. Nellist, and V. Nicolosi, “Impurity induced non-bulk stacking in chemically exfoliated h-BN nanosheets.,” *Nanoscale*, vol. 5, no. 6, pp. 2290–4, Mar. 2013.

[95] J. Brivio, D. T. L. Alexander, and A. Kis, “Ripples and layers in ultrathin MoS2 membranes.,” *Nano Lett.*, vol. 11, no. 12, pp. 5148–53, Dec. 2011.

[96] O. L. Krivanek, M. F. Chisholm, V. Nicolosi, T. J. Pennycook, G. J. Corbin, N. Dellby, M. F. Murfitt, C. S. Own, Z. S. Szilagyi, M. P. Oxley, S. T. Pantelides, and S. J. Pennycook, “Atom-by-atom structural and chemical analysis by annular dark-field electron microscopy.,” *Nature*, vol. 464, no. 7288, pp. 571–574, Mar. 2010.

[97] Z. L. Wang, “An optical potential approach to incoherent multiple thermal diffuse scattering in quantitative HRTEM,” *Ultramicroscopy*, vol. 74, no. 1–2, pp. 7–26, Jul. 1998.

[98] Z. L. Wang, “The `Frozen-Lattice’ Approach for Incoherent Phonon Excitation in Electron Scattering. How Accurate Is It?,” *Acta Crystallogr. Sect. A Found. Crystallogr.*, vol. 54, no. 4, pp. 460–467, Jul. 1998.

[99] Z. L. Wang, “Thermal diffuse scattering in sub-angstrom quantitative electron microscopy—phenomenon, effects and approaches,” *Micron*, vol. 34, no. 3–5, pp. 141–155, Apr. 2003.

[100] F. Fujimoto, “Periodicity of crystal structure images in electron microscopy with crystal thickness,” *Phys. status solidi*, vol. 99, 1978.

[101] K. Kambe, “Visualization of bloch waves of high energy electrons in high resolution electron microscopy,” *Ultramicroscopy*, vol. 10, no. 3, pp. 223–227, Jan. 1982.

[102] C. R. Hall and P. B. Hirsch, “Effect of Thermal Diffuse Scattering on Propagation of High Energy Electrons Through Crystals,” *Proc. R. Soc. A Math. Phys. Eng. Sci.*, vol. 286, no. 1405, pp. 158–177, Jun. 1965.

[103] S. J. Pennycook and D. E. Jesson, “High-resolution Z-contrast imaging of crystals,” *Ultramicroscopy*, vol. 37, no. 1–4, pp. 14–38, Aug. 1991.

[104] P. Nellist and S. Pennycook, “Incoherent imaging using dynamically scattered coherent electrons,” *Ultramicroscopy*, vol. 78, no. 1999, pp. 111–124, 1999.

[105] L. J. Allen, S. D. Findlay, M. P. Oxley, and C. J. Rossouw, “Lattice-resolution contrast from a focused coherent electron probe. Part I.,” *Ultramicroscopy*, vol. 96, no. 1, pp. 47–63, Jul. 2003.

[106] S. D. Findlay, L. J. Allen, M. P. Oxley, and C. J. Rossouw, “Lattice-resolution contrast from a focused coherent electron probe. Part II.,” *Ultramicroscopy*, vol. 96, no. 1, pp. 65–81, Jul. 2003.

[107] J. LeBeau, S. Findlay, X. Wang, A. Jacobson, L. Allen, and S. Stemmer, “High-angle scattering of fast electrons from crystals containing heavy elements: Simulation and experiment,” *Phys. Rev. B*, vol. 79, no. 21, pp. 2–7, Jun. 2009.

[108] C. J. Rossouw, L. J. Allen, S. D. Findlay, and M. P. Oxley, “Channelling effects in atomic resolution STEM.,” *Ultramicroscopy*, vol. 96, no. 3–4, pp. 299–312, Sep. 2003.

[109] C. T. Koch, “QSTEM.” [Online]. Available: http://elim.physik.uni-ulm.de/?page_id=834.

[110] H. Katz-Boon, C. J. Rossouw, C. Dwyer, and J. Etheridge, “Rapid measurement of nanoparticle thickness profiles.,” *Ultramicroscopy*, vol. 124, pp. 61–70, Jan. 2013.

[111] S. D. Findlay and J. M. LeBeau, “Detector non-uniformity in scanning transmission electron microscopy.,” *Ultramicroscopy*, vol. 124, pp. 52–60, Jan. 2013.

[112] K. Schwetz, “Boron carbide, boron nitride, and metal borides,” *Ullmann’s Encycl. Ind. Chem.*, 1985.

[113] M. Hirayama, “CVD-BN for Boron Diffusion in Si and Its Application to Si Devices,” *J. Electrochem. Soc.*, vol. 122, no. 12, p. 1671, 1975.

[114] M. J. Rand and J. F. Roberts, “Preparation and Properties of Thin Film Boron Nitride,” *J. Electrochem. Soc.*, vol. 115, no. 4, p. 423, 1968.

[115] R. W. G. Wyckoff, *Crystal Structures*, Second. New York, 1963, pp. 85–237.

[116] Y.-N. Xu and W. Ching, "Calculation of ground-state and optical properties of boron nitrides in the hexagonal, cubic, and wurtzite structures," *Physical Review B*, vol. 44, no. 15. pp. 7787–7798, Oct-1991.

[117] N. Ooi, A. Rairkar, L. Lindsley, and J. B. Adams, "Electronic structure and bonding in hexagonal boron nitride," *J. Phys. Condens. Matter*, vol. 18, no. 1, pp. 97–115, Jan. 2006.

[118] J. Furthmüller, J. Hafner, and G. Kresse, "Ab initio calculation of the structural and electronic properties of carbon and boron nitride using ultrasoft pseudopotentials," *Physical Review B*, vol. 50, no. 21. pp. 15606–15622, Dec-1994.

[119] K. Watanabe, T. Taniguchi, and H. Kanda, "Direct-bandgap properties and evidence for ultraviolet lasing of hexagonal boron nitride single crystal.," *Nat. Mater.*, vol. 3, no. 6, pp. 404–9, Jun. 2004.

[120] C. R. Dean, A. F. Young, I. Meric, C. Lee, L. Wang, S. Sorgenfrei, K. Watanabe, T. Taniguchi, P. Kim, K. L. Shepard, and J. Hone, "Boron nitride substrates for high-quality graphene electronics," *Nat. Nanotechnol.*, vol. 5, no. October, pp. 722–726, Aug. 2010.

[121] I. Meric, C. Dean, A. Young, J. Hone, P. Kim, and K. L. Shepard, "Graphene field-effect transistors based on boron nitride gate dielectrics," in *Electron Devices Meeting (IEDM), 2010 IEEE International*, 2010, pp. 23.2.1 – 23.2.4.

[122] M. Si and D. Xue, "Magnetic properties of vacancies in a graphitic boron nitride sheet by first-principles pseudopotential calculations," *Phys. Rev. B*, vol. 75, no. 19, pp. 1–4, May 2007.

[123] M. S. Si, J. Y. Li, H. G. Shi, X. N. Niu, and D. S. Xue, "Divacancies in graphitic boron nitride sheets," *EPL (Europhysics Lett.*, vol. 86, no. 4, p. 46002, May 2009.

[124] C.-H. Park and S. G. Louie, "Energy gaps and stark effect in boron nitride nanoribbons.," *Nano Lett.*, vol. 8, no. 8, pp. 2200–3, Aug. 2008.

[125] X. Wu, M. Wu, and X. C. Zeng, "Chemically decorated boron-nitride nanoribbons," *Front. Phys. China*, vol. 4, no. 3, pp. 367–372, May 2009.

[126] C. Jin, F. Lin, K. Suenaga, and S. Iijima, "Fabrication of a freestanding boron nitride single layer and its defect assignments," *Phys. Rev. Lett.*, vol. 102, no. 19, pp. 3–6, May 2009.

[127] J. C. Meyer, A. Chuvilin, G. Algara-Siller, J. Biskupek, and U. Kaiser, "Selective sputtering and atomic resolution imaging of atomically thin boron nitride membranes.," *Nano Lett.*, vol. 9, no. 7, pp. 2683–2689, Jul. 2009.

[128] N. Alem, R. Erni, C. Kisielowski, M. Rossell, W. Gannett, and A. Zettl, "Atomically thin hexagonal boron nitride probed by ultrahigh-resolution transmission electron microscopy," *Phys. Rev. B*, vol. 80, no. 15, pp. 1–7, Oct. 2009.

[129] J. H. Warner, M. H. Rümmeli, A. Bachmatiuk, and B. Büchner, "Atomic resolution imaging and topography of boron nitride sheets produced by chemical exfoliation.," *ACS Nano*, vol. 4, no. 3, pp. 1299–304, Mar. 2010.

[130] A. Zobelli, A. Gloter, C. Ewels, G. Seifert, and C. Colliex, "Electron knock-on cross section of carbon and boron nitride nanotubes," *Phys. Rev. B*, vol. 75, no. 24, pp. 1–9, Jun. 2007.

[131] J. C. Meyer, C. Kisielowski, R. Erni, M. D. Rossell, M. F. Crommie, and a Zettl, "Direct imaging of lattice atoms and topological defects in graphene membranes.," *Nano Lett.*, vol. 8, no. 11, pp. 3582–6, Nov. 2008.

[132] X. Blase, a. De Vita, J.-C. Charlier, and R. Car, "Frustration Effects and Microscopic Growth Mechanisms for BN Nanotubes," *Phys. Rev. Lett.*, vol. 80, no. 8, pp. 1666–1669, Feb. 1998.

[133] R. Ribeiro and N. Peres, "Stability of boron nitride bilayers: Ground-state energies, interlayer distances, and tight-binding description," *Phys. Rev. B*, vol. 83, no. 23, pp. 1–6, Jun. 2011.

[134] L. Liu, Y. Feng, and Z. Shen, "Structural and electronic properties of h-BN," *Phys. Rev. B*, vol. 68, no. 10, pp. 1–8, Sep. 2003.

[135] S. Horiuchi, T. Gotou, M. Fujiwara, R. Sotoaka, M. Hirata, K. Kimoto, T. Asaka, T. Yokosawa, Y. Matsui, K. Watanabe, and M. Sekita, "Carbon Nanofilm with a New Structure and Property," *Jpn. J. Appl. Phys.*, vol. 42, no. Part 2, No.9A/B, pp. L1073–L1076, Sep. 2003.

[136] L.-M. Peng, G. Ren, S. L. Dudarev, and M. J. Whelan, "Debye–Waller Factors and Absorptive Scattering Factors of Elemental Crystals," *Acta Crystallogr. Sect. A Found. Crystallogr.*, vol. 52, no. 3, pp. 456–470, May 1996.

[137] N. Marom, J. Bernstein, J. Garel, A. Tkatchenko, E. Joselevich, L. Kronik, and O. Hod, "Stacking and registry effects in layered materials: The case of hexagonal boron nitride," *Phys. Rev. Lett.*, vol. 105, no. 4, pp. 1–4, Jul. 2010.

[138] S. Okada and M. Otani, "Stability and electronic structure of potassium-intercalated hexagonal boron nitride from density functional calculations," *Phys. Rev. B*, vol. 81, no. 23, pp. 3–6, Jun. 2010.

[139] N. Alem, Q. M. Ramasse, C. R. Seabourne, O. V. Yazyev, K. Erickson, M. C. Sarahan, C. Kisielowski, A. J. Scott, S. G. Louie, and A. Zettl, "Subangstrom Edge Relaxations Probed by Electron Microscopy in Hexagonal Boron Nitride," *Phys. Rev. Lett.*, vol. 109, no. 20, p. 205502, Nov. 2012.

[140] H. Sawada, T. Tomita, M. Naruse, T. Honda, P. Hambridge, P. Hartel, M. Haider, C. Hetherington, R. Doole, A. Kirkland, J. Hutchison, J. Titchmarsh, and D. Cockayne, "Experimental evaluation of a spherical aberration-corrected TEM and STEM.," *J. Electron Microsc. (Tokyo).*, vol. 54, no. 2, pp. 119–21, Apr. 2005.

[141] E. J. Kirkland, *Advanced Computing in Electron Microscopy*, 2nd ed. 2010.

[142] M. Hebbache, "Shear modulus and hardness of crystals: density functional calculations," *Solid State Commun.*, vol. 113, no. 8, pp. 427–432, Jan. 2000.

[143] R. Huisman, R. De Jonge, C. Haas, and F. Jellinek, "Trigonal-prismatic coordination in solid compounds of transition metals," *J. Solid State*, vol. 3, no. 1, pp. 56–66, Feb. 1971.

[144] J. Zhang, J. M. Soon, K. P. Loh, J. Yin, J. Ding, M. B. Sullivian, and P. Wu, "Magnetic molybdenum disulfide nanosheet films.," *Nano Lett.*, vol. 7, no. 8, pp. 2370–6, Aug. 2007.

[145] S. H. I. Chen, M. A. O. Da-heng, and F. Hao, "Preparation of tungsten disulfide motor oil and its tribological characteristics," pp. 673–678, 2007.

[146] P. D. Fleischauer, "Fundamental aspects of the electronic structure, materials properties and lubrication performance of sputtered MoS2 films," *Thin Solid Films*, vol. 154, no. 1–2, pp. 309–322, 1987.

[147] K. Hu, M. Liu, Q. Wang, Y. Xu, S. Schraube, and X. Hu, "Tribological properties of molybdenum disulfide nanosheets by monolayer restacking process as additive in liquid paraffin," *Tribol. Int.*, vol. 42, no. 1, pp. 33–39, Jan. 2009.

[148] O. Landa and S. Weisse, *Sulphide Catalysts, Their Properties and Applications*. New York: Pergamon Press, 1973.

[149] C. T. Tye and K. J. Smith, "Catalytic Activity of Exfoliated MoS2 in Hydrodesulfurization, Hydrodenitrogenation and Hydrogenation Reactions," *Top. Catal.*, vol. 37, no. 2–4, pp. 129–135, Apr. 2006.

[150] J. Bonde, P. Moses, T. Jaramillo, J. Nørskov, and I, "Hydrogen evolution on nano-particulate transition metal sulfides," *Faraday Discuss.*, vol. 28, no. 11, pp. 254–1897, Nov. 2009.

[151] a. Di Paola, L. Palmisano, M. Derrigo, and V. Augugliaro, "Preparation and Characterization of Tungsten Chalcogenide Photocatalysts," *J. Phys. Chem. B*, vol. 101, no. 6, pp. 876–883, Feb. 1997.

[152] E. Gourmelon, "MS2 (M = W, Mo) photosensitive thin films for solar cells," *Sol. Energy Mater. Sol. Cells*, vol. 46, no. 2, pp. 115–121, May 1997.

[153] J. M. Soon and K. P. Loh, "Electrochemical Double-Layer Capacitance of MoS[sub 2] Nanowall Films," *Electrochem. Solid-State Lett.*, vol. 10, no. 11, pp. A250–A254, 2007.

[154] C. Julien, S. Saikh, and G. Nazri, “Electrochemical studies of disordered MoS2 as cathode material in lithium batteries,” *Mater. Sci. Eng. B*, vol. 15, no. 1, pp. 73–77, Oct. 1992.

[155] J. Xiao, D. Choi, L. Cosimbescu, P. Koech, J. Liu, and J. P. Lemmon, “Exfoliated MoS2 nanocomposite as an anode material for lithium ion batteries,” *Chem. Mater.*, vol. 22, no. 15, pp. 4522–4524, Jul. 2010.

[156] C. Feng, L. Huang, Z. Guo, and H. Liu, “Synthesis of tungsten disulfide (WS2) nanoflakes for lithium ion battery application,” *Electrochem. commun.*, vol. 9, no. 1, pp. 119–122, Jan. 2007.

[157] A. Ayari, E. Cobas, O. Ogundadegbe, and M. S. Fuhrer, “Realization and electrical characterization of ultrathin crystals of layered transition-metal dichalcogenides,” *J. Appl. Phys.*, vol. 101, no. 1, p. 014507, 2007.

[158] M. Dines, “Lithium intercalation via-Butyllithium of the layered transition metal dichalcogenides,” *Mater. Res. Bull.*, vol. I, no. 5, pp. 87–91, 1975.

[159] M. A. Gee, R. F. Frindt, P. Joensen, and S. R. Morrison, “Inclusion compounds of MoS2,” *Mater. Res. Bull.*, vol. 21, no. 5, pp. 543–549, 1986.

[160] W. M. Divigalpitiya, R. F. Frindt, and S. R. Morrison, “Inclusion systems of organic molecules in restacked single-layer molybdenum disulfide.,” *Science*, vol. 246, no. 4928, pp. 369–71, Oct. 1989.

[161] W. M. R. Divigalpitiya, R. F. Frindt, and S. R. Morrison, “Molecular composite films of MoS2 and styrene,” *J. Mater. Res.*, vol. 6, no. 5, pp. 1103–1107, May 1991.

[162] R. Bissessur, M. G. Kanatzidis, J. L. Schindler, and C. R. Kannewurf, “Encapsulation of polymers into MoS2 and metal to insulator transition in metastable MoS2,” *J. Chem. Soc. Chem. Commun.*, no. 20, p. 1582, 1993.

[163] L. Wang, J. Schindler, J. A. Thomas, C. R. Kannewurf, and M. G. Kanatzidis, “Entrapment of polypyrrole chains between MoS2 layers via an in situ oxidative polymerization encapsulation reaction,” *Chem. Mater.*, vol. 7, no. 10, pp. 1753–1755, 1995.

[164] E. Benavente, M. A. Santa Ana, and G. González, “Electrical conductivity of MoS2 based organic–inorganic nanocomposites,” *Phys. status solidi*, vol. 241, no. 10, pp. 2444–2447, Aug. 2004.

[165] R. F. Frindt and D. Yang, “Restacked WS2(PEO)1.4 Nanocomposites,” *Mol. Cryst. Liq. Cryst.*, vol. 311, no. 1, pp. 367–375, Mar. 1998.

[166] B. Xu, B. Lin, D. Sun, and C. Ding, “Preparation and electrical conductivity of polyethers/WS2 layered nanocomposites,” *Electrochim. Acta*, vol. 52, no. 9, pp. 3028–3034, Feb. 2007.

[167] R. Bissessur, J. Heising, W. Hirpo, and M. Kanatzidis, “Toward Pillared Layered Metal Sulfides. Intercalation of the Chalcogenide Clusters Co6Q8 (PR3) 6 (Q= S, Se, and Te and R= Alkyl) into MoS2,” *Chem. Mater*, vol. 8, no. 11, pp. 318–320, 1996.

[168] R. Bissessur, R. I. Haines, D. Gallant, and R. Brüning, “Inclusion of a cobalt tetraazamacrocycle into layered molybdenum disulfide,” *Mater. Chem. Phys.*, vol. 122, no. 2–3, pp. 563–566, Aug. 2010.

[169] J.-W. Seo, Y.-W. Jun, S.-W. Park, H. Nah, T. Moon, B. Park, J.-G. Kim, Y. J. Kim, and J. Cheon, “Two-dimensional nanosheet crystals.,” *Angew. Chem. Int. Ed. Engl.*, vol. 46, no. 46, pp. 8828–31, Jan. 2007.

[170] G. Du, Z. Guo, S. Wang, R. Zeng, Z. Chen, and H. Liu, “Superior stability and high capacity of restacked molybdenum disulfide as anode material for lithium ion batteries.,” *Chem. Commun. (Camb).*, vol. 46, no. 7, pp. 1106–8, Feb. 2010.

[171] R. F. Frindt and A. D. Yoffe, “Physical Properties of Layer Structures: Optical Properties and Photoconductivity of Thin Crystals of Molybdenum Disulphide,” *Proc. R. Soc. A Math. Phys. Eng. Sci.*, vol. 273, no. 1352, pp. 69–83, Apr. 1963.

[172] R. Frindt, “Optical Absorption of a Few Unit-Cell Layers of MoS2,” *Physical Review*, vol. 140, no. 2A. pp. A536–A539, Oct-1965.

[173] D. Yang and R. F. Frindt, “Li-intercalation and exfoliation of WS2,” *J. Phys. Chem. Solids*, vol. 57, no. 6–8, pp. 1113–1116, Aug. 1996.

[174] D. Yang, S. Sandoval, W. Divigalpitiya, J. Irwin, and R. Frindt, “Structure of single-molecular-layer MoS2,” *Physical Review B*, vol. 43, no. 14. pp. 12053–12056, May-1991.

[175] R. Gordon, D. Yang, E. Crozier, D. Jiang, and R. Frindt, “Structures of exfoliated single layers of WS2, MoS2, and MoSe2 in aqueous suspension,” *Phys. Rev. B*, vol. 65, no. 12, pp. 1–9, Mar. 2002.

[176] F. Wypych, T. Weber, and R. Prins, “Scanning Tunneling Microscopic Investigation of 1T-MoS2,” *Chem. Mater.*, vol. 10, no. 3, pp. 723–727, Mar. 1998.

[177] C. Lee, H. Yan, L. E. Brus, T. F. Heinz, J. Hone, and S. Ryu, “Anomalous lattice vibrations of single- and few-layer MoS2.,” *ACS Nano*, vol. 4, no. 5, pp. 2695–700, May 2010.

[178] E. Prouzet, J. Heising, and M. G. Kanatzidis, “Structure of Restacked and Pillared WS2 : An X-ray Absorption Study,” *Chem. Mater.*, vol. 15, no. 2, pp. 412–418, Jan. 2003.

[179] X. Qin, D. Yang, R. Frindt, and J. Irwin, “Scanning tunneling microscopy of single-layer MoS2 in water and butanol,” *Ultramicroscopy*, vol. 42, pp. 630–636, 1992.

[180] R. Chianelli, A. Ruppert, M. Joseī-Yacamaīn, and A, "HREM studies of layered transition metal sulfide catalytic materials," *Catal. Today*, vol. 23, no. 3, pp. 269–281, 1995.

[181] J. Heising and M. G. Kanatzidis, "Structure of restacked MoS2 and WS2 elucidated by electron crystallography," *J. Am. Chem. Soc.*, vol. 121, no. 4, pp. 638–643, Feb. 1999.

[182] H. Search, C. Journals, A. Contact, and M. Iopscience, "The structure characterization of MoS2 and WS2 catalysts by HREM," *Microscopy*, vol. 219, 1993.

[183] L. P. Hansen, Q. M. Ramasse, C. Kisielowski, M. Brorson, E. Johnson, H. Topsøe, and S. Helveg, "Atomic-scale edge structures on industrial-style MoS2 nanocatalysts.," *Angew. Chem. Int. Ed. Engl.*, vol. 50, no. 43, pp. 10153–6, Oct. 2011.

[184] G. Eda, T. Fujita, H. Yamaguchi, D. Voiry, M. Chen, and M. Chhowalla, "Coherent atomic and electronic heterostructures of single-layer MoS2.," *ACS Nano*, vol. 6, no. 8, pp. 7311–7, Aug. 2012.

[185] R. R. Chianelli, J. C. Scanlon, and A. H. Thompson, "Structure refinement of stoichiometric TiS2," *Mater. Res. Bull.*, vol. 10, no. 12, pp. 1379–1382, Dec. 1975.

[186] A. Thompson, F. Gamble, and C. Symon, "The verification of the existence of TiS2," *Mater. Res. Bull.*, vol. i, no. 4, pp. 0–4, 1975.

[187] V. Ivanovskaya, G. Seifert, and A. Ivanovskii, "Electronic structure of titanium disulfide nanostructures: Monolayers, nanostripes, and nanotubes," *Semiconductors*, vol. 39, no. 9, pp. 1093–1100, 2005.

[188] C. Fang, R. de Groot, and C. Haas, "Bulk and surface electronic structure of 1T-TiS2 and 1T-TiSe2," *Phys. Rev. B*, vol. 56, no. 8, pp. 4455–4463, Aug. 1997.

[189] M. S. Whittingham, "Electrical energy storage and intercalation chemistry.," *Science*, vol. 192, no. 4244, pp. 1126–7, Jun. 1976.

[190] C. Lin, X. Zhu, J. Feng, C. Wu, S. Hu, J. Peng, Y. Guo, L. Peng, J. Zhao, J. Huang, J. Yang, and Y. Xie, "Hydrogen-Incorporated TiS2 Ultrathin Nanosheets with Ultrahigh Conductivity for Stamp-Transferrable Electrodes.," *J. Am. Chem. Soc.*, pp. 0–7, Mar. 2013.

[191] V. V. Plashnitsa, F. Vietmeyer, N. Petchsang, P. Tongying, T. H. Kosel, and M. Kuno, "Synthetic Strategy and Structural and Optical Characterization of Thin Highly Crystalline Titanium Disulfide Nanosheets," *J. Phys. Chem. Lett.*, vol. 3, no. 11, pp. 1554–1558, Jun. 2012.

[192] J. H. Paterson and O. L. Krivanek, "ELNES of 3d transition-metal oxides," *Ultramicroscopy*, vol. 32, no. 4, pp. 319–325, May 1990.

[193] X. Lin, Y. Wang, and V. Dravid, “Valence states and hybridization in vanadium oxide systems investigated by transmission electron-energy-loss spectroscopy,” *Phys. Rev. B*, vol. 47, no. 7, pp. 3477–3481, 1993.

[194] D. Pearson, C. Ahn, and B. Fultz, “White lines and d-electron occupancies for the 3d and 4d transition metals,” *Phys. Rev. B*, vol. 47, no. 14, pp. 8471–8478, 1993.

[195] V. Gallegos-Orozco, A. Santos-Beltrán, R. Martínez-Sánchez, and F. Espinosa-Magaña, “White Lines and Electron Occupancy for Ti 3d States in BaTiO3 by EELS,” *Microsc. Microanal.*, vol. 13, no. S02, Aug. 2007.

[196] H. Hernandez-Hernandez, L. Gonzalez-Hernandez, H. Flores-Zuniga, F. Espinosa-Magana, and D. Rios-Jara, “EELS Study of the Effect of Temperature on Ti L23 White Lines,” *Microsc. Microanal.*, vol. 10, no. S02, Aug. 2004.

[197] E. Clar, C. T. Ironside, and M. Zander, “28. The electronic interaction between benzenoid rings in condensed aromatic hydrocarbons. 1 : 12-2 : 3-4 : 5-6 : 7-8 : 9-10 : 11-hexabenzocoronene, 1 : 2-3 : 4-5 : 6-10 : 11-tetrabenzoanthanthrene, and 4 : 5-6 : 7-11 : 12-13 : 14-tetrabenzoperopyrene,” *J. Chem. Soc.*, no. 142, p. 142, 1959.

[198] C. D. Simpson, J. D. Brand, A. J. Berresheim, L. Przybilla, H. J. Räder, and K. Müllen, “Synthesis of a giant 222 carbon graphite sheet.,” *Chemistry*, vol. 8, no. 6, pp. 1424–9, Mar. 2002.

[199] J. Wu, W. Pisula, and K. Müllen, “Graphenes as potential material for electronics.,” *Chem. Rev.*, vol. 107, no. 3, pp. 718–47, Mar. 2007.

[200] A. Rouhanipour, M. Roy, X. Feng, H. J. Räder, and K. Müllen, “Subliming the unsublimable: how to deposit nanographenes.,” *Angew. Chem. Int. Ed. Engl.*, vol. 48, no. 25, pp. 4602–4, Jan. 2009.

[201] D. L. Kokkin, T. P. Troy, M. Nakajima, K. Nauta, T. D. Varberg, G. F. Metha, N. T. Lucas, and T. W. Schmidt, “The Optical Spectrum of a Large Isolated Polycyclic Aromatic Hydrocarbon: Hexa- peri -hexabenzocoronene, C 42 H 18,” *Astrophys. J.*, vol. 681, no. 1, pp. L49–L51, Jul. 2008.

[202] M. Steglich, J. Bouwman, F. Huisken, and T. Henning, “Can Neutral and Ionized Polycyclic Aromatic Hydrocarbons Be Carriers of the Ultraviolet Extinction Bump and the Diffuse Interstellar Bands?,” *Astrophys. J.*, vol. 742, no. 1, p. 2, Nov. 2011.

[203] W. Hendel, Z. H. Khan, and W. Schmidt, “Hexa-peri-benzocoronene, a candidate for the origin of the diffuse interstellar visible absorption bands ?,” *Tetrahedron*, vol. 42, no. 4, pp. 1127–1134, Jan. 1986.

[204] A. J. Fleming, J. N. Coleman, A. B. Dalton, A. Fechtenkötter, M. D. Watson, K. Müllen, H. J. Byrne, and W. J. Blau, “Optical Spectroscopy of Isolated and Aggregate Hexabenzocoronene Derivatives: A Study of Self-Assembling Molecular Nanowires,” *J. Phys. Chem. B*, vol. 107, no. 1, pp. 37–43, Jan. 2003.

[205] M. Kastler, W. Pisula, D. Wasserfallen, T. Pakula, and K. Müllen, "Influence of alkyl substituents on the solution- and surface-organization of hexa-peri-hexabenzocoronenes.," *J. Am. Chem. Soc.*, vol. 127, no. 12, pp. 4286–96, Mar. 2005.

[206] Y. Natsume, T. Minakata, and T. Aoyagi, "Structures and electronic properties of thin-films of polycyclic aromatic hydrocarbons," *Thin Solid Films*, vol. 517, no. 9, pp. 3005–3010, Mar. 2009.

[207] W. W. H. Wong, T. B. Singh, D. Vak, W. Pisula, C. Yan, X. Feng, E. L. Williams, K. L. Chan, Q. Mao, D. J. Jones, C.-Q. Ma, K. Müllen, P. Bäuerle, and A. B. Holmes, "Solution Processable Fluorenyl Hexa-peri-hexabenzocoronenes in Organic Field-Effect Transistors and Solar Cells," *Adv. Funct. Mater.*, vol. 20, no. 6, pp. 927–938, Mar. 2010.

[208] a. M. van de Craats, N. Stutzmann, O. Bunk, M. M. Nielsen, M. Watson, K. Müllen, H. D. Chanzy, H. Sirringhaus, and R. H. Friend, "Meso-Epitaxial Solution-Growth of Self-Organizing Discotic Liquid-Crystalline Semiconductors," *Adv. Mater.*, vol. 15, no. 6, pp. 495–499, Mar. 2003.

[209] W. W. H. Wong, D. J. Jones, C. Yan, S. E. Watkins, S. King, S. a Haque, X. Wen, K. P. Ghiggino, and A. B. Holmes, "Synthesis, photophysical, and device properties of novel dendrimers based on a fluorene-hexabenzocoronene (FHBC) core.," *Org. Lett.*, vol. 11, no. 4, pp. 975–8, Feb. 2009.

[210] L. Schmidt-Mende, A. Fechtenkötter, and K. Müllen, "Self-organized discotic liquid crystals for high-efficiency organic photovoltaics," *Science (80-.).*, vol. 293, no. 5532, pp. 1119–1122, 2001.

[211] J. M. Englert, F. Hauke, X. Feng, K. Müllen, and A. Hirsch, "Exfoliation of hexa-peri-hexabenzocoronene in water.," *Chem. Commun. (Camb).*, vol. 46, no. 48, pp. 9194–6, Dec. 2010.

[212] M. Ai, S. Groeper, W. Zhuang, X. Dou, X. Feng, K. Müllen, and J. P. Rabe, "Optical switching studies of an azobenzene rigidly linked to a hexa-peri-hexabenzocoronene derivative in solution and at a solid–liquid interface," *Appl. Phys. A*, vol. 93, no. 2, pp. 277–283, Sep. 2008.

[213] L. Gross, F. Mohn, N. Moll, B. Schuler, A. Criado, E. Guitián, D. Peña, A. Gourdon, and G. Meyer, "Bond-order discrimination by atomic force microscopy.," *Science*, vol. 337, no. 6100, pp. 1326–9, Sep. 2012.

[214] M. Koshino, T. Tanaka, N. Solin, K. Suenaga, H. Isobe, and E. Nakamura, "Imaging of single organic molecules in motion.," *Science*, vol. 316, no. 5826, p. 853, May 2007.

Appendix A: Structure Factor Calculation

The expression for structure factor, $F_{hkl}(\theta)$, is given by

$$F_{hkl}(\theta) = \sum_n f_n\,(\theta) e^{2\pi i(hx_n + ky_n + lz_n)}$$

where $f_n(\theta)$ is the atomic scattering amplitude of the nth atom with coordinates (x_n, y_n, z_n). The values of $f_n(\theta)$ can be found in the International Tables for Crystallography Volume C where $f_n(\theta)$ is given as a function of $\sin\theta/\lambda$. The values of $\sin\theta/\lambda$ can be related to magnitude of reciprocal space vectors, $|\mathbf{g}_{hkl}|$, via Bragg's Law:

$$\lambda = 2d\sin\theta$$

$$\frac{\sin\theta}{\lambda} = \frac{1}{2d} = \frac{1}{2}|\mathbf{g}_{hkl}|$$

The general expression $|\mathbf{g}_{hkl}|$ to unit cell parameters of the hexagonal lattice, a and c is

$$|\mathbf{g}_{hkl}|^2 = (h \quad k \quad l)\begin{pmatrix} \frac{4}{3a^2} & \frac{2}{3a^2} & 0 \\ \frac{2}{3a^2} & \frac{4}{3a^2} & 0 \\ 0 & 0 & \frac{1}{c^2} \end{pmatrix}\begin{pmatrix} h \\ k \\ l \end{pmatrix}$$

The corresponding formulae for $|\mathbf{g}_{100}|$ and $|\mathbf{g}_{110}|$ are:

$$|\mathbf{g}_{100}| = \frac{2}{a\sqrt{3}}; \qquad |\mathbf{g}_{110}| = \frac{2}{a}$$

A case of h-BN (AB)

Monolayer:

$$F_{hk0} = \left(f_{N_{hk0}} + f_{B_{hk0}} e^{i2\pi\left(\frac{1}{3}h+\frac{2}{3}k\right)}\right)$$

Bilayer:

$$F_{hk0} = \left(f_{N_{hk0}} + f_{B_{hk0}} e^{i2\pi\left(\frac{1}{3}h+\frac{2}{3}k\right)}\right)\left(1 + e^{i2\pi\left(\frac{1}{3}h+\frac{2}{3}k\right)}\right)$$

Substituting elastic scattering factors given in Table A1 the squared ratios of structure factor magnitudes can be obtained

$$\left(\frac{|F_{100}|^2}{|F_{110}|^2}\right)_{monolayer} = 1.1; \qquad \left(\frac{|F_{100}|^2}{|F_{110}|^2}\right)_{bilayer} = 0.28$$

Table A.1. Elastic scattering factors for {**100**} and {**110**} families of planes for neutral atoms of boron and nitrogen.

$\{hkl\}$	{100}	{110}
$f_{B_{hkl}}\ (\text{Å}^{-1})$	1.158	0.493
$f_{N_{hkl}}\ (\text{Å}^{-1})$	1.300	0.684

Appendix B: C_S-corrector drift

Table B1. Example of the $\boldsymbol{C_s}$-corrector drift on an average day. HRTEM configuration. JEOL2200MCO.

	at time, $t = 0$	at time, $t = 30$ min
A_1 (nm)	0.27	3.12
A_2 (nm)	118	187.1
B_2 (nm)	38.1	70
C_3, C_s (μm)	1.07	0.59
A_3 (μm)	0.72	1.65
S_3 (μm)	1.12	1.63